

1-1-2007

## Polarized X-ray emission spectroscopy at the chlorine K edge of the chlorofluoromethanes

Amanda C Hudson  
*University of Nevada, Las Vegas*

Follow this and additional works at: <https://digitalscholarship.unlv.edu/rtds>

---

### Repository Citation

Hudson, Amanda C, "Polarized X-ray emission spectroscopy at the chlorine K edge of the chlorofluoromethanes" (2007). *UNLV Retrospective Theses & Dissertations*. 2741.  
<http://dx.doi.org/10.25669/nvna-8qij>

This Dissertation is protected by copyright and/or related rights. It has been brought to you by Digital Scholarship@UNLV with permission from the rights-holder(s). You are free to use this Dissertation in any way that is permitted by the copyright and related rights legislation that applies to your use. For other uses you need to obtain permission from the rights-holder(s) directly, unless additional rights are indicated by a Creative Commons license in the record and/or on the work itself.

This Dissertation has been accepted for inclusion in UNLV Retrospective Theses & Dissertations by an authorized administrator of Digital Scholarship@UNLV. For more information, please contact [digitalscholarship@unlv.edu](mailto:digitalscholarship@unlv.edu).

POLARIZED X-RAY EMISSION SPECTROSCOPY AT THE Cl K EDGE OF  
THE CHLOROFLUOROMETHANES

by

Amanda C. Hudson

Bachelor of Science in Chemistry  
University of Nevada, Reno  
2001

Master of Science in Chemistry  
University of Nevada, Las Vegas  
2003

A dissertation submitted in partial fulfillment  
of the requirements for the

**Doctor of Philosophy Degree in Chemistry**  
**Department of Chemistry**  
**College of Sciences**

**Graduate College**  
**University of Nevada, Las Vegas**  
**August 2007**

UMI Number: 3282004

Copyright 2007 by  
Hudson, Amanda C.

All rights reserved.

#### INFORMATION TO USERS

The quality of this reproduction is dependent upon the quality of the copy submitted. Broken or indistinct print, colored or poor quality illustrations and photographs, print bleed-through, substandard margins, and improper alignment can adversely affect reproduction.

In the unlikely event that the author did not send a complete manuscript and there are missing pages, these will be noted. Also, if unauthorized copyright material had to be removed, a note will indicate the deletion.

**UMI**<sup>®</sup>

---

UMI Microform 3282004

Copyright 2007 by ProQuest Information and Learning Company.

All rights reserved. This microform edition is protected against  
unauthorized copying under Title 17, United States Code.

ProQuest Information and Learning Company  
300 North Zeeb Road  
P.O. Box 1346  
Ann Arbor, MI 48106-1346

Copyright by Amanda C. Hudson 2007  
All Rights Reserved



## Dissertation Approval

The Graduate College  
University of Nevada, Las Vegas

June 28, 20 07

The Dissertation prepared by

Amanda C. Hudson

### Entitled

Polarized X-Ray Emission Spectroscopy at the Cl K Edge of the  
Chlorofluoromethanes

is approved in partial fulfillment of the requirements for the degree of

Doctor of Philosophy Degree in Chemistry

Examination Committee Chair

Dean of the Graduate College

Examination Committee Member

Examination Committee Member

Graduate College Faculty Representative

## ABSTRACT

### **Polarized X-Ray Emission Spectroscopy at the Cl *K* Edge of the Chlorofluoromethanes**

by

Amanda C. Hudson

Dr. Dennis W. Lindle, Examination Committee Chair  
Professor of Chemistry  
University of Nevada, Las Vegas

The x-ray emission of CCl<sub>4</sub>, CFCl<sub>3</sub>, CF<sub>2</sub>Cl<sub>2</sub>, and CF<sub>3</sub>Cl has been observed by measuring the polarized Cl *K-L* and *K-V* fluorescence in the gas phase. Experiments were conducted at the Advanced Light Source in Berkeley CA using a polarization sensitive x-ray emission spectrometer. In both energy ranges, the measured x-ray peak widths and energy dispersion are dependent on the initial photon energy and the final state lifetime broadening and can be described with established theoretical models. The first measurement of a negative energy dispersion is reported here where the energies of the emitted peaks are decreasing with increasing photon energy close to the 4*p* Rydberg. In this case, the emitted photon's energy is dependent on vibrational excitations of several intermediate states. In the *K-L* energy range, there are significant deviations from the statistical 2:1 spin-orbit ratio that can be attributed to molecular field effects. The extent of the molecular field effects is dependent on the symmetry of the molecule and the orientation of the orbitals involved in absorption and emission with the emission in

the parallel direction showing the largest effects. In the  $K$ - $V$  energy range, the x-ray emission above the ionization potential (IP) was observed to be anisotropic in  $\text{CF}_2\text{Cl}_2$  and  $\text{CCl}_4$  and largely isotropic in  $\text{CF}_3\text{Cl}$ . This difference above the IP has been attributed to nondipole effects where vibronic coupling between near degenerate states (Cl  $1s$  orbitals) can open decay channels otherwise not seen when the dipole approximation holds; this explains why anisotropy is seen in molecules with multiple Cl atoms.

## TABLE OF CONTENTS

ABSTRACT .....	iii
LIST OF FIGURES .....	viii
ACKNOWLEDGEMENTS .....	x
CHAPTER 1 INTRODUCTION .....	1
CHAPTER 2 THEORETICAL REVIEW .....	9
Stimulated Absorption .....	9
Nonresonant X-Ray Emission.....	11
Resonant X-Ray Scattering (RXS) .....	12
Spin-Orbit Splitting.....	15
Polarization .....	16
Resonance Approximation and Classical Limits .....	19
CHAPTER 3 EXPERIMENTAL REVIEW .....	20
Resonant X-Ray Scattering.....	20
Angular Distribution and Polarization.....	22
Cl K-Edge.....	22
C K-Edge.....	28
Lifetime-Vibrational Interference .....	30
Screening.....	32
Parity Selection and Forbidden Transitions (Nondipole) .....	34
Molecular Field Effects.....	39
Assigning XAS Using XES .....	40
Ultrafast XES .....	43
CHAPTER 4 EXPERIMENTAL SET-UP .....	46
Advanced Light Source (ALS) .....	46
X-Ray Emission Spectrometer.....	47
Vacuum Isolation.....	50
Gas Cell.....	51
Crystal Bender .....	53
Detector.....	55
Alignment and Energy Calibration .....	57
Argon Spectral Calibration .....	61
Spectrometer Equations .....	63
Gas Samples.....	65



CHAPTER 5	Cl <i>K-L</i> Results.....	66
	Cl <i>K-Edge</i> Absorption.....	66
	Cl <i>K-L</i> Emission.....	73
	Cl $1s \rightarrow \text{LUMO}$ .....	73
	Peak Widths .....	77
	Dispersion .....	81
	Spin-Orbit Ratio.....	84
	Polarization .....	89
	Cl $1s \rightarrow 4p$ .....	91
	Peak Widths .....	91
	Dispersion .....	93
	Spin-Orbit Ratio.....	97
	Polarization .....	100
	Cl $1s \rightarrow \infty$ .....	102
CHAPTER 6	Cl <i>K-V</i> Results .....	109
	CF <sub>2</sub> Cl <sub>2</sub> .....	109
	<i>K-V</i> Valence Molecular Orbitals.....	109
	Peak Widths .....	113
	Dispersion .....	114
	Peak Ratios.....	118
	Polarization .....	122
	Bonus Peak.....	127
	CCl <sub>4</sub> .....	128
	<i>K-V</i> Valence Molecular Orbitals.....	128
	Peak Widths .....	129
	Dispersion .....	130
	Peak Ratios.....	131
	Polarization .....	133
	CF <sub>3</sub> Cl.....	135
	<i>K-V</i> Valence Molecular Orbitals.....	135
	Peak Widths .....	137
	Dispersion .....	139
	Peak Ratios.....	140
	Polarization .....	144
	Polarization Ratios of CF <sub>2</sub> Cl <sub>2</sub> , CCl <sub>4</sub> , and CF <sub>3</sub> Cl.....	147
CHAPTER 7	CONCLUSION .....	150
	Absorption Spectra.....	150
	Peak Widths, Dispersion, and Polarization.....	151
	SO Ratios, Nondipole, and Anti-Raman Dispersion .....	152
	Conclusion .....	155
APPENDIX I	RAISING AND LOWERING OPERATORS OF J .....	156

APPENDIX II	AUTOCAD DRAWING OF THE X-RAY EMISSION SPECTROMETER .....	158
APPENDIX III	CHARACTER TABLES FOR $C_{2v}$ , $C_{3v}$ , AND $T_d$ MOLECULES.....	159
REFERENCES	.....	161
VITA	.....	166

## LIST OF FIGURES

Figure 1	Absorption and Photoelectron Production.....	3
Figure 2	X-Ray and Auger Electron Emission .....	6
Figure 3	Resonant X-ray Emission .....	8
Figure 4	Cu <i>K-L</i> X-Ray Dispersion and Peak Widths .....	21
Figure 5	Polarized Cl <i>K-V</i> X-Ray Emission Spectra of CH <sub>3</sub> Cl .....	23
Figure 6	Polarized Cl <i>K-V</i> X-Ray Emission Spectra of CFC <sub>3</sub> , CF <sub>3</sub> Cl, and CF <sub>2</sub> Cl <sub>2</sub> .....	25
Figure 7	C <i>K-Edge</i> X-Ray Emission Spectra of CO.....	29
Figure 8	Simulated C and O <i>K</i> Vibrationally Resolved Absorption Spectra.....	32
Figure 9	Cl <i>K-L</i> and <i>K-V</i> X-Ray Dispersion and Peak Widths of HCl.....	44
Figure 10	Cl <i>K-V</i> X-Ray Emission Spectra of HCl .....	45
Figure 11	Schematic of Beamline 9.3.1.....	47
Figure 12	Schematic of the X-Ray Emission Spectrometer .....	49
Figure 13	Vacuum Interlock Box .....	51
Figure 14	Gas Cell Interaction Region .....	52
Figure 15	Schematic of the Crystal Bending Device.....	54
Figure 16	Micrometer Measurement of the Crystal Bender .....	55
Figure 17	Raw Detector Image .....	57
Figure 18	Cl <i>K-L</i> and <i>K-V</i> Energy Calibration .....	59
Figure 19	Cl <i>K-L</i> Energy Calibrated Spectra .....	59
Figure 20	Energy Window and Slit Position .....	60
Figure 21	Ar <i>K-Edge</i> Absorption and <i>K-L</i> Emission Spectra.....	61
Figure 22	Ar <i>K-L</i> X-Ray Peak Widths and Dispersion.....	62
Figure 23	Ar <i>K-L</i> Spin-Orbit Ratios .....	63
Figure 24	Cl <i>K-Edge</i> Absorption Spectrum of CCl <sub>4</sub> .....	67
Figure 25	Cl <i>K-Edge</i> Absorption Spectrum of CFC <sub>3</sub> .....	68
Figure 26	Cl <i>K-Edge</i> Absorption Spectrum of CF <sub>2</sub> Cl <sub>2</sub> .....	69
Figure 27	Cl <i>K-Edge</i> Absorption Spectrum of CF <sub>3</sub> Cl .....	70
Figure 28	Absorption Spectra on and Around the LUMO .....	74
Figure 29	Cl <i>K-L</i> X-Ray Emission Around the LUMO of the Chlorofluoromethanes ...	75
Figure 30	Cl <i>K-L</i> Peak Widths on and Around the LUMO .....	78
Figure 30a	Theoretical Plot of the Spectral Widths.....	80
Figure 31	Cl <i>K-L</i> Dispersion on and Around the LUMO .....	82
Figure 31a	Theoretical Plot of the Energy Dispersion.....	84
Figure 32	Spin-Orbit Ratio Plots of the Chlorofluoromethanes Over the LUMO .....	86
Figure 33	Cl <i>K-L</i> SO Ratios Around the LUMO.....	87
Figure 34	Cl <i>K-L</i> Polarization Ratios Around the LUMO.....	90
Figure 35	Cl <i>K-L</i> Peak Widths Over the Rydbergs.....	92
Figure 36	Cl <i>K-L</i> Dispersion Over the Rydbergs.....	94
Figure 37	O <i>K-V</i> Calculated X-Ray Dispersion of CO.....	97
Figure 38	Spin-Orbit Ratio Plots of the Chlorofluoromethanes Over the Rydbergs.....	99
Figure 39	Cl <i>K-L</i> SO Ratios Over the Rydbergs.....	100

Figure 40	Cl <i>K-L</i> Polarization Ratios Over the Rydbergs .....	101
Figure 41	Cl <i>K-L</i> Peak Widths Above the IP.....	103
Figure 42	Cl <i>K-L</i> Dispersion Above the IP.....	104
Figure 43	Cl <i>K-L</i> SO Ratios Above the IP.....	106
Figure 44	SO Ratio Oscillations Above the IP in CCl <sub>4</sub> .....	107
Figure 45	Cl <i>K-L</i> Polarization Ratios Above the IP .....	108
Figure 46	Polarized Cl <i>K-V</i> X-Ray Emission from CF <sub>2</sub> Cl <sub>2</sub> .....	112
Figure 47	Cl <i>K-V</i> Peak Widths for CF <sub>2</sub> Cl <sub>2</sub> .....	114
Figure 48	Cl <i>K-V</i> Dispersion for CF <sub>2</sub> Cl <sub>2</sub> .....	116
Figure 48a	Cl <i>K-V</i> Dispersion of all Emission Peaks for CF <sub>2</sub> Cl <sub>2</sub> .....	117
Figure 49	Cl <i>K-V</i> Peak Ratios Over the Pre-Edge Features in CF <sub>2</sub> Cl <sub>2</sub> .....	119
Figure 50	Cl <i>K-V</i> Peak Ratios Above the IP in CF <sub>2</sub> Cl <sub>2</sub> .....	121
Figure 51	Cl <i>K-V</i> Polarization Plots for CF <sub>2</sub> Cl <sub>2</sub> .....	123
Figure 52	Cl <i>K-V</i> Polarization Ratios of CF <sub>2</sub> Cl <sub>2</sub> .....	125
Figure 53	Cl <i>K-V</i> Emission Spectra of CF <sub>2</sub> Cl <sub>2</sub> at 2826.18, 2826.5 and 2826.78 eV .....	127
Figure 54	Polarized Cl <i>K-V</i> X-Ray Emission from CCl <sub>4</sub> .....	129
Figure 55	Cl <i>K-V</i> Peak Widths for CCl <sub>4</sub> .....	130
Figure 56	Cl <i>K-V</i> Dispersion for CCl <sub>4</sub> .....	131
Figure 57	Cl <i>K-V</i> Peak Ratios for CCl <sub>4</sub> .....	132
Figure 58	Cl <i>K-V</i> Polarization Plots and Polarization Ratios for CCl <sub>4</sub> .....	135
Figure 59	Polarized Cl <i>K-V</i> X-Ray Emission from CF <sub>3</sub> Cl .....	137
Figure 60	Cl <i>K-V</i> Peak Widths for CF <sub>3</sub> Cl.....	138
Figure 61	Cl <i>K-V</i> Dispersion for CF <sub>3</sub> Cl.....	140
Figure 62	Cl <i>K-V</i> Peak Ratios Over the Pre-Edge Features in CF <sub>3</sub> Cl .....	142
Figure 63	Cl <i>K-V</i> Peak Ratios Above the IP in CF <sub>3</sub> Cl.....	143
Figure 64	Cl <i>K-V</i> Polarization Plots for CF <sub>3</sub> Cl.....	145
Figure 65	Cl <i>K-V</i> Polarization Ratios of CF <sub>3</sub> Cl .....	146
Figure 66	Cl <i>K-V</i> Polarization Ratios of CF <sub>2</sub> Cl <sub>2</sub> , CCl <sub>4</sub> , and CF <sub>3</sub> Cl Over the LUMO ...	148
Figure 67	Cl <i>K-V</i> Polarization Ratios of CF <sub>2</sub> Cl <sub>2</sub> , CCl <sub>4</sub> , and CF <sub>3</sub> Cl Above the IP .....	149

## ACKNOWLEDGEMENTS

I would like to thank the following people for their knowledge and expertise; In the XAMS group, Dr. Wayne Stolte for knowing a great deal about running an experiment, Dr. Renaud Guillemin for being an expert with Igor programming, and Dr. Dennis Lindle for being the group expert on just about everything (especially x-ray emission spectroscopy and wine). I would also like to thank my family: my wonderful husband, Reynaldo, for being supportive and encouraging even when I would go to Berkeley for months at a time, my mother, Georgeanne, my Aunt Sue, and all my cousins for also encouraging me even at a young age to follow my dreams. I would like to thank Mark and Debbie in the chemistry office for running things in Las Vegas. I would also like to thank my friends and colleagues at the ALS, Dr. Stefano DeSantis in the Accelerator Physics group and Brian Fairchild in the Environmental Safety and Health group for both your support and friendship!

Finally, I would like to thank my committee members, Dr. Clemens Heske, Dr. Boyd Earl, and Dr. David Shelton for taking the time to help improve the content of this work and to my outside committee member, Dr. Peter Langhoff, for his expertise and for traveling to be at my defense.

UNLV

Chemistry Department

June 28, 2007

The author of this Dissertation,

Amanda C. Hudson,

entitled

Polarized X-Ray Emission Spectroscopy at the Cl K Edge of the  
Chlorofluoromethanes,

would like to specially acknowledge

Dr. Peter Langhoff, University of California, San Diego

who served as a Chemistry Department approved outside consulting member.

  
*Outside Consulting Member*

## CHAPTER 1

### INTRODUCTION

Until the advent of synchrotron radiation, core-level electron studies in atoms and molecules have proven difficult for many reasons. Previously, core-level studies have relied upon incident excitation by x-rays emitted by a fixed-wavelength source [1], polychromatic Bremsstrahlung radiation sources [2], or by high-energy electron impact [3]. Although these methods have yielded excellent results, and they lack the ability to selectively excite specific resonances near the ionization potential (tunability), they lack sufficient x-ray intensity required for core studies, and polarizability (for determination of orbital orientation) [4]. Synchrotron radiation (SR) alleviates all the issues surrounding core-level studies; SR provides intense (often providing  $10^{10}$  photons/second or more), tunable (at the Cl *K*-edge the resolution is 0.2 eV), and polarized (over 99% linearly polarized) x-rays throughout the regions near the ionization potential of the core levels of most elements [5].

To study core electrons, or those tightly bound to the nucleus, high-energy photons are used, namely the x-rays (or lower energy vacuum ultra-violet) produced in synchrotron radiation which have energies between 15 and 150,000 eV. These electromagnetic waves are energetic enough to ionize core electrons (especially for first and second row elements) and tunable, making excitation of specific atoms to well-defined states possible (for example, the excitation of a chlorine 1s electron to an empty molecular orbital in a molecule such as Cl<sub>2</sub>).

X-rays can be used to study matter in a number of different ways; x-rays can be absorbed by an atom or a molecule (producing a system in a core-excited state), which yields information on the vacant orbitals [6]. Also, x-rays (or electrons) can be emitted from a core-excited system to yield information on occupied orbitals [7], providing complementary information; this is x-ray emission when a photon is emitted [8] and photoemission when an electron is emitted [7]. Atoms or molecules that have been excited can relax in the following ways: a valence or outer core electron can fill the core hole and an Auger electron is emitted (electron spectroscopy) [9], or a photon of light can be emitted (x-ray emission spectroscopy) [9]. Also, a molecule can fragment upon core-excitation, a process called photofragmentation [10]. A specific type of x-ray emission spectroscopy, resonant x-ray emission, occurs when the initial absorption is to bound states (resonance) followed by relaxation of an electron into the core hole via the production of an emitted photon, and is one of the main focuses of this work [8].

In x-ray absorption, a photon of light interacts with a core electron to promote it to a higher energy state (unoccupied orbital) or to ionize it (excitation to the continuum); see Figure 1. On resonance, the incoming photon has the same energy ( $E$ ) as the transition energy, or

$$\omega = \omega_{f0}, \quad (1)$$

where  $\omega$  is the frequency ( $E = \hbar\omega$ , where  $\hbar$  is Planck's constant divided by  $2\pi$ ) of the incident photon and  $\omega_{f0}$  is the frequency of the transition between the ground state (0) and the final state ( $f$ ). When the excitation energy is greater than the ionization potential, the ejected electron carries away the excess energy.



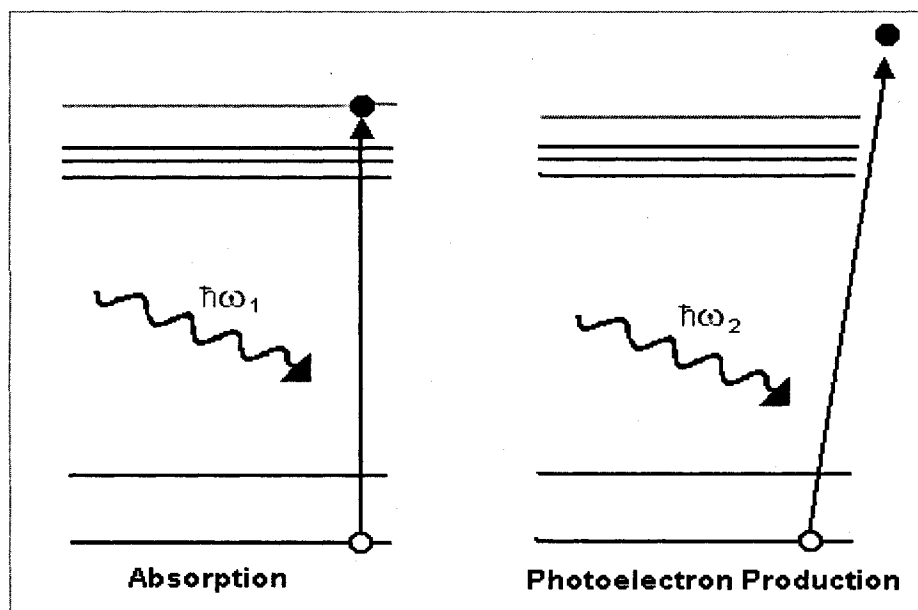


Figure 1. Illustration of absorption of an incident photon and promotion of a core electron to a well defined state (left) and the ionization of a core electron (right). In this scheme,  $\hbar\omega_2 > \hbar\omega_1$  and the gray lines represent unoccupied orbitals, the black represent occupied orbitals and only the electrons involved in these processes are shown.

In the ionization process (nonresonant x-ray absorption or excitation to the continuum), see Figure 1, one of the photons from the x-ray beam displaces an electron from a core orbital as follows:



where  $A$  can be an atom, molecule, or an ion,  $A^{+*}$  is an electronically excited ion with a positive charge one greater than that of  $A$ ,  $\hbar\omega$  is the photon energy and  $e^{-}$  is an electron that is emitted as the result of the interaction. The kinetic energy of the emitted electron can be measured with an electron spectrometer, and thus the binding energy of the electron to the nucleus can be calculated using the following:

$$E_b = \hbar\omega - E_k, \quad (3)$$

where  $E_b$  is the electron binding energy and  $E_k$  is the kinetic energy of the electron. When an atomic or molecular system absorbs a photon, part of the absorbed photon energy is used to overcome the electrostatic forces holding the electron to its orbital (binding energy), and the remainder of the energy appears as the emitted electron's kinetic energy. The binding energy of an electron is characteristic of both the atom and the orbital it arises from [11].

A core-excited system will decay to a lower energy state quite rapidly, usually within  $10^{-14}$  s due to its instability [12]. Photon emission occurs when a vacancy in a core electron shell is filled by an electron from one of the outer shells through the emission of a photon; see Figure 2. The outer shells include outer core orbitals or valence orbitals. The x-ray photon emission process from a core-excited state,  $A^*$ , can be shown as the following:

$$A^* \rightarrow A^* + \hbar\omega'. \quad (4)$$

The energy of the emitted photon  $\hbar\omega'$  is the difference between the initial and the final states of the system and, in some cases, is dependent on the excitation energy [13-15]. The result of this decay process is a valence excited state,  $A^*$ , and a photon of light; when the incident light exceeds the IP,  $A^*$  is a cation with a valence hole ( $A^{+*}$ ). X-Ray emission spectroscopy (XES), like x-ray absorption spectroscopy (XAS), is symmetry, orientational, and polarization selective and can probe the electronic structure of specific atoms in a system [4,6].

In Auger electron spectroscopy, a competitive process to x-ray emission, an electron ( $e_1$ ) fills a core hole generated by an incident x-ray and a second electron ( $e_2$ ) is ejected from the system, in the same way a photon is ejected in XES, to compensate for the energy differences in the initial and final states; see Figure 2. Auger decay occurs as follows:



The ejected electron has a characteristic kinetic energy based on the element and the orbital it is ejected from and is independent of the excitation energy, so it effectively takes a fingerprint of the sample. Auger electron emission and x-ray photon emission are competitive processes and their rates depend on the atomic number ( $Z$ ) and the energy of the core-hole of the element involved. High  $Z$  elements favor x-ray emission decay [16] channels while lower  $Z$  elements favor Auger electron emission [17]. In chlorine, the dominant decay process is Auger electron emission with x-ray emission constituting only 7% of the total decay. Of the total x-ray emission, the weak  $3p \rightarrow 1s$  emission lines represent less than one percent of the total x-ray emission, with the  $2p \rightarrow 1s$  comprising the rest of the x-ray emission (over 99% of the total x-ray emission). The strengths of Auger electron spectroscopy include its sensitivity for low  $Z$  elements and its surface sensitivity, which is in particular interest for detailed examination of a solid surface as the low energy electrons cannot escape from more than a few nanometers of the solid surface (the higher the emitted electron's energy, the deeper it can originate in the solid sample) [18].

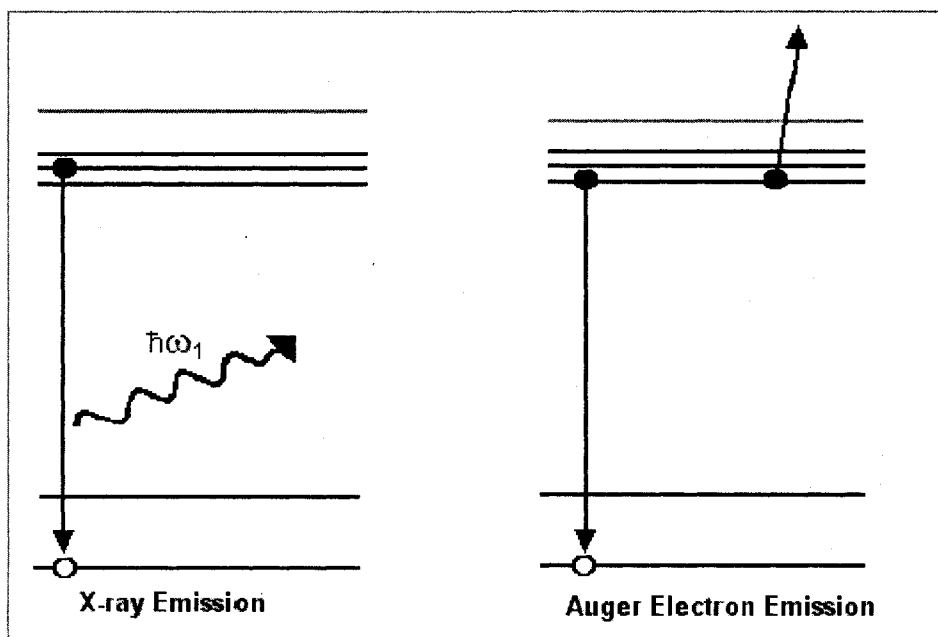


Figure 2. Illustration of the x-ray emission process (left) and the Auger electron emission process (right). Gray lines represent unoccupied orbitals, black lines represent occupied orbitals, and only the electrons involved in these processes are shown.

The final spectroscopic technique discussed in this work is resonant x-ray emission spectroscopy. In this process a photon of light is absorbed by an electron, promoting it to an unoccupied atomic or molecular orbital; see Figure 3. An outer electron fills the core hole via photon emission and the resulting atom or molecule has a valence hole, as follows:



The lifetimes of valence holes are long lived compared to core holes,  $10^{-10}$  s for the valence hole compared to  $10^{-14}$  s for the core hole. This spectroscopic technique yields information on both the unoccupied and the occupied orbitals of an electronic system, since absorption and emission are both measured. In this process, an outer core electron

or a valence electron can fill the core hole (spectator emission), also called inelastic scattering, leaving the core-promoted electron in a higher energy state, or the promoted electron can fill the core hole (participator emission), also called elastic scattering. In the first case, the emitted photon has less energy than the incoming photon and in the second, they have the same energy.

The primary spectroscopic methods used in this work are resonant x-ray emission spectroscopy and nonresonant x-ray emission spectroscopy. In both cases, the initial absorption is near the core ionization potential (IP), an energy region called near-edge x-ray absorption fine structure (NEXAFS). In NEXAFS, measurements are conducted only a few eV away from the ionization threshold; 10's of electron-volts (eV) below threshold (to include pre-edge absorption features) to 100's of eV above (to include multielectron processes and shape resonances). The pre-edge area of NEXAFS involves excitations to molecular antibonding orbitals (molecular orbitals with destructive interference) or to atomic-like Rydberg states. Rydberg states occur just below the IP; they can be excitations to specific states (like the Cl  $1s \rightarrow 4p$  Rydberg) or to a Rydberg series of states (as in the Cl  $1s \rightarrow np$  series where  $n = 5, 6, 7, \dots$ ). In most cases, Rydberg features are weaker due to decreased spatial overlap with the  $1s$  state [6]. The unoccupied molecular orbitals are lower in energy than the Rydberg states and have different characteristics dependent on the molecule ( $\sigma$  bonding environments versus  $\pi$  bonding environments, for example). Near edge spectra are valuable in that they yield information on coordinate geometry, molecular orientation, and density and symmetry of unoccupied valence electron states [19].

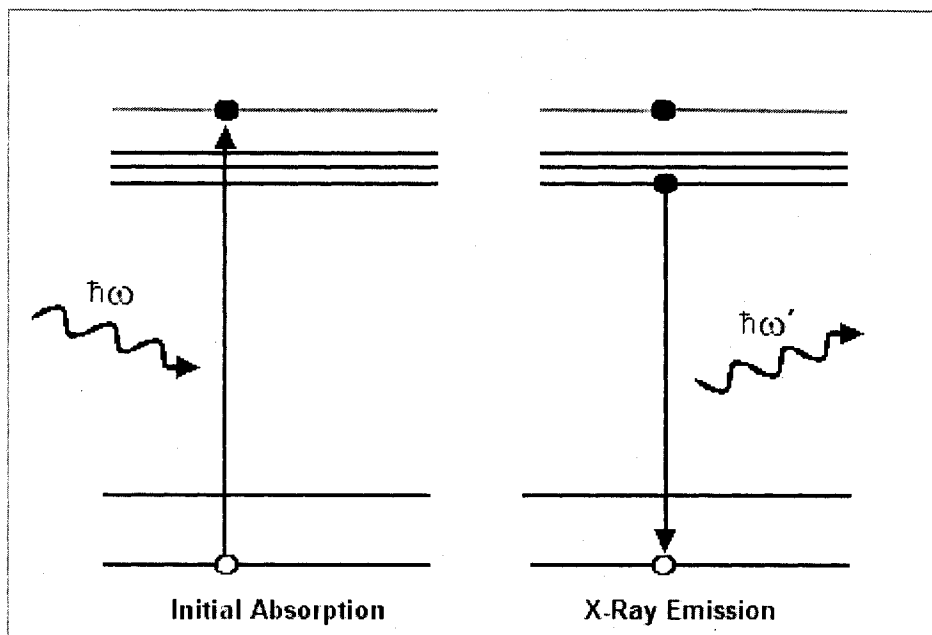


Figure 3. Illustration of the resonant x-ray emission process. In the initial absorption, an electron is promoted to an unoccupied orbital (gray line) and an electron from an outer core or a valence occupied orbital (black lines) fills the core hole. In this figure, only the electrons involved in resonant x-ray emission are shown.

## CHAPTER 2

### THEORETICAL REVIEW

The following chapter presents a review of theoretical work related to the data presented in Chapters 5 and 6. The topics in the chapter are organized as follows; the first topics presented, stimulated absorption and nonresonant x-ray emission (or emission following excitation above the ionization potential of the molecule) are the steps in the two-step theoretical model that describes x-ray fluorescence where the absorption and the emission are not coupled. The second topics, resonant x-ray emission and Raman Stokes and anti-Raman, describe scattering events, or one-step theoretical models where the emitted photon energy is dependent on the incident photon energy. The last two topics in this chapter relate to specific parameters of the data, namely the spin-orbit ratios of the *K-L* data (an outer core electron (Cl 2*p*) fills the core hole after a *K*-shell excitation) and the polarizations of the *K-V* data (a valence electron (Cl 3*p*) fills the core hole after a *K*-shell excitation).

#### Stimulated Absorption

Stimulated absorption is the first step of a theoretical two-step process that describes x-ray fluorescence. The incident photon, or x-ray, is treated as an electromagnetic wave and its interaction with an atom or molecule in the ground state is shown here. When an electromagnetic field interacts with matter, it can cause one or more electrons to be promoted to higher energy states. In most cases, the electric field of the radiation reacts

more strongly with the electrons than the magnetic field of the radiation, so the magnetic portion of the radiation is neglected and only the electric field interactions are considered, where only the first order of the interaction is considered. This is the electric dipole approximation; the selection rules arising from this approximation have been determined elsewhere [20]. The oscillating electric field of the radiation is given by the following:

$$\mathcal{E} = \mathcal{E}_0 (e^{i\omega t} + e^{-i\omega t}), \quad (7)$$

where  $\mathcal{E}$  is the electric field produced by the radiation,  $\mathcal{E}_0$  is the maximum amplitude,  $\omega$  is the frequency, and  $t$  is time [21]. When considering the sizes involved, the size of the atomic or molecular orbital is usually much smaller than the wavelength of light in question, so  $\mathcal{E}$  is said to be constant in space, but not in time; which constitutes the second part of the dipole approximation. The time-dependent Hamiltonian in this case is

$$H'(t) = V_e = -e\mathcal{E}\hat{e}_0 \cdot \vec{r} = -e\mathcal{E}_0\hat{e}_0 \cdot \vec{r}(e^{i\omega t} + e^{-i\omega t}), \quad (8)$$

where  $\hat{e}_0$  is a unit polarization vector,  $\vec{r}$  is the position vector of the electron, and  $e$  is the electron charge [21]. Applying time dependent perturbation, where the electric field constitutes the perturbation, to the system  $\Psi(0) = a_i\psi_i + a_k\psi_k$ , where  $\psi_i$  is the system in the ground state and  $\psi_k$  is the system after interacting with the electric field. At time  $t$  the expansion coefficient  $a_k(t)$  can be described by the following:

$$a_k(t) = \frac{\mathcal{E}_0 D_{ki}}{\hbar} \frac{\exp(i(\omega_{ki} - \omega)t) - 1}{\omega_{ki} - \omega}, \quad (9)$$

where  $D_{ki}$  is the dipole matrix element between states  $k$  and  $i$  and is a measure of the overlap between  $|i\rangle$  and  $|k\rangle$  and  $\omega_{ki} = (E_k - E_i)/\hbar$ .



Exposure of the system to radiation of the frequency  $\omega$  has produced a transition from state  $i$  to state  $k$  and, since  $\omega$  is positive,  $E_k > E_i$ . In this system, there is energy uptake, or absorption, and the probability of finding the system in the discrete state  $|k\rangle$  after time  $t$  if it were initially in state  $|i\rangle$  at  $t = 0$  is

$$P_k(t) = \frac{4|D_{ki}(t)|^2}{\hbar^2(\omega_{ki} - \omega)^2} \sin^2 \frac{1}{2}(\omega_{ki} - \omega)t \quad (10)$$

The amplitudes oscillate in time, known as Rabi oscillations. The rate of absorption is given by the following:

$$R_{k \leftarrow i}(t) = \frac{|a_k(t)|^2}{t} = \frac{\pi \epsilon_0^2}{2\hbar^2} |D_{ki}|^2. \quad (11)$$

In the present study, the initial state  $|i\rangle$  is the ground electronic state of the system and state  $|k\rangle$  is a core-excited or core-ionized state.

### Nonresonant X-Ray Emission

Above the ionization potential, x-ray emission is treated as a two-step process. First is the absorption process (as described above) stimulated by the presence of an x-ray, and second relaxation occurs as a spontaneous emission process and is called nonresonant x-ray emission. In quantum field theory, the electromagnetic radiation is also described using a quantum mechanical equation and the Hamiltonian of the system includes contributions from the atom and the field. This means the eigenstates obtained from solving this equation are not true energy eigenstates, but differ very slightly from the atomic energies. Perturbation theory is also used here to describe the interaction as the following:

$$H = H_0 + V' \quad (12)$$

Where  $V'$  describes the coupling of the atom to the field of quantization [22]. If we apply the time dependent perturbation theory to this state to obtain a transition rate between the initial state to a final state the following results:

$$A_{ik} = \frac{4\omega_{ik}^3}{3\hbar c^3} \frac{1}{4\pi\epsilon_0} \left| \langle k | V' | i \rangle \right|^2 \quad (13)$$

where  $A$  is the coefficient for spontaneous emission. This equation is dependent on the density of the final states of the atom-field system; which is assumed to form a continuum. From this treatment, the decay is exponential and yields a Lorentzian lineshape as the natural lineshape of atomic transitions. It has been seen that at short decay times, the system can deviate from the exponential function [23].

### Resonant X-Ray Scattering (RXS)

Above the ionization potential, the x-ray absorption and x-ray emission processes can be treated as separate events, however, on resonance, the two are coupled and must be treated theoretically as a single scattering event. The incident radiation ( $\omega$ ) and the emitted x-ray ( $\omega_1$ ) are related as follows [23]:

$$\frac{d\sigma(\omega_1, \omega)}{d\omega d\Omega} = r_0^2 \frac{\omega_1}{\omega} \sum_f |F_f|^2 \Delta(\omega_1 + \omega_{f0} - \omega, \Gamma_f), \quad (14)$$

where  $\sigma$  is the cross section (probability) of scattering,  $d\Omega$  is the solid angle of scattering,  $r_0$  is the Thompson radius (classic radius of an electron),  $\Gamma_f$  is the final state lifetime broadening,  $\omega_{f0}$  is the frequency of transition between the ground (0) and final (f) states, and

$$\Delta(\Omega, \Gamma) = \Gamma / \pi(\Omega^2 + \Gamma^2) \quad (15)$$

is a Lorentzian function with full width at half maximum (FWHM) of  $\Gamma$  and  $\Omega = \omega - \omega'$  is the resonant detuning;  $\omega$  is the frequency at the resonance maximum and  $\omega'$  is the actual photon energy. The scattering amplitude  $F_f$  is given by the Kramers-Heisenberg formula (KH) [65]:

$$F_f = F_f^T + \sum_n \sum_i F_{f,in}, \quad F_{in} = \omega_f \omega_{i0} e^{iq \cdot R_n} \left[ \frac{D'_f D_{i0}}{\omega - \omega_{i0} + i\Gamma_i} - \frac{D'^T D'_{i0}}{\omega_1 + \omega_{i0}} \right],$$

$$F_f^T = (e_1 \cdot e) \langle f | \sum e^{iq \cdot r} | o \rangle, \quad (16)$$

where  $q = p_1 - p$  is the change of x-ray photon momentum due to scattering,  $D = e \cdot D$ ,  $D' = e' \cdot D$  with  $D$  being the total electronic dipole moment of the molecule,  $\omega_f$  is the frequency of transition between the intermediate ( $i$ ) and final states ( $f$ ),  $\omega_{i0}$  is the frequency of transition between the ground and intermediate states, and  $R_n$  is the coordinate of the core-excited atom. The sum on the right hand side of  $F_f^T$  is a summation over coordinates of all  $Z$  electrons. As seen from equation 20, in the one-step model the scattering cross section is dependent on both the incident photon energy and on the final state lifetime broadening of the system in question. Specific manifestations of equation 20 are seen in the remainder of this section and in the next section.

In this work, the molecules in question are chlorofluoromethanes and all studies were conducted at the Cl  $K$ -edge (Cl 1s). For these molecules, the three resonances are Cl 1s  $\rightarrow$  molecular antibonding orbitals followed by 1s  $\rightarrow$  4p and 1s  $\rightarrow$  np Rydberg resonances. The first resonance, 1s  $\rightarrow$  lowest unoccupied molecular orbital (LUMO), is a dissociative state (dissociation occurs  $\sim$  1fs), which is strongly dependent on the duration time of resonant scattering. This time period is defined by the difference of the nuclear potential

surfaces of the final and core excited states (which are parallel in the Cl *K*-edge system).

In this case,

$$F_f = \omega_f \omega_{i0} D_{fi}^\dagger D_{io} \frac{\langle n|o \rangle}{\Omega + i\Gamma_i} \quad (17)$$

where  $|o\rangle$  and  $|n\rangle$  are the vibrational states of the ground and final states and  $\langle n|o \rangle$  is a measure of the overlap (scattering amplitude), or the Franck-Condon (FC) factor [23]. In this case,  $\sigma$  can be written as a product of a bound-free FC factor and a Lorentzian function accounting for the lifetime  $\Gamma$  as follows [15]:

$$\sigma(\omega, \omega_i) \propto \frac{F(\Omega_i - \Omega)}{\Omega_i^2 + \Gamma^2 / 4}. \quad (18)$$

In this equation,  $\Omega_i$  is the difference in energy between the measured emitted photon and the energy of an emitted photon in isolated Cl. The influence of (18) on spectral features on and around the LUMO will be further discussed in Chapters 3, 5, and 6.

The Raman-Stokes law is described as a linear dependence of the emitted x-rays on the frequency of the incident x-rays (one of the manifestations of equation 18) as follows:

$$\omega_i = \omega - \omega_{0f}. \quad (19)$$

This energy law is only strictly fulfilled for elastic scattering (where the final state energy  $f$  is explicitly known). The accuracy for which the energy of the final state is known in inelastic scattering is proportional to the inverse lifetime of the final state [24]. The linear dispersion law, a linear (for elastic scatter, the slope is equal to one) increase in the emitted peak's energy with increasing photon energy, is valid only if the final state of the RXS process is discrete with a sufficiently small lifetime broadening ( $\Gamma_f < \Gamma_i$ ).

Exceptions to this law occur when the final state is in the continuum or when the final state is dissociative [23]. Examples of this will be seen in Chapter 3.

The dispersion can become non-Raman or anti-Raman (have a negative dispersion) when the initial excitation is to several intermediate states or when the ground state is vibrationally excited. This behavior can be explained by the following [24]:

$$\varepsilon(\omega) \approx \Omega \left( \frac{\omega_i^2 - \omega_f^2}{2\omega_i^2} \right) + \varepsilon_{if}, \quad (20)$$

where  $\varepsilon(\omega)$  describes the energy dispersion,  $\omega_i$  is the (vibrational) frequency of the initial state,  $\omega_f$  is the (vibrational) frequency of the final state and  $\varepsilon_{if}$  is the frequency of the sudden (vertical) emission transition from the lowest vibrational level of the core-excited state. In the anti-Raman case, the vibrational frequency of the final state is larger than that of the initial state ( $\omega_f > \omega_i$ ) and results in a negative slope (detuning versus dispersion). Equation (26) can also explain deviations from the Raman-Stokes behavior. If the ground state is in a vibrational level of  $\nu \neq 0$  (not in the ground-state vibrational level),  $\varepsilon(\omega)$  would yield a positive slope that is different than the predicted value of one from the Raman-Stokes law [23, 24].

### Spin Orbit Splitting

A parameter of importance to the *K-L* data in Chapter 5 is the spin-orbit splitting. This describes the characterization of electrons in core orbitals (like Cl 2*p*). When characterizing outer core electrons, it is most useful to use the total angular momentum quantum number (*j*). The total angular momentum quantum number is calculated using

the orbital angular momentum from the orbital in which the electron resides ( $\ell$ ) and the electron-spin ( $s$ ) as follows [25]:

$$j = \ell + s, \ell + s - 1, \dots, \ell - s. \quad (21)$$

The quantum number projection of the total angular momentum ( $m_j$ ) is found by applying raising and lowering operators to the total spin eigenfunction to yield the following:

$$m_j = -j, -j + 1, \dots, j - 1, j. \quad (22)$$

The  $m_j$  values are found in the same way the orbital angular momentum ( $m_\ell$ ) values are calculated from the angular momentum eigenstates ( $\ell$ ); see Appendix I. In the first part of this work, the decay channel arising from the Cl 1s excitation is a photon emission via a 2p electron filling the core hole. For 2p electrons,  $\ell = 1$  and  $s = \frac{1}{2}$  which yields

$j = \frac{3}{2}, \frac{1}{2}$  and corresponds to the  $2p_{3/2}$  and the  $2p_{1/2}$  states. The following  $m_j$  values are then obtained:

$$\begin{aligned} m_j(2p_{3/2}) &= \frac{3}{2}, \frac{1}{2}, -\frac{1}{2}, -\frac{3}{2} \\ m_j(2p_{1/2}) &= \frac{1}{2}, -\frac{1}{2} \end{aligned} \quad (23)$$

Equation (23) predicts  $2p_{3/2}$  to have twice as many states as the  $2p_{1/2}$  and therefore twice the intensity in the x-ray emission spectrum when there are no molecular contributions. The spin-orbit ratios for argon have been measured at the  $K$ - $L$  energy range previously [26] and are reported in Chapter 4. In this atom, the statistical 2:1 SO ratio is achieved at energies above the ionization energy of the 1s electron, just as predicted above.

### Polarization

In the  $K$ - $V$  data in Chapter 6, the most significant parameter is the polarization.

Because the valence electrons are involved in bonding, their orientation and shape is

dependent on molecular symmetry. Described in detail in Chapter 3, excitation of a core electron to well-defined molecular orbital (like a Cl 1s electron to an antibonding orbital which is symmetric about the C–Cl molecular axes) produces an aligned system that is frozen during the emission process making polarization measurements possible.

Polarization measurements can characterize orbitals based on their orientation relative to the symmetry axis since the orientation of the molecule is known. Measurements of polarized Raman scattering dispersed with frequency (energy)  $\omega_1$  for incident photon energy  $\omega$  can be calculated using a variation on equation (14). In this case, the differential cross section becomes [27]:

$$\frac{d\sigma^{(\parallel, \perp)}(\omega)}{d\omega_1 d\omega} = \frac{\sigma^{(\parallel, \perp)}(\omega)}{4\pi} \{1 + \beta^{(\parallel, \perp)}(\omega) P_2(\cos \theta_1)\} \delta(E_0 + \omega - E_1 - \omega_1), \quad (24)$$

where  $\beta^{(\parallel, \perp)}$  is the scattering anisotropy,  $P_2$  is the polarization factor and is the second Legendre polynomial<sup>1</sup>,  $\theta_1$  is the scattering angle of the emitted photon,  $E_0$  is the ground state energy, and  $E_1$  is the final molecular energy. The spectra of radiation scattered with energy  $\omega_1$  for each of the two final state polarizations ( $\parallel$ ,  $\perp$ ), where  $\parallel$  polarization is parallel to the incident photon's polarization and  $\perp$  is polarization perpendicular to the incident photon's polarization, is given by the following:

$$dI^{(\parallel, \perp)}(\omega_1) = \sum_{(1)} I_0(\omega_1) \frac{\sigma^{(\parallel, \perp)}(\omega_1)}{4\pi} \{1 + \beta^{(\parallel, \perp)}(\omega_1) P_2(\cos \theta_1)\} d\omega d\omega_1, \quad (25)$$

where  $I_0(\omega_1)$  is the spectrum of linearly polarized radiation with electric field vector  $e_1$ , and the sum over (1) includes all final states in the measured interval  $d\omega_1$  which satisfy the energy conservation law  $h\omega_1 = h\omega + E_0 - E_1$ . This equation predicts the polarized

---

<sup>1</sup> A solution to the Legendre differential equation,  $P_2(x) = \frac{1}{2}(3x^2 - 1)$ .

emission spectra in the parallel and the perpendicular directions where a peak that is more intense in the parallel direction than in the perpendicular is said to be oriented largely along the main symmetry axis. The polarization,  $P(\omega_l, \theta_\beta)$ , in the interval  $d\omega_l$  is defined as

$$P(\omega_l, \theta_\beta) \equiv \frac{dI^{(||)}(\omega_l) - dI^{(\perp)}(\omega_l)}{dI^{(||)}(\omega_l) + dI^{(\perp)}(\omega_l)} \quad (26)$$

where  $I^{(||)}$  is the intensity in the parallel direction and  $I^{(\perp)}$  is the intensity in the perpendicular direction. State-to-state line polarizations are given by the following:

$$P_{0 \rightarrow 1}(\omega_l, \theta_\beta) = \frac{P_2(\cos \theta_\beta) - 1}{P_2(\cos \theta_\beta) - 2/\beta(\omega_l)}. \quad (27)$$

The term  $\beta(\omega_l)$  is related to  $\beta^{(||, \perp)}(\omega_l)$  by the following:

$$\beta^{(||)}(\omega_l) = \frac{-2\beta(\omega_l)}{2 + \beta(\omega_l)} \text{ and } \beta^{(\perp)}(\omega_l) = 0 \quad (28)$$

Line polarization values will cover a maximum allowable range of +1 to -1 only at a scattering angle of  $\theta_l = 90^\circ$  and this range will be minimum at  $\theta_l = 0$  or  $180^\circ$ , due to the dependence of  $\cos \theta_l$ . Also, there will generally be less sensitivity of the line polarization values to the scattering anisotropy at smaller  $\theta_l = 0^\circ$  (parallel), scattering angles than at  $\theta_l = 90^\circ$  (perpendicular). At the specific case of  $\theta_l = 90^\circ$ , the emission spectra of (25) are

$$dI^{(||, \perp)}(\omega_l) = \sum_{\beta} I_0(\omega_l) \frac{\sigma^{(||, \perp)}(\omega_l)}{4\pi} \{1 - \frac{1}{2}\beta^{(||, \perp)}(\omega_l)\} d\omega_l, \quad (29)$$

the corresponding line polarization is

$$P(\omega_l, 90^\circ) = \frac{\sum_{\beta} \sigma(\omega_l) \{3\beta(\omega_l)\}}{\sum_{\beta} \sigma(\omega_l) \{\beta(\omega_l) + 4\}}, \quad (30)$$



and the state-to-state polarization is

$$P_{0 \rightarrow 1}(\omega_1, 90^\circ) = \frac{3\beta(\omega_1)}{\beta(\omega_1) + 4}. \quad (31)$$

Measurements of the line polarization provide the ratio of values given in equation (31).

### Resonance Approximation and Classical Limits

It is useful to examine the limits when the two-step scattering model approaches the classical limit of a two-step photon in and photon out process. In this limit, there is only electronic resolution and the measurements effectively sum over photon contributions from all vibrational states associated with a specific final electronic state. In this case, the scattering cross section is dependent on the dipole absorption and emission electronic transition moments ( $a^{el}$ ,  $b^{el}$ , respectively). The state-to-state line polarization in such a case can be described as the following [27]:

$$P_{0 \rightarrow 1}^{el}(\omega, 90^\circ) = \frac{3\cos^2 \gamma_{ab} - 1}{\cos^2 \gamma_{ab} + 3}. \quad (32)$$

Equation (32) is a two-step expression (absorption followed by emission) obtained by exploring the classical limits, where there is a sum over all intermediate and the final vibrational states in the resonant scattering picture. In this picture, equation (31) will reduce down to equation (32) when only electronic resolution is considered. This result was calculated by Jablonski [69] and used to describe the polarization of x-ray emission in [4].

## CHAPTER 3

### EXPERIMENTAL REVIEW

The topics in the following Chapter relate to phenomena that are measured experimentally. The first section, resonant x-ray scattering (RXS), is a review of some of the early works in the field and provides the background for the rest of the chapter. The first section is essentially the birth of the field of resonant x-ray scattering. The following sections, angular distribution and polarization, lifetime-vibrational interference, screening, parity selection and forbidden transitions (nondipole), and molecular field effects are specific topics of resonant x-ray scattering and will be discussed in great detail. The last topics, assigning x-ray absorption using x-ray emission and ultrafast x-ray emission spectroscopy are specific applications of resonant x-ray scattering.

#### Resonant X-Ray Scattering (RXS)

Resonant x-ray emission spectroscopy has been a tool used to characterize atomic and molecular orbitals for many decades. Some of the first studies were conducted on copper using early synchrotron sources or elemental x-ray tubes [8, 13, 28, 29]. From these early experiments, it was found that the linewidth of the scattered x-ray radiation was narrower than the lifetime width of the fluorescence, or the linewidth is dependent on the excitation beam and not the lifetime width on resonance [8,13]. This finding made a distinction between x-ray scattering on resonance (a one-step theoretical model) and absorption followed by emission above the ionization potential (a two-step model).

Further confirmation of this can be seen when examining the peak widths and the x-ray dispersion versus the incident photon energy, see Figure 4. In this figure, there is a linear (Raman-Stokes) increase of peak position with incident photon energy and the emission can be described as a scattering event. When the emission is fluorescence, the peak position remains constant (when the detuning is greater than +1.0 eV). For the peak widths, there is a sharp decrease in width with increasing photon energy where it reaches a minimum on resonance and begins to increase again (scattering, RXS). When it is above the IP, the peak widths remain constant (fluorescence, XES) and are 30% larger than those on resonance; the same trends have been seen in the x-ray emission spectra of Xe as well [14]. This study of Cu led to many experimental and theoretical investigations of RXS. Some of the relevant findings are reviewed in the following sections.

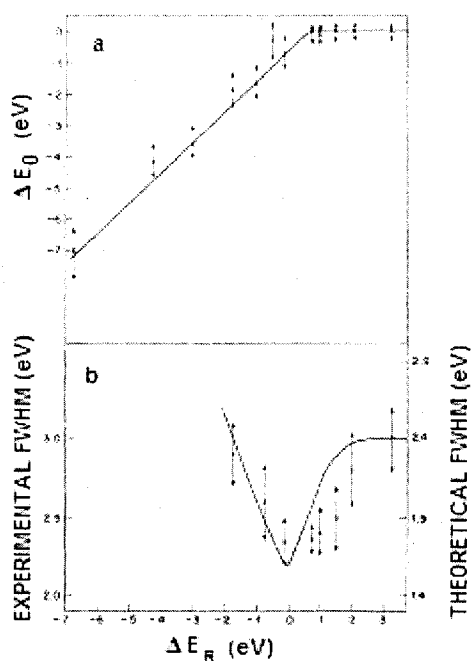


Figure 4. Cu experimental x-ray dispersion (a) and peak widths (b) around the  $K$  absorption edge measured by Eisenberger et al. [13].

## Angular Distribution and Polarization

### *Cl K-Edge*

Polarized resonant x-ray emission spectroscopy (an angular distribution measurement) is also a powerful tool in determining molecular symmetries, electronic structures, and molecular dynamics [4, 30, and 15]. In RXS, the initial absorption is to a well-defined state with a specific orientation relative to the axis of symmetry in the molecule and an aligned condition can be produced even in gas samples [4]. Fluorescence occurs on a timescale much shorter than molecular tumbling periods ( $10^{-14}$  s compared to  $10^{-10}$  s), and any alignment produced by the initial absorption is retained during the emission process making polarization measurements possible. The degree of polarization of the fluorescence depends on the incident excitation energy; which has been demonstrated in many gas phase molecules by measuring the *K-V* x-ray emission [4, 30-39]. In these molecules, the degree and the direction of polarization was observed to change with the excitation energy and with the symmetry of the occupied valence MO involved in the emission process. This proves to be a valuable tool to study symmetries of occupied and unoccupied orbitals, anisotropies in absorption and emission, and orientational and geometrical information of the system.

In  $\text{CH}_3\text{Cl}$  [4], the  $7a_1 \rightarrow 1a_1$ <sup>1</sup> x-ray emission is stronger in the parallel orientation relative to the  $3e \rightarrow 1a_1$  (which is more intense in the perpendicular direction); both of these molecular orbitals contain a significant amount of Cl  $3p$  character; see Figure 5. This result is expected given that the initial absorption ( $1a_1 \rightarrow 8a_1$ ) has the same symmetry

---

<sup>1</sup> Here,  $a_1(e)$  is a molecular orbital defined by the irreducible representations of the molecule's point group symmetry and can be obtained from character tables.

as the  $7a_1$  orbital; or they are both polarized along the symmetry axis. Above the IP, the polarization effect diminishes and the emission is largely isotropic.

Molecular orbital and static exchange calculations were performed on the  $8a_1$ ,  $7a_1$ , and  $3e$  molecular orbitals. They showed that the  $8a_1$  and the  $7a_1$  axes were oriented along the symmetry axis and with intensity over both the carbon and the chlorine atoms. The  $3e$  orbital occurred perpendicular to the symmetry axis and is largely the chlorine lone pair of electrons. Since the  $8a_1$  orbital is oriented along the molecular symmetry axis, the molecules that are excited are those with their symmetry axes oriented mostly in the synchrotron radiation polarization direction. The resulting emission reflects the molecular alignment produced by the absorption step. The  $7a_1 \rightarrow 1a_1$  (peak C) emission band is also oriented along the symmetry axis so it is stronger than  $3e \rightarrow 1a_1$  (peak B) when viewed in the parallel direction.

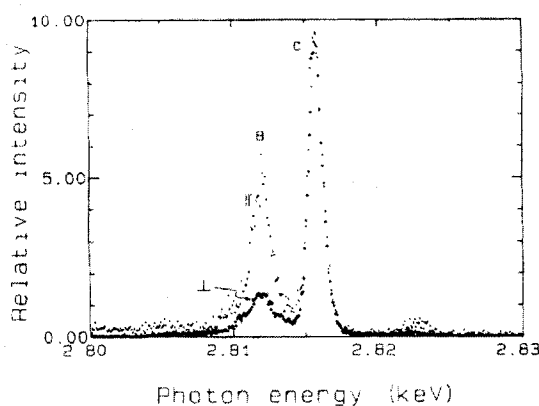


Figure 5. Polarized x-ray emission spectrum of  $\text{CH}_3\text{Cl}$  in the parallel and perpendicular orientations, where the two spectra are normalized to the height of peak C, measured by Lindle et al [4].

The study of polarized x-ray emission was soon after broadened and measurements were conducted on three similar compounds; chlorotrifluoromethane ( $\text{CF}_3\text{Cl}$ ), trichlorofluoromethane ( $\text{CFCl}_3$ ), and dichlorodifluoromethane ( $\text{CF}_2\text{Cl}_2$ ) [30, 31]. In these examinations, the molecular contributions and the molecular orientations of the x-ray emission when the excitation energy was to the lowest unoccupied molecular orbital (LUMO) were of primary focus.

Like the previous work done on  $\text{CH}_3\text{Cl}$ , the three chlorofluoromethanes show significant polarization effects on the main resonance; see Figure 6 [30]. The absorption and emission spectra of  $\text{CFCl}_3$  are more complicated due to the three chlorine atoms. The six chlorine  $1s$  electrons reside in two molecular orbitals, the  $1a_1$  and the  $1e$  (molecular) core orbitals. The presence of three chlorine atoms also triples the number of Cl  $3p$  electrons, increasing the number of valence MO's that can interact with the Cl  $1s$  hole. Resonant excitation was tuned to the  $1a_1$ ,  $1e \rightarrow 11e$  transitions, which are near degenerate at 2822.8 eV. There are three emission peaks in the  $\text{CFCl}_3$  emission spectrum; peaks A, B and C, see Table 1 for energies and assignments.

There is a rather dramatic polarization effect observed in  $\text{CFCl}_3$ . Peaks A and B essentially disappear in perpendicular polarization. The  $1e$ ,  $1a_1 \rightarrow 11e$  absorption followed by the  $7e \rightarrow 1e$ ,  $1a_1$  and the  $8e \rightarrow 1e$ ,  $1a_1$  emission are strongly polarized parallel to the synchrotron radiation; the  $1e \rightarrow 11e$  and the  $8e$  ( $7e$ )  $\rightarrow 1e$  transitions occur along the symmetry axis which is parallel to the SR polarization which explains the increased intensity in the parallel orientation.

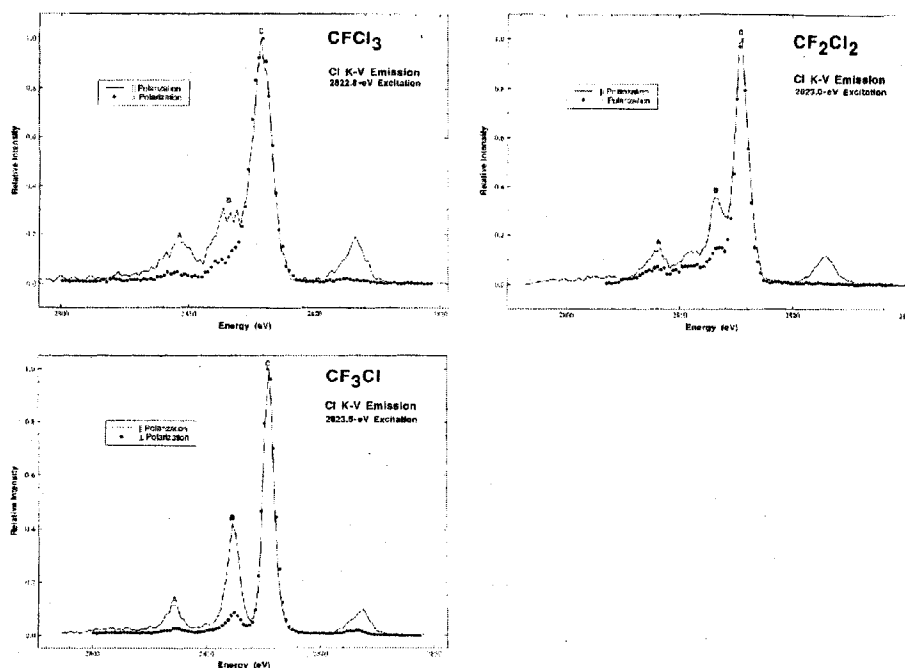


Figure 6. X-ray emission spectra of  $\text{CFCl}_3$ ,  $\text{CF}_2\text{Cl}_2$ , and  $\text{CF}_3\text{Cl}$  in the parallel and perpendicular orientations measured by Lindle et al [30], where the high-energy peak in the parallel direction is the elastically scattered “Rayleigh” peak.

Unlike the other molecules studied,  $\text{CF}_2\text{Cl}_2$  has  $\text{C}_{2v}$  symmetry while all the other molecules in this study have  $\text{C}_{3v}$  symmetry (see Appendix III for character tables). The reduction of symmetry results in the addition of more valence MO's. The Cl valence electrons reside in 10 molecular orbitals that contribute to three main emission peaks, see Table 1. Excitation in  $\text{CF}_2\text{Cl}_2$  is from the  $1a_1, 1b_2 \rightarrow 13a_1, 9b_2$  molecular orbital at 2823.1 eV. Like  $\text{CFCl}_3$ , the low energy peaks (peaks A and B) are strongly polarized in the parallel orientation. This spectrum is more complicated than those of  $\text{CFCl}_3$  and  $\text{CF}_3\text{Cl}$  and polarization effects are not dominating the emission profile [30].

Table 1. Energies and assignments of Cl *K-V* x-ray emission peaks of CFCl<sub>3</sub>, CF<sub>2</sub>Cl<sub>2</sub>, and CF<sub>3</sub>Cl taken from [30] and [31].

<i>Peak</i>	<i>Energy</i>	<i>Assignment</i>
<b>CFCl<sub>3</sub></b>		
Resonance	2822.8 eV	1a <sub>1</sub> , 1e → 11e
A	2811.5 eV	7e → 1a <sub>1</sub> , 1e
B	2814.5 eV	8e → 1a <sub>1</sub> , 1e
C	2816.7 eV	11a <sub>1</sub> , 9e, 10e, 2a <sub>2</sub> → 1a <sub>1</sub> , 1e
<b>CF<sub>2</sub>Cl<sub>2</sub></b>		
Resonance	2823.0 eV	1a <sub>1</sub> , 1b <sub>2</sub> → 13a <sub>1</sub> , 9b <sub>2</sub>
A	2810.4 eV	10a <sub>1</sub> , 4b <sub>1</sub> , 6b <sub>2</sub> → 1a <sub>1</sub> , 1b <sub>2</sub>
B	2813.1 eV	11a <sub>1</sub> , 2a <sub>2</sub> → 1a <sub>1</sub> , 1b <sub>2</sub>
C	2816.5 eV	12a <sub>1</sub> , 3a <sub>2</sub> , 6b <sub>1</sub> , 7b <sub>2</sub> , 8b <sub>2</sub> → 1a <sub>1</sub> , 1b <sub>2</sub>
<b>CF<sub>3</sub>Cl</b>		
Resonance	2823.5 eV	1a <sub>1</sub> → 11a <sub>1</sub>
A	2810.1 eV	4e, 9a <sub>1</sub> → 1a <sub>1</sub>
B	2815.1 eV	10a <sub>1</sub> , 5e → 1a <sub>1</sub>
C	2817.1 eV	7e → 1a <sub>1</sub>

In CF<sub>3</sub>Cl, the resonant x-ray emission spectrum was taken while tuned to the excitation of a Cl 1s electron to the 11a<sub>1</sub> molecular orbital at 2823.5 eV. Like the other molecules, three peaks can be seen in the corresponding emission spectra; see Table 1. There are five valence orbitals in CF<sub>3</sub>Cl with partial 3p character that can fill the core hole. These are 7e, 10a<sub>1</sub>, 5e, 9a<sub>1</sub>, and 4e, see Table 1. Since CF<sub>3</sub>Cl has the same symmetry as CH<sub>3</sub>Cl, the excitation and emission transitions are analogous.

Using modified neglect of diatomic-overlap (MNDO) calculations, the amount of 3p character in the chlorofluoromethanes was computed to complement the emission spectra measured above [31]. In these calculations, the molecular geometry was varied to minimize the orbital energy, while retaining the proper ground-state molecular symmetry.



Trichlorofluoromethane ( $\text{CFCl}_3$ ) has 32 valence electrons that reside in 11 different valence molecular orbitals. These 11 orbitals are  $7a_1$ ,  $8a_1$ ,  $6e$ ,  $9a_1$ ,  $10a_1$ ,  $7e$ ,  $8e$ ,  $11a_1$ ,  $9e$ ,  $10e$ , and  $2a_2$ . The lowest unoccupied molecular orbitals are  $12a_1$ ,  $11e$ , and  $13a_1$  and are involved in absorption. A large portion of the chlorine  $3p$  character lies in six valence MO's. These are  $2a_2$ ,  $10e$ ,  $9e$ ,  $11a_1$ ,  $8e$ , and  $7e$ . Peak A is largely dominated by the  $7e$ ,  $8a_1$ , and the  $10a_1$ , peak B by the  $8e$ , and peak C by  $2a_2$ ,  $10e$ ,  $11a_1$ , and  $9e$ . From this, peak C is expected to have the most intensity followed by peak B and finally peak A; as seen in the emission profile; refer to Table 1.

Dichlorodifluoromethane ( $\text{CF}_2\text{Cl}_2$ ) has 32 valence electrons in 16 different valence molecular orbitals; which include  $7a_1$ ,  $2b_1$ ,  $8a_1$ ,  $6b_2$ ,  $9a_1$ ,  $7b_2$ ,  $10a_1$ ,  $3b_1$ ,  $11a_1$ ,  $2a_2$ ,  $4b_1$ ,  $8b_2$ ,  $12a_1$ ,  $3a_2$ ,  $5b_1$  and  $9b_2$ . The lowest unoccupied orbitals involved in absorption are the  $13a_1$ ,  $10b_2$ ,  $14a_1$ , and  $6b_1$ . Most of the chlorine  $3p$  character resides in five orbitals, the  $9b_2$ ,  $3a_2$ ,  $5b_1$ ,  $12a_1$ , and  $8b_2$ . Four other orbitals contain a significant amount of chlorine  $3p$  character as well, the  $11a_1$ ,  $7b_2$ ,  $10a_1$  and  $8a_1$ . These latter orbitals also include large amounts of carbon and fluorine character as well as some Cl  $3s$  character. The main contribution to peak A is from the  $10a_1$ ,  $7b_2$ , and the  $8a_1$  molecular orbitals, peak B is the  $11a_1$ , and peak C is the  $9b_2$ ,  $3a_2$ ,  $5b_1$ , and the  $12a_1$ . From this calculation, peak C has the most Cl  $3p$  character, and is the most intense, followed by peak A and then peak B. This trend is seen in the emission spectra, see Figure 6 and Table 1.

Chlorotrifluoromethane ( $\text{CF}_3\text{Cl}$ ) has 32 valence electrons in the following orbitals:  $6a_1$ ,  $3e$ ,  $7a_1$ ,  $8a_1$ ,  $9a_1$ ,  $4e$ ,  $5e$ ,  $1a_2$ ,  $6e$ ,  $10a_1$ , and  $7e$ . The first three unoccupied orbitals are  $11a_1$ ,  $12a_1$ , and  $8e$  in order of increasing energy. The results from the MNDO calculation showed that the  $7e$  and the  $10a_1$  orbitals contained the most chlorine  $3p$  character and the

6e and the  $1a_2$  orbitals contained the least (these orbitals are largely fluorine 2p). The rest of the remaining valence orbitals contain various amounts of chlorine 3p character. From this information, it is expected that the emission peaks are dominated by the transitions from the 7e (peak C) and the  $10a_1$  (peak B) to the  $1a_1$  and that peak A will have the least intensity, which is seen in the emission spectra; Figure 6 and Table 1.

### *C K-Edge*

The angular distributions of Rydberg resonances in CO were also studied using RXS at the C K-edge [32, 33]. Resonant x-ray spectra were recorded by exciting the core 1s electron to the  $3s\sigma$  and the  $3p\pi$  Rydberg resonances; see Figure 7. Emission spectra were taken at two different angles,  $0^\circ$  and  $90^\circ$  with respect to the polarization of the synchrotron radiation. For transitions where a core hole, after initial excitation is to an  $\sigma$  orbital, is filled by an  $\sigma$  electron, the emission intensity is maximum at  $\theta = 90^\circ$  and is minimum at  $\theta = 0^\circ$ . This is because the molecule is essentially aligned with its axis in the direction of the incident photons' electric field vector. For transitions involving an  $\pi$  orbital, the maximum is at  $\theta = 0^\circ$  and the minimum is at  $\theta = 90^\circ$ . When the initial excitation is to an  $\pi$  orbital, the trend is reversed, and the molecule is aligned with its nuclear axis perpendicular to the linear polarization vector of the incident x-ray beam. When the excitation is tuned to the C  $1s \rightarrow 3s\sigma$  Rydberg resonance, the intensity of the  $1\pi$  band at  $\theta = 0^\circ$  is larger than at  $\theta = 90^\circ$ , as opposed to the  $3p\pi$  spectra where the intensity is largest at  $\theta = 90^\circ$ . Similar anisotropy was also seen in the  $4s\sigma_g$  and the  $4p\pi_u$  Rydberg resonances in  $N_2$  [34].

Although these measurements were not polarization-sensitive, i.e. they do not select a polarization angle to measure (and therefore reject all others), but simply by measuring in

two spectrometer angles, they were able to study the angular dependence of the emitted x-rays (or the change in spectra with respect to the spectrometer angle) by directly comparing the intensities in the  $\theta = 0^\circ$  and the  $\theta = 90^\circ$  spectrometer angles. Polarization-dependent and angle-dependent measurements provide complementary information in that they are probing an aligned system of core-excited molecules; which agrees with Lindle et al who measured the polarization and the angular distribution of  $\text{CF}_3\text{Cl}$  [56].

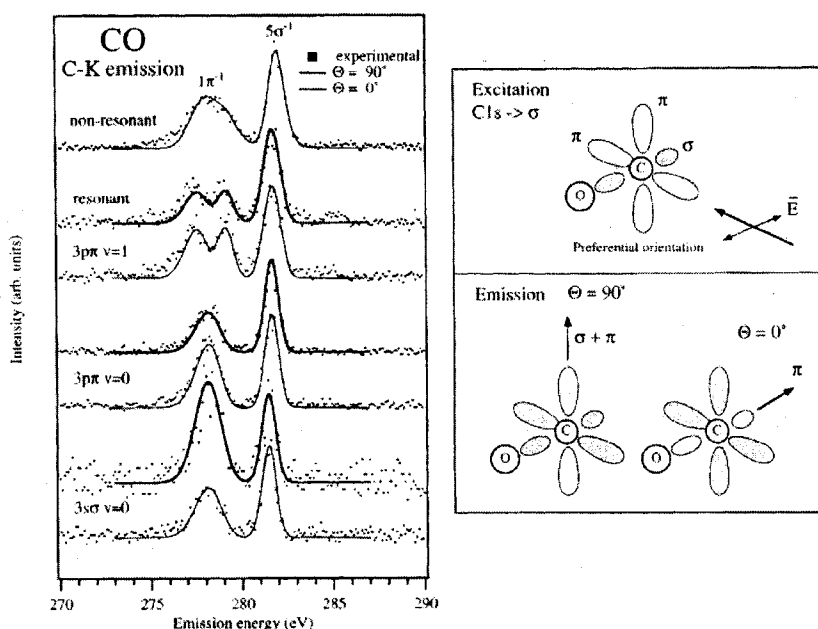


Figure 7. X-Ray emission spectra at the C *K*-edge from CO on the  $3p\pi$  and the  $3s\sigma$  Rydberg resonances (left) in the parallel ( $\theta = 0^\circ$ ) and the perpendicular ( $\theta = 90^\circ$ ) orientations. Schematic picture illustrating the anisotropy in resonant emission (right) when excitation is to an  $\sigma$  orbital from [32].

From studying these molecules, it has been seen that the degree and the direction of x-ray polarization is sensitive to the initial excitation energy in the core-level region and to the symmetry properties of the valence molecular orbitals involved in the x-ray

emission process. These studies led to further investigations of the lifetime-vibrational interference, screening of the promoted electron, nondipole x-ray emission effects in molecules, and ultra-fast RXS.

### Lifetime-Vibrational Interference

Lifetime-vibrational interference effects were found to dramatically influence the Auger decay of diatomic molecules depending on the initial excitation [68]. Diatomic molecules were chosen as there is only one degree of freedom (no vibronic coupling). Interference effects can lead to changes in the lineshape of the transition by modulation of the population of the final state vibrational levels (or due to excitation of several final vibrational states). These experiments essentially probe the development of the wavefunction of the core excited state on the timescale of the core hole decay time, which is a few femtoseconds; this timescale is much shorter than the period of one vibrational cycle of the nuclei. Interference effects thus occur when spacing between vibrational levels is comparable to the lifetime width where the largest effect was seen in O<sub>2</sub>. In this molecule, there are dramatic changes in the Auger lineshapes for the O  $1\sigma_u^{-1}1\pi_g^3$  decay into the  $1\pi_g^1$  ground state. On the low energy side of the absorption resonance, the main emission peak is almost symmetric but as the incident photon energy is increased over the resonance, a distinct low-energy tail develops and the kinetic energy of the leading edge increases. At large vibrational excitations, and increased equilibrium bond lengths ( $v > 15$ ), the FC overlap integrals are dominated by the contributions from the classical turning points, resulting in the two-peak structure.

The role of lifetime-vibrational interference effects in the resonant x-ray emission spectra of N<sub>2</sub> and CO was also examined [34, 35]. Because the lifetime width of the core-excited state is of the same order of magnitude as the spacing of the vibrational levels, an excitation of several vibrational levels could occur for each photon energy; this leads to lifetime-vibrational interference. Since all the vibrational levels can decay into the same final state, the excited levels can cause interference effects. In CO [35], the [C 1s<sup>-1</sup>] 2π<sup>1</sup> core excited state has an equilibrium bond length slightly longer than that of the ground state, and the vibrational energy is more than twice the natural lifetime width of the core-excited state. The [O 1s<sup>-1</sup>] 2π<sup>1</sup> core excited state has a significantly longer bond length, leading to the excitation of multiple vibrational levels. The lifetime width is approximately equal to the vibrational spacing in the [O 1s<sup>-1</sup>] 2π<sup>1</sup> core excited state; yielding a broad, structureless band in the O K emission spectrum, see Figure 8.

For the carbon vibrational profile, three bands are clearly seen,  $v = 0, 1$ , and  $2$ , see Figure 8. At  $v = 0$ , there is almost no excitation of the other two states; at the  $v = 1$  and  $v = 2$  levels, however, vibrational interference is greater and all three levels can be excited. This results in large interference effects that are observed in the emission profile; the peak shape changes dramatically depending on what vibrational levels are excited, or the emission peaks change dramatically over the absorption resonance. In the oxygen case, vibrational interferences occur at all excitation energies, see Figure 8. To properly describe the band profiles in the oxygen emission spectra it is necessary to include the interference contributions. For carbon, however, the interference effects are important only at higher vibrational levels. The same trend at the C K-edge is seen at the N K-edge in N<sub>2</sub> [34]. The lifetime-vibrational interference effects are strong at excitations above

the  $v = 1$  vibrational level, especially at  $v = 3$  and 4 and essentially no effects are present at  $v = 0$  or at  $v = 1$  in  $N_2$ .

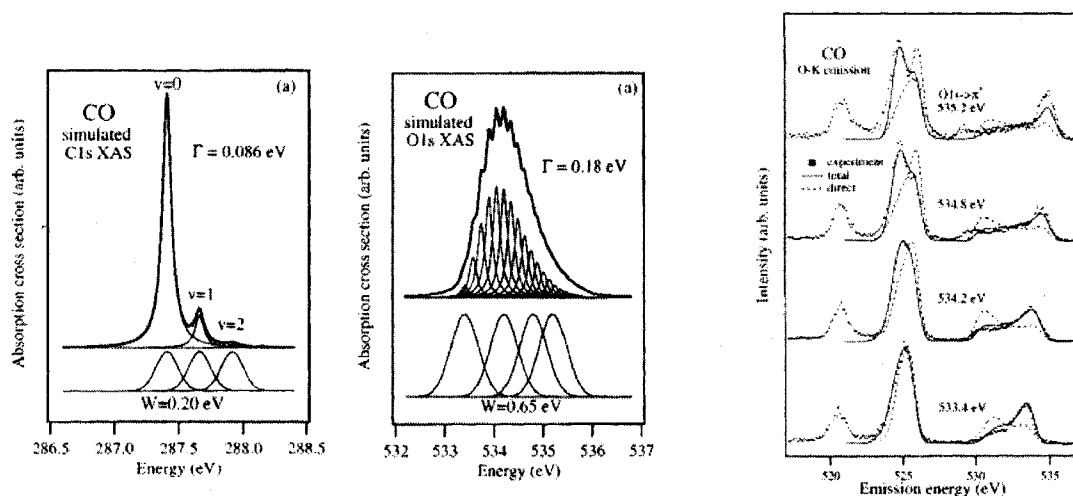


Figure 8. Simulated C 1s x-ray absorption spectrum for the  $v = 0, 1$ , and 2 levels (right) and the simulated O 1s absorption spectrum of many vibrational levels (center) and simulated O x-ray emission showing the interference (right) effects from [35].

## Screening

Screening occurs when an electron promoted to an empty MO screens differently the decay of valence or outer core electrons to the core, which can result in energy shifts and intensity differences. In some instances, the creation of a core hole can cause screening with the penetration of valence electrons into the core; this is dependent on the core-hole and the valence contributions [36]. Screening calculations were performed on a number of molecules to determine the role of screening in different systems [35, 36]. Three types of screening were studied; valence effects (CO and  $H_2CO$ ), Rydberg effects ( $H_2O$ ), and core-level effects ( $H_2S$  and  $CF_3Cl$ ). The largest effect was seen in valence screening of CO and  $H_2CO$  where the spectator electron influences the valence emission. In CO [35],

the valence  $\pi^*$  orbital is largely localized on the carbon atom (to counter the  $1\pi$  localization on oxygen), making the  $C\ 1s \rightarrow \pi^*$  absorption a factor of three more intense than the  $O\ 1s \rightarrow \pi^*$  transition. There is significant screening in both the O and the C emission spectra from the  $5\sigma$  molecular orbital and a small effect from the  $1\pi$  orbital. The screening in carbon is self-screening (by the  $\pi^*$  since it is largely localized on the C atom) and the oxygen screening is from the rearrangement of the occupied orbitals [23]. This was confirmed experimentally where energy of the  $5\sigma$  emission band is downshifted by 2.9 eV and the  $1\pi$  emission band is downshifted by 0.6 eV. Energy in the O-K emission spectrum are downshifted 2.9 eV for the  $5\sigma \rightarrow 1\sigma$  transition and 0.8 eV for the  $1\pi \rightarrow 1\sigma$  transition [39]. The same trend is observed in  $H_2CO$  but the oxygen HOMO is more intense and the carbon is screened more than the oxygen, which is the opposite of CO [36].

In water, excitation is to an oxygen Rydberg state and the screening is predicted by Skytt [35] to be substantially reduced. This is because Rydberg orbitals are less penetrating than valence orbitals and magnitudes of the screening energies depend on the degree to which the spectator electron penetrates the molecular ion core. In  $H_2O$ , the energy of the  $1b_1$  (HOMO)  $\rightarrow 1s$  is only down-shifted by 0.9 eV; which agrees well for the energy shifts predicted for the CO Rydberg shifts.

Finally, core-level screening was observed in  $H_2S$  and  $CF_3Cl$  [36]. In core-level screening, screening occurs between different core-levels, which can be either main ( $K, L, \dots$ ) or from a subshell ( $L_I, L_{II}, \dots$ ). In these cases, the promoted electron acts in the same way as a chemical shift; which produce observable effects in the x-ray emission spectra. Energy shifts of  $\approx 1$  eV are seen in the  $K\beta$  and  $K\alpha$  spectra of  $H_2S$  and  $\approx 2$  eV for the  $K\beta$

and  $K\alpha$  ( $L_I$ ,  $L_{II}$ ,  $L_{III}$ ) x-ray emission spectra of  $\text{CF}_3\text{Cl}$ . These calculations also show negligible effects in the emission intensities of all molecules studied ( $< 1\%$ ). This means that screening does not influence the anisotropy of RXS.

### Parity Selection and Forbidden Transitions (Nondipole)

Due to the dipole approximation, certain selection rules arise due to the interaction of light and matter; these include angular momentum selection rules and parity selection rules. Parity selection and forbidden transitions were examined in many molecules, from diatomics to conjugated hydrocarbons [33, 34, 37-41]. In nitrogen,  $\text{N}_2$ , there are three possible orbitals that can contribute to the x-ray emission profile [34]. These correspond to the  $3\sigma_g$ , the  $1\pi_u$ , and the  $2\sigma_u$  molecular orbitals. In the resonant x-ray emission study, a core electron ( $1\sigma_u$ ) was excited to the lowest unoccupied molecular orbital, the  $1\pi_g$  orbital. The emission spectra were collected by tuning the excitation energy to the five lowest vibrational energies of the  $1\pi_g$  electronic orbital. This yields only two emission bands in each of the spectra, one from the  $1\pi_g$  and one from the  $3\sigma_g$  molecular orbital. The high-energy band is due to the participator electron, or the electron originally excited, and the other is due to a  $3\sigma_g$  electron filling the core hole; electrons from the ungerade orbitals are forbidden to fill the core hole due to the dipole selection rules and those rules are strictly upheld in  $\text{N}_2$ .

The techniques of parity selection in resonant x-ray emission spectroscopy were used to study symmetry breaking upon core-hole excitation in molecular oxygen and carbon dioxide [37-39]. To accomplish this, the symmetry selection rules (gerade and ungerade) were used to probe whether the intermediate core-excited state has broken symmetry or



not. Their main goal was to test if core-orbitals delocalize, or share the core hole, according to the irreducible representations of the point group of the molecule upon excitation.

In O<sub>2</sub> [37], a  $1\sigma_u$  core electron was promoted to the  $1\pi_g$  partially filled orbital. Due to the selection rules for parity, spin, and spatial symmetries, the final states of the molecule must be of triplet multiplicity and  $\Sigma$ ,  $\Pi$ , or  $\Delta$  symmetries. There are only three possible bands in the XES spectrum, from the  $1\pi_g$ , the  $3\sigma_g$  and the  $2\sigma_g$ . From the dipole selection rules, the  $2\sigma_g \rightarrow 1\sigma_u$  transition is forbidden; the  $2\sigma_g$  orbital is composed of O 2s character and the angular momentum does not change by one ( $\Delta \ell = 0$ ) in the  $2\sigma_g \rightarrow 1\sigma_u$  transition. The only peaks present in the emission spectrum arise from the two allowed, valence orbitals and the parity selection rule is not broken.

In the second set of measurements, two separate excitation energies were used, one at 539.2 eV (which is composed mainly of the  $3\sigma_u$  unoccupied orbital or the  $\sigma^*$  orbital) and at 541.1 eV (which consists of a vast number of Rydberg lines). The emission spectra from these two energies are similar; both consisting of one main emission line, the  $1\pi_u \rightarrow 1\sigma_g$ . At these two energies, the parity selection rule is upheld for molecular oxygen excited below threshold and the inversion symmetry of the core-excited states is also retained. This is because the internuclear separation is small compared to the wavelength of light and that the appearance of dipole forbidden emission peaks did not depend on core-hole localization, but on the internuclear separation [40].

The appearance of a carbon atom in between two oxygen atoms greatly changes the O  $K\beta$  emission spectrum by introducing an antisymmetric stretch mode [38, 39]. Core excitation occurs from either the  $1\sigma_g$  or the  $1\sigma_u$  O 1s orbital to the  $2\pi_u$  lowest unoccupied

molecular orbital. There are four possible valence emission bands, originating from the  $1\pi_g$ ,  $1\pi_u$ ,  $3\sigma_u$  and  $4\sigma_g$  orbitals. The emission spectra of  $\text{CO}_2$  show three bands, one due to the participator electron and two due to spectator electrons; the emission spectra of molecular oxygen only yielded two bands, a participator and a spectator band. If the parity selection rules held, only gerade final states would be seen, but the  $1\pi_g^{-1}2\pi_u^1$  has significant intensity in the O *K* emission spectra. Calculations show that vibronic coupling, due to the antisymmetric vibrational mode, is responsible for the breaking of the parity selection rules as seen above.

Theoretical calculations for  $\text{CO}_2$  show that the symmetry breaking is due to pseudo Jahn-Teller-like vibronic coupling<sup>2</sup> between near degenerate core excited states [38]. Vibronic interactions between the  $1\sigma_g^{-1}2\pi_u^1$  and the  $1\sigma_u^{-1}2\pi_u^1$  intermediate states allow a transition otherwise forbidden to occur in  $\text{CO}_2$ . The degree of symmetry breaking depends on the vibrational frequency and the duration of the resonant x-ray scattering process, or the correlation time between absorption and emission. If the duration time is much shorter than the vibrational time period, the molecule has no time to execute the antisymmetric vibration that introduces the forbidden parity, and there is no vibronic coupling. Tuning away from resonance effectively shortens the duration of the resonant x-ray scattering process, and one is probing transitions with shorter lifetimes and vibronic coupling becomes less and less effective. As the absorption energy is tuned farther and farther away from resonance, the forbidden band becomes smaller, and the spectrum becomes symmetry purified.

---

<sup>2</sup> In Jahn-Teller vibronic coupling, the total wavefunction is not a product of the electronic and the vibronic wavefunctions. The electronic character changes as a function of molecular geometry.

Scattering theory and a few-level model system were used to explain the symmetry purification. The theory shows that the dynamical vibronic coupling effectively vanishes in the limit of large detuning, or at higher energies, and that in this limit, the transitions between the initial ground state and the final states can be regarded as sudden, or the molecule does not have time to vibrate [39].

Strong nondipole features were also observed in Cl<sub>2</sub> at the chlorine *K*-edge [40]. In polyatomic molecules, vibrational coupling can lift the degeneracy of equivalent core-excited electronic states. In diatomic molecules, however, vibronic core-excited states remain degenerate and nondipole (parity forbidden) transitions can be observed. The pre-edge absorption feature of Cl<sub>2</sub> taken near the *K*-edge is comprised of two degenerate transitions: a dipole allowed transition  $1\sigma_g \rightarrow 5\sigma_u$ , and a dipole forbidden  $1\sigma_u \rightarrow 5\sigma_u$  transition. This degeneracy was discovered upon examination of the x-ray emission spectra where two emission lines were present; one corresponding to the dipole allowed  $2\pi_u \rightarrow 1\sigma_g$  transition and a dipole forbidden  $2\pi_g \rightarrow 1\sigma_u$  transition. The dipole approximation is normally applied in x-ray processes because the incident wavelength is much larger than the radius of the core orbital as was seen in O<sub>2</sub>. This is not valid in molecular chlorine, however, because the internuclear separation is not negligible relative to the wavelength when considering the delocalized  $1\sigma_g$  and  $1\sigma_u$  orbitals. Phase variation of the incident radiation over the entire molecule must be considered, or the dipole approximation is not valid in this case. Theoretical calculations show that there is an equilibrium bond length dependence in the normalization factor for the transition;

$$\left( \frac{1}{2} \pm \frac{3}{2} \frac{j_1(k_a R_e)}{k_a R_e} \right) \times 4 \left| \langle 1s | \hat{\mu}_z | 5\sigma_u \rangle \right|^2, \quad (37)$$

where  $j_1$  is a spherical Bessel function<sup>3</sup> dependent on the product of the radiation wave vector ( $k_a$ ) and the equilibrium molecular bond distance ( $R_e$ ),  $1s$  is the atomic-hydrogen like  $1\sigma_g$  or  $1\sigma_u$  orbitals,  $\hat{\mu}_z$  is the dipole-moment operator along the molecular axis, and  $5\sigma_u$  is a linear combination of atomic orbitals. Calculations show that as the internuclear separation increases, as in  $\text{CO}_2$  and in  $\text{Cl}_2$ , the nondipole transition becomes more intense until it has the same relative intensity as the dipole transition.

A final case of symmetry breaking leading to forbidden x-ray transitions is observed in acetylene, ethylene, and ethane [41]. In these molecules, the degree of symmetry breaking is sensitive to the change in size of the  $1s$  orbital. For these molecules, it is predicted that the longer bond length ( $\text{C}_2\text{H}_6$ , or ethane  $R_e = 1.536$ ) will have the most intense forbidden transitions followed by  $\text{C}_2\text{H}_4$  (ethylene,  $R_e = 1.339$ ) and  $\text{C}_2\text{H}_2$  (acetylene,  $R_e = 1.208$ ) will have the smallest intensity in the forbidden transitions. In  $\text{C}_2\text{H}_2$ , the measured intensities of the dipole forbidden transitions over the main resonance, and all subthreshold resonances, are very small. In  $\text{C}_2\text{H}_4$ , there are significant screening effects (2.9 eV) as well as parity forbidden transitions. The forbidden transition is present in all subthreshold resonances, but with varying intensity due to parity mixing of overlapping resonances. In  $\text{C}_2\text{H}_6$ , there are large parity forbidden transitions observed on all resonances; the only suppression of these transitions occurs at large detunings from the main resonance, due to the shortened timescale. In acetylene (triple bond), the symmetry is preserved and the forbidden transitions only contribute a small amount. The double bonded ethylene has slight symmetry breaking while the

---

<sup>3</sup>  $j_1(kR) = \frac{\sin kR}{(kR)^2} - \frac{\cos kR}{kR}$ ; a class of Bessel function (a solution to a specific differential equation) when spherical symmetry is present.

single, longest bonded ethane, exhibits the largest degree of symmetry breaking; this illustrates that symmetry breaking is not always complete for core excitation in polyatomic symmetric molecules and that it is sensitive to bond length.

### Molecular Field Effects

The core hole molecular field (MF) splitting effect is seen in cases where the core orbital has an atomic degeneracy, i.e. when the orbital angular momentum of the core orbital is greater than zero. The MF then couples with the spin-orbit (SO) interaction and can have significant effects on SO ratios and energy distributions. Such MF effects have been observed in OCS, SO<sub>2</sub>, PF<sub>3</sub> [42], SF<sub>4</sub> [43], H<sub>2</sub>S [44] and HCl [45, 46]. Calculation on the ground, the 2*s*, and the 2*p* hole states of OCS, SO<sub>2</sub> and PF<sub>3</sub>, where MF effects are included in the interaction Hamiltonian, show that changes in the equilibrium bond length and bond angles (changes in symmetry) have considerable effects on the photoelectron spectrum of these molecules [42]. The P-F bond in PF<sub>3</sub>, the S-O bond in SO<sub>2</sub>, and the C-O bond in OCS are shortened when a core-hole is introduced while the H-Cl bond in HCl [45] and the O-S bond in OCS are elongated upon ionization. In OCS and HCl [42,45], the Cl and the S atoms are electronegative and the core-hole reduces the negativity of these atoms and weakens the bond. In SO<sub>2</sub> and PF<sub>3</sub>, the largest spectral effects occur when the bond angles change upon excitation (increasing by 1.7 degrees in both molecules), which stabilizes the core-hole (more MF coupling to the SO ratio) [42]. This shortening of bond length and increase in bond angle results in an increase in the ionization energy of these electrons when the 2*pσ* types of orbitals are stabilized through

$\sigma$ -bond interactions with valence orbitals. In contrast,  $2p\pi$  types of orbitals have weak interactions and result in a decrease in ionization energy (and a smaller MF effect).

Similar experimental and theoretical studies have been carried out on HCl [46]. In HCl, the H-Cl bond is elongated upon core-excitation, just as predicted by [42]. Also, experimentally and theoretically, an 85 meV energy shift in the SO split is seen in HCl and is attributed to molecular field effects. Finally, differences from the 2:1 statistical SO ratio (branching ratio) are seen close to the ionization potential of the molecule while 2:1 ratios are achieved at high photon energies.

### Assigning XAS Using XES

In some cases, the x-ray emission spectra are well known while the x-ray absorption features may be obscure due to lifetime broadening or are otherwise unknown. The symmetry determination of XAS features can be achieved by examining the polarization (angular dependence) of selectively excited XES [47, 48]. The first case involves the determination of molecular orbital symmetry in  $\text{H}_2\text{S}$  [47]. The molecule  $\text{H}_2\text{S}$  belongs to the symmetry group  $\text{C}_{2v}$  and has a subthreshold absorption resonance, which is dominated by excitations to the unresolved  $3b_2$  and  $6a_1$  orbitals. The polarization of the  $K$ -V emission varies as the incident photon energy is scanned across the absorption resonance; this is attributed to contributions from excitation to the two absorption resonances that have different symmetries. Additionally, polarization studies in  $\text{H}_2\text{S}$  above the IP permitted the study of the formation of an emission satellite<sup>4</sup> and its origin. There are three peaks found in the x-ray emission spectrum of  $\text{H}_2\text{S}$ ,  $2b_1 \rightarrow 1a_1$  (A),  $5a_1 \rightarrow$

---

<sup>4</sup> a multielectron process where the incident and an outer core or a valence electron are both excited.

$1a_1$  (B), and  $2b_2 \rightarrow 1a_1$  (C). The MO's are derived from S  $3p$  and H  $1s$  atomic orbitals,  $5a_1$  and  $2b_2$  are combinations of S  $3p_z$  and  $3p_y$  AO's with H (1)  $1s$  and H (2)  $1s$  orbitals while  $2b_1$  is a nonbonding orbital ( $3p_x$ ). Peak C is suppressed, while A and B are enhanced when the spectrometer is aligned to detect perpendicular polarization; meaning the peaks have strong polarizations of opposite sign. Classically, the polarization,  $P$ , for an electric dipole absorber and reemitter is given by  $P = (3 \cos^2 \gamma - 1) / (2 \cos^2 \gamma + 1)$  where  $\gamma$  is the average angle between the emission and absorption oscillators, and  $P$  reaches limiting values of  $1/2$  and  $-1/3$  for angles  $0^\circ$  and  $90^\circ$ , respectively. Using the  $C_{2v}$  group character table, the  $1a_1 \rightarrow 3b_2$  and  $1a_1 \rightarrow 6a_1$  absorption dipole moments point along the y and z-axes, respectively. The emission dipole moments for peaks A ( $2b_1 \rightarrow 1a_1$ ), B ( $5a_1 \rightarrow 1a_1$ ) and C ( $2b_2 \rightarrow 1a_1$ ) point along the x, z, and y-axes, respectively. The classical model then predicts the polarizations of peaks A, B, and C to be  $P_A = -1/3$ ,  $P_B = 1/2$ , and  $P_C = 1/2$  for the  $1a_1 \rightarrow 3b_2$  transition, while  $P_A = -1/3$ ,  $P_B = 1/2$ , and  $P_C = -1/3$  for the  $1a_1 \rightarrow 6a_1$  excitation. At excitation energies at or below the peak of the absorption resonance, data is consistent with the  $1a_1 \rightarrow 3b_2$  assignment. As the excitation energy is increased to the high-energy side of the absorption maximum, the emission peak polarizations shift towards the polarization values that are consistent with the addition of the  $1a_1 \rightarrow 6a_1$  excitation;  $P_A$  remains large and negative,  $P_B$  becomes less negative and  $P_C$  becomes less positive. This suggests that the  $1a_1 \rightarrow 3b_2$  resonance is 0.5 eV below the  $1a_1 \rightarrow 6a_1$  resonance.

When the excitation energy is 5.7 eV above the S  $1s$  threshold, a shoulder develops on the high-energy side of peak A. As the photon energy is increased, the intensity of the shoulder increases until it reaches an asymptotic value around 2550 eV. This suggests

that initially the satellite can be attributed to *K*-hole formation and electron excitation to an unoccupied valence orbital. At higher energies, double ionization also may contribute to the intensity of the shoulder.

The O *K*-V x-ray emission spectra in parallel (0°) and perpendicular (90°) angular distributions of CO<sub>2</sub> were measured to aid in assigning the x-ray absorption spectrum at the O *K*-edge [48]. There are three subthreshold features in the O *K*-absorption spectrum; a strong-broad peak, a weaker-sharp peak, and a broad structure leading to the IP. To determine the symmetry and parity of unoccupied orbitals, the x-ray emission intensity ratio between the  $1\pi_g$  and the  $(3\sigma_u/1\pi_u)$  emission peaks was compared. These intensity ratios were compared to a statistical, isotropic angular distribution. If the intensity ratio of the emission peaks is well above this value, the excitation is to gerade unoccupied orbital, and well below for excitations to an ungerade orbital. From this, the strong-broad peak is of ungerade parity and the other two are of gerade parity. On the strong-broad resonance, there is no difference between parallel and perpendicular intensity ratios; this means that this resonance is comprised of the  $2\pi_u$  MO. On the other two resonances, the intensity ratios are smaller in the perpendicular direction; and the difference comes from the low-energy side of the emission peak of ungerade parity (or the  $3\sigma_u$  emission). From this, the absorption features in question are mainly due to unoccupied levels of  $\sigma$  symmetry. Static exchange and multiconfiguration self-consistent field calculations of the absorption spectrum confirm the assignments.



## Ultrafast XES

Recently, resonant x-ray Raman scattering was also shown to be a powerful tool in studying ultrafast, sub-femtosecond nuclear dynamics. Femtosecond lasers are used in the vacuum ultraviolet energy region to probe the evolution of an electronic system on a short time scale using valence electron excitation. Unfortunately in the x-ray energy range above 1 keV, a direct approach using ultrafast (short-pulsed) light sources is currently not available; therefore, another experimental approach must be used. Ultrafast x-ray spectroscopy occurs when molecular dissociation is faster than the core-hole lifetime. Core-hole lifetimes in first and second row elements are several femtoseconds long,  $\sim 10$  fs in OCS and  $\sim 1$  fs in HCl, and ultrafast dynamics have been observed in hydrogen halides [15, 49-51] diatomic molecules such as oxygen [52] and nitrogen [53], and polyatomic molecules such as carbonyl sulfide [53] and phosphine [54]. Ultrafast RXS relies on the analysis of spectral features sensitive to short time evolution of the molecular system. If molecular dissociation is fast when compared to electronic relaxation of the molecule, emission from the fragment is observed in conjunction with the molecular emission, allowing the study of sub-femtosecond dynamics using RXS techniques (for Cl the core-hole lifetime is 0.9 fs (FWHM of 0.64 eV) and the FWHM of the main, dissociative, resonance is 0.8 eV) [15].

In HCl [15], the RXS  $K$ - $L$  and the  $K$ - $V$  profiles broaden as the incident photon energy is detuned from the main absorption resonance; see Figure 9. Dynamical broadening is quenched on top of the main absorption resonance because the width of the emission line approaches the final state lifetime broadening ( $\Gamma$  in equation 24). Also, the duration time of RXS is reduced by frequency detuning ( $\Omega$ ) due to the suppression of large-time

contributions to the scatter. It was shown, theoretically and experimentally, that detuning from the main absorption resonance results in a non-linear dispersion of the *K-L* lines because the widths of the FC factors ( $\Delta$ ) and the Lorentzian term ( $\Gamma$ ) are comparable in hard x-rays. The decay transition between inner shells has parallel potential surfaces, which is a completely general process (in contrast with resonant Auger scattering where the potentials of core-excited and final states are parallel by coincidence) [55].

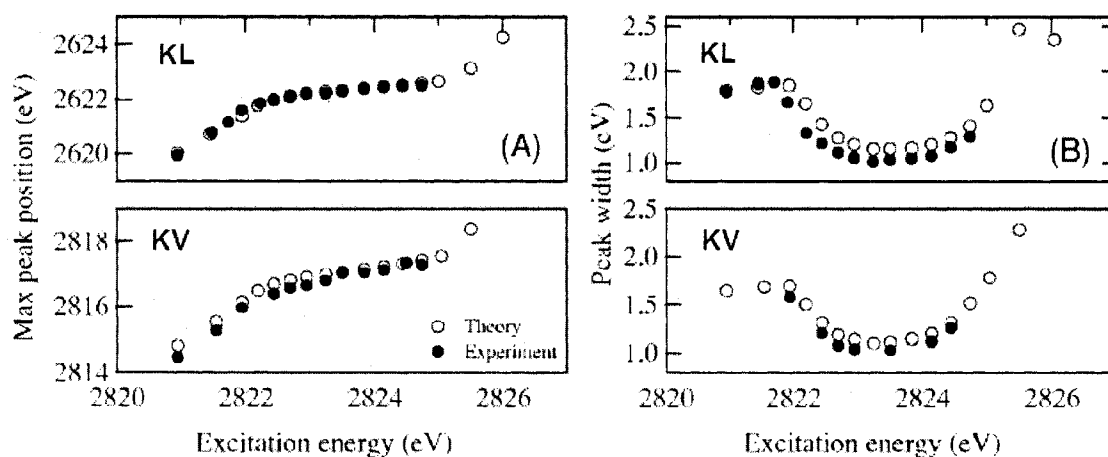


Figure 9. (A) Measured, solid dots, and calculated, empty dots, x-ray dispersion for the *K-L* and *K-V* x-ray emission. (B) Measured (solid) and calculated (empty) spectral widths for the *K-L* and *K-V* x-ray emission reported by Simon et al [15].

The elastic band in *K-V* emission spectrum is most sensitive to nuclear dynamics; small changes in bond length can have large effects on the shape and intensity of the elastic peak; see Figure 10. As seen in Figure 10, the elastic peak on the top of the main absorption resonance, where the duration time is long, is asymmetric; because this resonance is dissociative, this peak contains contributions from the molecule at the

equilibrium bond length and from the molecule with an increased bond length<sup>5</sup>. Farther from the top of the resonance, the duration time becomes short and the wave packet does not have time to spread on the core-excited potential surfaces and the elastic peak becomes more symmetric. At  $\Omega = -1.56$  eV the peak is totally symmetric and only the molecule at the equilibrium bond length contributes to the emission because the emission occurs before the molecule can begin to dissociate.

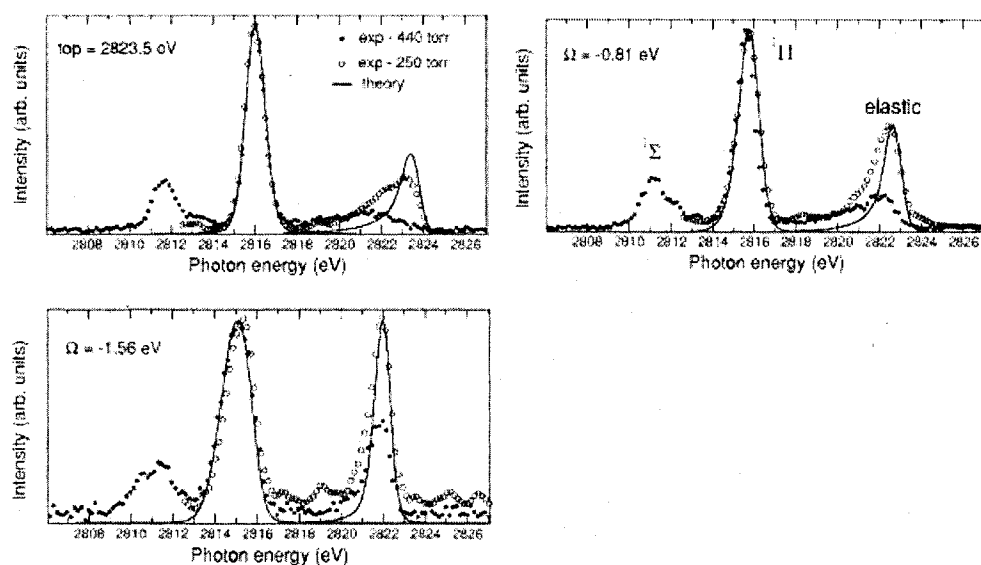


Figure 10. X-ray emission spectra at three detunings,  $\Omega = 0, -0.81$  and  $-1.56$  eV at 250 Torr (empty) and 440 Torr (solid) measured by Simon et al [15].

<sup>5</sup> an increased bond length can be complete dissociation or small changes in the bond length

## CHAPTER 4

### EXPERIMENTAL SET-UP

Investigations of atomic or molecular core-level x-ray fluorescence require an intense and high-resolution source of polarized x-rays. It is also desirable for the secondary (emission) spectrometer to be polarization sensitive and of moderately high resolution. The first requirement is met by using synchrotron radiation from a third-generation light source, namely the Advanced Light Source where the x-rays are inherently linearly polarized. The secondary spectrometer requirement is met by using a Si (111) crystal, which provides good energy resolution and strong rejection of light polarized out of the plane of the crystal surface, in this case rejecting over 99% of light polarized in the plane of incidence when the crystal is near  $45^\circ$  (2800 eV).

#### Advanced Light Source (ALS)

Experiments were conducted at beamline 9.3.1 at the ALS, Lawrence Berkeley Laboratory, Berkeley, CA. The ALS provides both quasistatic and pulsed operation. The x-ray emission spectrometer is designed to run during the quasistatic, or multibunch, mode. In multibunch mode, the electrons are at energies of 1.9 GeV with a maximum current of 400 mA. In this mode, 276 electron bunches circulate in the storage ring with a uniform spacing of about 2 ns except for one larger gap. This provides the intense photon flux required to make x-ray emission measurements. Beamline 9.3.1 utilizes a double Si (111) monochromator at an energy range of 2.2 keV to 6.0 keV which provides

intense ( $10^{11}$  photons/sec), monochromatic ( $\pm 0.3$  eV at the Cl  $K$ -edge), and over 99% linearly polarized photons along the plane of the storage ring orbit; see Figure 11 [5].

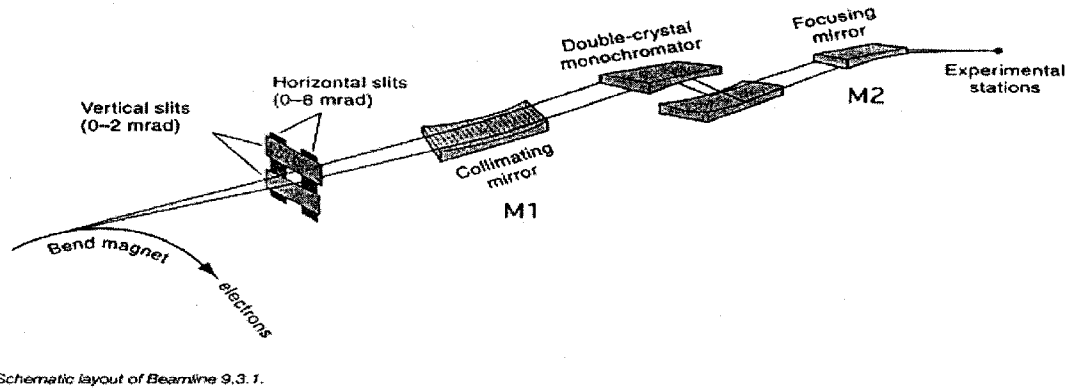


Figure 11. Schematic layout of beamline 9.3.1 at the ALS [5].

Incident photon energy is selected using Bragg diffraction, where photon wavelength is directly related to the angle of the crystal face by the following relationship:

$$n\lambda = 2d \sin \theta_{\text{Bragg}} \quad (\text{Bragg Equation})$$

where  $\theta_{\text{Bragg}}$  is the Bragg angle,  $d$  is the crystal lattice spacing, and  $\lambda$  is the photon wavelength (in Angstroms). For Si (111),  $2d$  is  $6.2712 \text{ \AA}$ .

### X-ray Emission Spectrometer

An x-ray emission spectrometer (XES) was designed and built to measure x-ray fluorescence resulting from a core-level atomic or molecular excitation [57]. Polarization sensitive core-level x-ray fluorescence requires a source of polarized x-rays, high-resolution primary and secondary x-ray monochromators and polarization sensitivity of the secondary monochromator. The first requirement is met by using synchrotron

radiation from a third-generation light source, which provides inherently linearly polarized x-rays. The spectrometer utilized in the XES is a curved Si (111) crystal, which provides strong rejection of polarization out of the plane of the crystal face. The spectrometer can be rotated to detect fluorescence emitted parallel or perpendicular to the polarization/propagation direction of the incident x-rays.

The secondary spectrometer is of Johann geometry [58]; the crystal face and the detector are both situated on a Rowland circle of variable radius with the crystal-to-detector distance fixed at 0.6 m. The sample cell is situated inside the circle to reduce sensitivity to alignment of the primary photon beam with respect to the secondary spectrometer and to prevent point-to-point focusing from the sample to the detector. X-rays travel vertically upward from the gas cell and are focused onto the detector, a two-dimensional microchannel plate resistive anode encoder (MCP-RAE); which can collect an entire spectrum (20 eV wide with 0.5 eV resolution at the Cl *K*-edge) in unison.

The x-ray emission spectrometer described here is a new apparatus that currently has an energy range of 2.4-3.6 keV with three main components, a gas cell, crystal bender, and detector. A schematic of the experimental setup is shown in Figure 12 and an Autocad® drawing is shown in Appendix II. The XES was designed, in its present state, for ALS bending-magnet beamline 9.3.1, which has a photon energy range of 2-6 keV. Light passes through the beamline monochromator and is focused into the XES, which maintains a pressure of  $10^{-7}$  Torr during data collection. Vacuum interlocks between the experiment and the beamline are provided to protect the beamline and the ALS storage ring should gas containment fail in the sample cell. The entire XES can be rotated about the axis of the beamline by 360° while maintaining vacuum, permitting measurements of

angular distribution of emitted x-rays. Two tilt sensors automatically monitor the angle of spectrometer rotation (0-90°). Incoming light passes through a four-jaw apparatus, which trims off any stray light from the beamline monochromator.

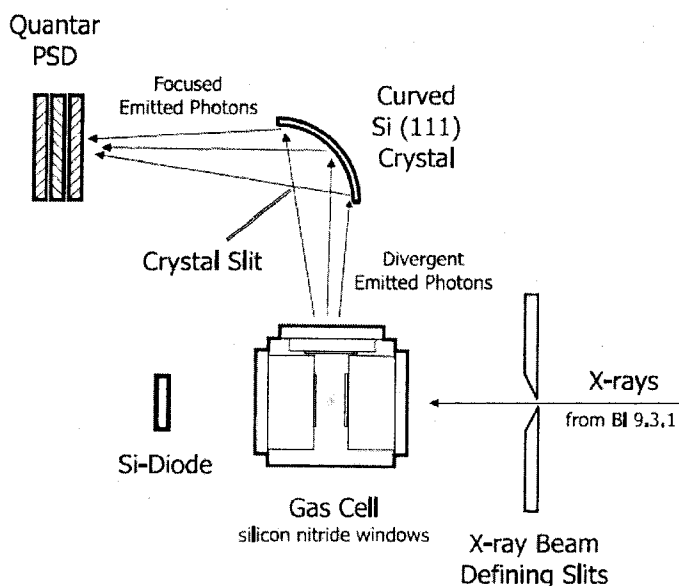


Figure 12. Flow diagram of the x-ray emission spectrometer.

Vertically upward, in the nominal position, from the gas cell (0.4 m) is the crystal tank, which houses the spectrometer. The crystal face of the spectrometer is designed to be in line with the photon exit window of the gas cell. The spectrometer can rotate from 0-180° to detect parallel-polarized light (0°) and perpendicular polarized light (90°) with respect to the polarization of the incoming photons. A rotational position transducer is attached to the arm to detect the angle of the spectrometer and a second detects the angle of the crystal face. Attached to the crystal tank is a 0.6 m long arm that houses the MCP-RAE detector housing. Movement of the detector is restricted to a curved path along the Rowland circle where movement of the arm changes the Bragg angle of the spectrometer

and as a result the energy range on the detector. The detector's position is recorded using a cable-extension position transducer, which measures the relative position of the detector.

### *Vacuum Isolation*

Vacuum isolation is critical in the XES to protect the beamline and the spectrometer should gas containment fail in the sample chamber. Pressure is monitored at three different locations, in the gas cell (which has operating pressures around 450 Torr), in the sample chamber (maintained at  $10^{-7}$  Torr) and at the detector ( $< 10^{-6}$  Torr). Between the endstation and the beamline and also between the main chamber and the spectrometer there are isolation gate valves, used to isolate the beamline or the spectrometer from the main chamber. This protects the detector and the beamline if a leak should develop in the gas cell. All valve controls, pressure sensing devices and vacuum pumps are controlled and monitored utilizing two independent vacuum interlock boxes, Figure 13. When a pressure change is sensed, the interlock boxes close the valve between the chamber and beamline (spectrometer), shut off the ionization gauge, and also shut down the turbo vacuum pump. This minimizes the effects of a containment failure on the beamline and the detector.



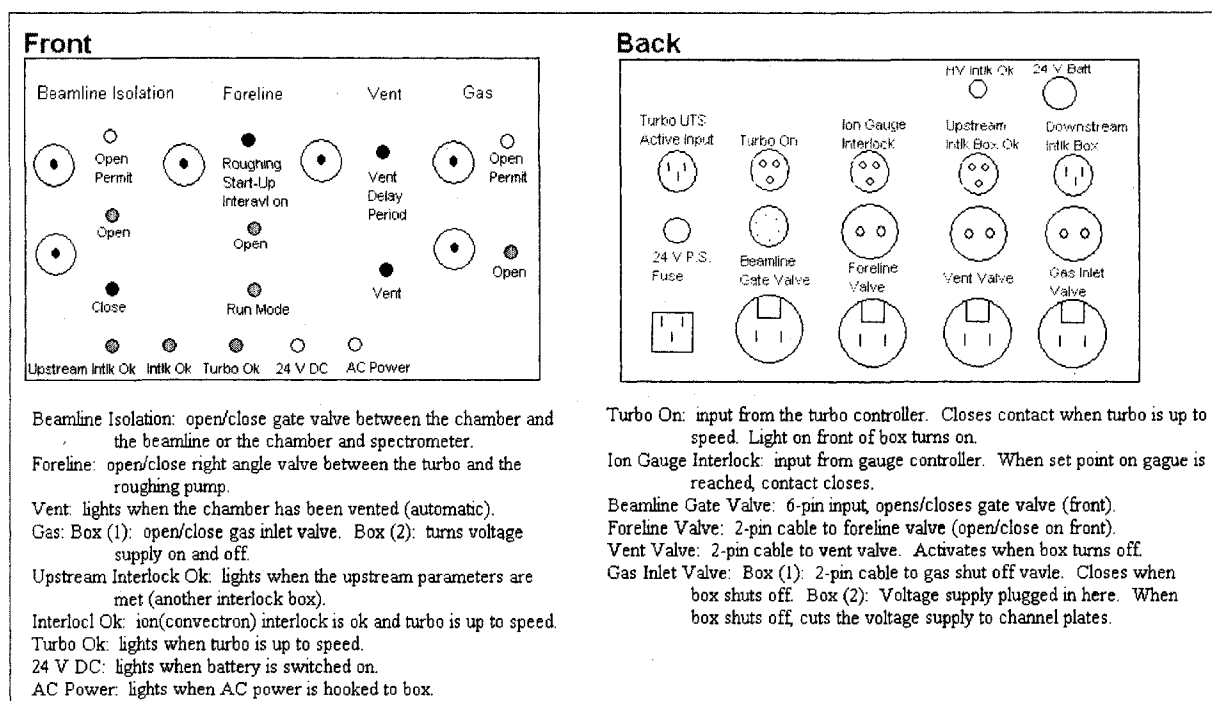


Figure 13. Description of the interlock box and its various functions.

### Gas Cell

A static gas cell allows x-rays to enter and exit a high-pressure sample of gas while maintaining the high vacuum of the chamber and the beamline. The skeleton of the gas cell is a commercially available mini-metal gasket sealed cube, to which incident-x-ray entrance and exit windows, a viewing window for x-ray-emission, and stainless-steel plumbing for gas handling have been added. The entrance and exit windows are 3 mm x 3 mm x 200 nm thick silicon nitride ( $\text{Si}_3\text{N}_4$ ) mounted on a 7.5 mm square frame. Silicon-nitride windows are used because they are easy to obtain, reasonably priced, relatively strong (able to support up to an atmosphere of pressure), and have over 90% x-ray transmission in the energy range of primary interest. The entrance and exit windows are mounted on cylindrical tubes extending 9.5 mm into the cube to allow the emission

window to observe the entire 2.5 mm photon-beam path through the gas sample; Figure 14. Relative absorption measurements can be made using a Si diode at the rear of the chamber to measure the x-ray flux transmitted through the gas cell.

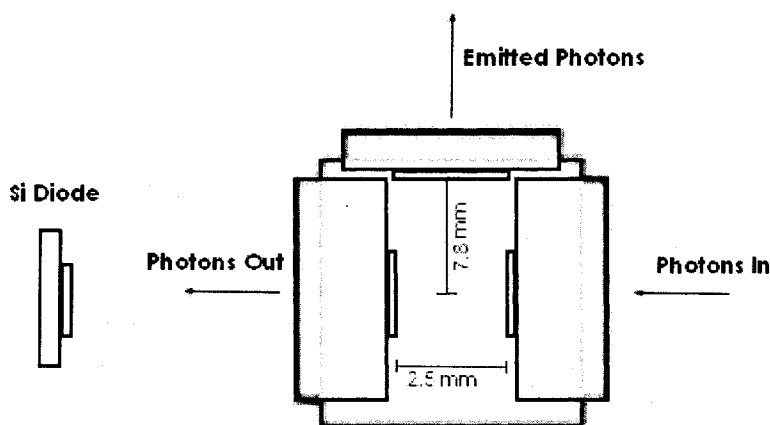


Figure 14. Schematic representation of the incident photon-gas sample interaction region. Photons enter and exit the cell along the beamline vector while emitted photons are detected perpendicular to the beamline.

X-rays emitted by the gas sample and that pass through the viewing window travel vertically upward, in the nominal spectrometer position, to the spectrometer crystal. The viewing window, also silicon nitride and of the same size as the entrance and exit windows, is mounted on a cylindrical tube extending 7.0 mm into the gas cell. The distance the photons travel to exit the sample cell through the viewing window is 7.8 mm, Figure 14. Gas enters the cell through a flange mounted opposite the viewing window, where, in current configuration, it remains static during measurements. The sample cell can be pumped or evacuated without disrupting the vacuum inside the chamber. To focus

x-rays from the beamline into the gas cell, a YAP ( $\text{YAlO}_3$ ) crystal and a  $90^\circ$  prism are mounted on the gas cell. The prism rotates the view of the beamspot on the YAP crystal, making it possible to view the size and shape of the incident-x-ray beam through a vacuum window on the chamber; mechanical drawings of all components are shown elsewhere [20].

### *Crystal Bender*

The spectrometer consists of two components: a crystal bender and a thin rectangular Si (111) crystal. The crystal bender was designed to bend a thin rectangular crystal into a near perfect circular arc, providing focusing and energy tuning of the emitted x-rays, see Figure 15. The bending device, allowing the crystal's radius of curvature to match the diameter of the Rowland circle, produces radii as small as 0.6 m. This arrangement provides maximum photon focusing in this geometry. In the nominal orientation, the vertical axis of the crystal bender is aligned with the vertical axis of the main chamber, and the entire apparatus is built to be insensitive to gravity for different orientations. The crystal-bending device contains two bender arms, a rotation link, two transfer bars, rotary link, pivot flexures for bending, a micrometer controlled linear motion feedthrough, two adjustment screws, a re-zeroing spring, and a Si (111) crystal. Bending is initiated when the linear motion feedthrough is moved, thus rotating the rotation link, which causes the transfer bars to push the bender arms apart. This action turns the flexures at both ends of the crystal, producing equal bending moments that deflect the crystal into a circular arc. Flat areas at the ends of the crystal due to mechanically holding the crystal on the edges can be masked with a crystal slit.

To establish a 'zero' for the crystal bender, the crystal is initially set flat and mechanically checked along its length and width for trueness with a micrometer; see Figure 16. The crystal can be fine adjusted along its length using the adjustment screws and metal shims. The zeroing spring is present to force the crystal back into the flat position after the crystal has been bent. After zeroing, the bender returns to the flat position when the input bar is completely relaxed. Along with establishing a zero, the center of the crystal was also calculated as a function of bend; the center of the crystal does not change with the deflection of the crystal.

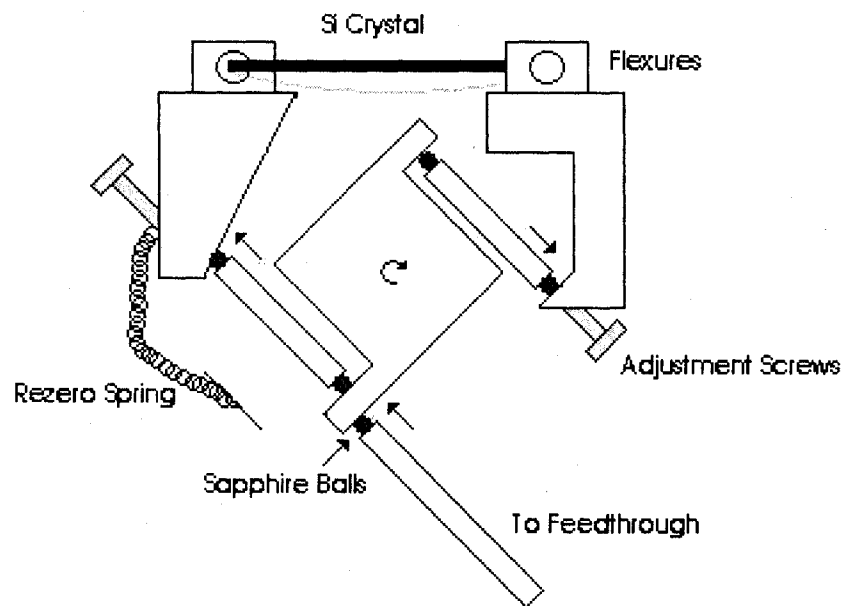


Figure 15. Schematic representation of the crystal-bending device.

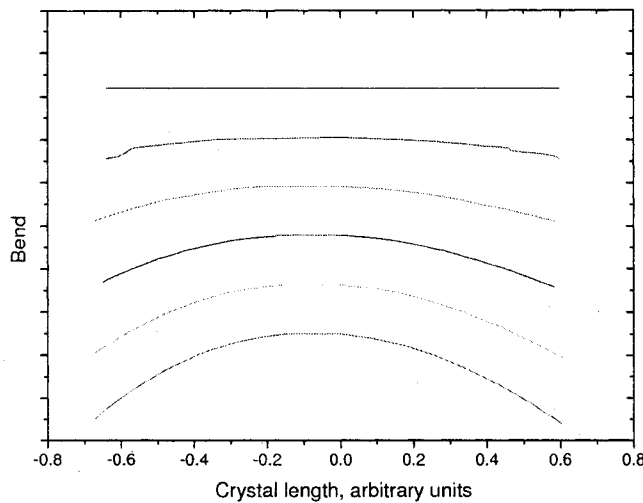


Figure 16. Micrometer measurement of the crystal bend along the length of the crystal. The crystal was incrementally bent and the crystal length versus the displacement from the flat position was recorded.

Si (111) crystals are currently used because they have an effective energy range of 2.0 keV to 22 keV. They are also rugged and stable with a high degree of perfection, so they can maintain a curved position for long periods of time without breaking. The size of crystal supported in the bender is 20 mm x 40 mm x 0.2 mm thick.

### *Detector*

The detector is a commercially available electron-optical device, Quantar Technology Inc®, model 3300, and is operated in clean vacuum with pressures lower than  $10^{-6}$  Torr. It has three wafer-type microchannel-plate electron multipliers; the first of which has a CsI coating for maximum photon detection. A resistive anode position encoder with integrated voltage bias and signal decoupling circuits backs the MCP stack. The encoder converts an incoming photon to four charge signals proportional to the spatial position of

incidence with a 100-micron resolution. Incident photons strike the front surface of the first MCP and the electron packet diffuses in the uniform resistive sheet surface of the anode toward collection electrodes located at the four corners (A, B, C, and D). The relative charge reaching each of the four corner contacts is a linear function of the position along X and Y orthogonal axes of the anode. Four signals and the total counts striking the detector are routed to the detector pre-amplifier. All five components are then sent to the position analyzer where the four signals are converted to X and Y coordinates. After the position analyzer, a Quantar Technology® model 2401B, the signal passes through a National Instrument® PCI-DIO-32HS card, and finally it is displayed, as a 2-D 1024 x 1024 array, and saved using customized Labview® software. The images obtained are further processed in IGOR®, a data analyzing, image processing, and programming software tool from WaveMetrics, to obtain the emission spectrum as a function of energy. As seen in Figure 17, the raw image from the detector is slightly curved due to the curvature of the crystal. A custom IGOR® fitting procedure accounts for the curvature to obtain maximum energy resolution. A histogram is then created as a function of channel number (0-1024) along the X-axis of the detector.

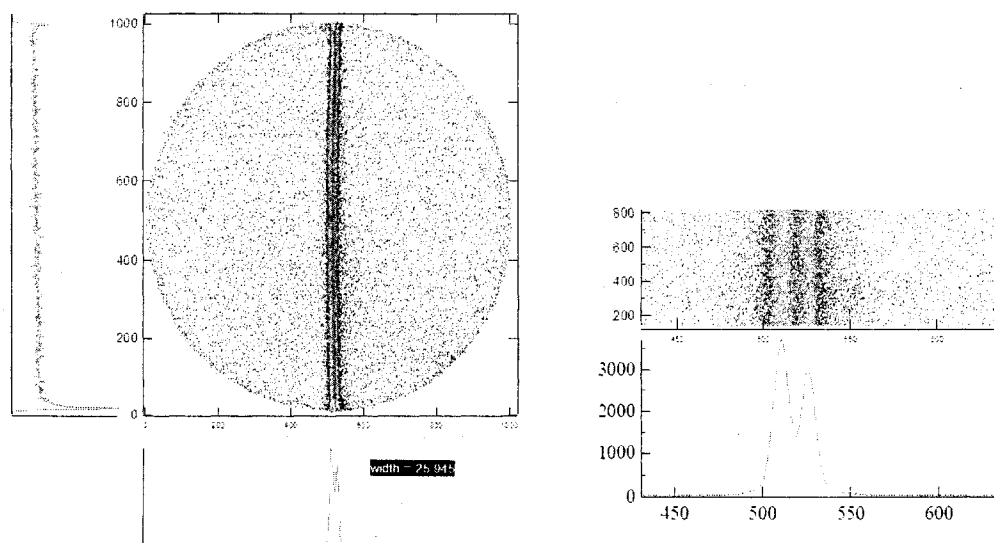


Figure 17. Raw detector image (top-left) and histogram (bottom-left) before the image was corrected for the crystal curvature. Expanded detector image with curvature corrections (top-right) and histogram (bottom-right). The image is the Cl *K-L* emission from CF<sub>2</sub>Cl<sub>2</sub> following the  $1a_1, 1b_2 \rightarrow 13a_1, 9b_2$  excitation (2823 eV photon energy).

### Alignment and Energy Calibration

The detector has a 40 mm<sup>2</sup> active area with a spatial resolution of approximately 100 microns. However the spectral resolution is not based solely on the spatial resolution of the detector. It includes all experimental effects; namely natural line widths, broadening due to diffraction from the crystal, and errors arising from peak-fitting procedures. With this instrument, the combined (beamline and instrumental) measured resolution,  $0.52 \pm 0.05$  eV, is primarily due to diffraction broadening of the crystal, with a very minor part due to the detector spatial resolution. Experimental peak widths in the Cl *K-L* energy range vary from 7.2 channels (0.9 eV), on resonance to 11.7 channels (1.5 eV) above resonance and those in the Cl *K-V* energy range vary from 13.2 channels (1.4 eV) on

resonance to 18.8 channels (2.0 eV) above resonance. At the Cl *K*-edge, the natural line widths are much larger than the experimental resolution and determine the spectral resolution.

Rigorous alignment and testing of the components of the emission spectrometer is described elsewhere [20]. The spectrometer is aligned with the axis of the beamline using three alignment points. The first is a paddle that enters the path of the photons at the front of the XES; which contains an alignment hole in the center. Second, is the gas sample cell, which can rotate 90°, and has a YAP (yttrium aluminate) crystal and a prism for alignment and photon focusing. Third, is an alignment paddle situated in the rear of the XES.

Energy calibration of the XES is accomplished in the parallel polarization direction; parallel to the polarization/propagation direction of the incident x-rays. Incident photons of the same energy as the emission energy of interest are diffracted off of the sample gas and collected on the detector. Calibration must be done using a parallel orientation because, due to polarization effects, elastically scattered photons cannot be observed in the perpendicular geometry. At least four different incident photon energies are recorded, the range of which cover the window of the emission spectra. The energies of the scattered photons are then plotted as a function of peak position determined by the detector; see Figure 18. A linear fit through the points is used to determine the energies of any x-ray emission peaks present within the energy window. As an example, an energy-calibrated spectrum for Cl *K-L* (*Kα*) emission from CF<sub>2</sub>Cl<sub>2</sub> following the  $1a_1; 1b_2 \rightarrow 13a_1; 9b_2$  excitation at 2823 eV photon energy is shown in Figure 19.



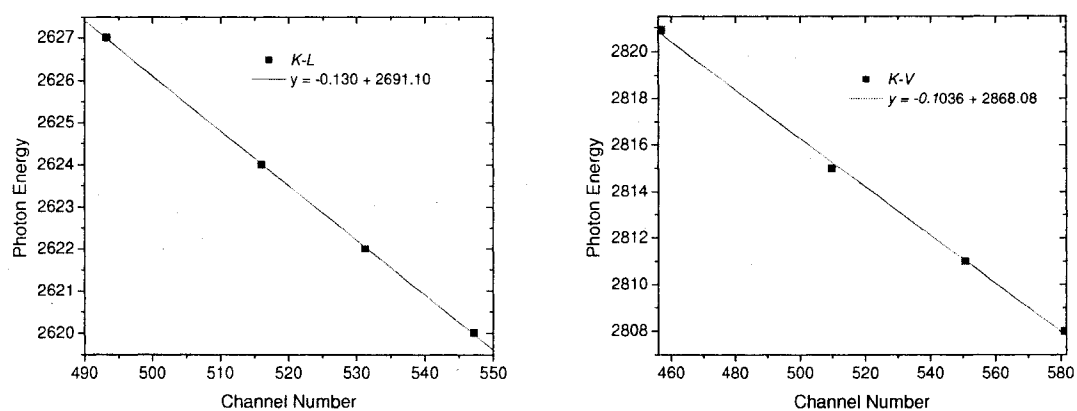


Figure 18. Energy calibration at the Cl *K* emission energy range. The plot on the left is the energy calibration in the *K-L* region and the plot on the right is the energy calibration in the *K-V* region.

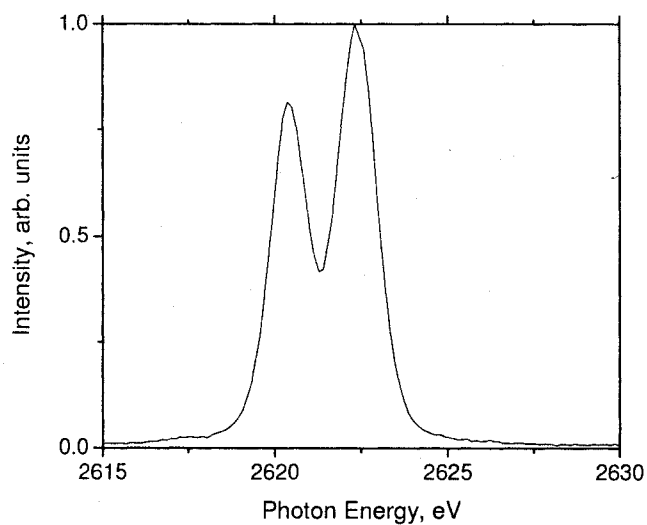


Figure 19. Cl *K-L* emission spectrum of CF<sub>2</sub>Cl<sub>2</sub> following the  $1a_1; 1b_2 \rightarrow 13a_1; 9b_2$  excitation at 2823 eV after energy calibration.

In the parallel-polarization geometry, the crystal slit can be used to increase resolution of the x-ray emission spectra at the cost of reducing both the signal and the width of the energy window. Figure 20 shows the reduction of the useable emission energy window for Cl *K-V* emission in the parallel orientation of the spectrometer. The effective resolution follows a nearly linear curve varying from approximately 0.4 eV for a slit of 0.2, to about 1 eV for a slit of 4.0. This relationship between slit position and energy resolution exists because the source volume of x-ray emission is extended along the incident beam axis, which, in the parallel geometry, coincides with the energy-dispersive axis of the spectrometer. In contrast, the resolution and energy window are affected much less in the perpendicular direction, for which the incident beam axis and the energy-dispersive axis do not coincide. For the perpendicular orientation, the only significant consequence is the loss of signal. Similar behavior was observed for Cl *K-L* emission.

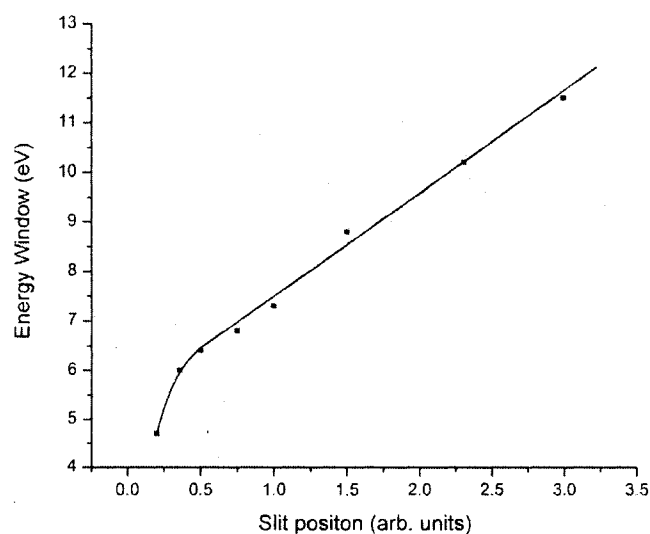


Figure 20. Variation of the x-ray energy window with crystal slit position. Data was collected in the *K-V* energy range.

## Argon Spectral Calibration

Spectral calibration of the XES was performed at the Ar *K*-edge by measuring the Ar *2p* x-ray emission. Argon was chosen because it does not have geometrical or molecular field effects and spectra in the parallel and perpendicular have shown to be the same [26]. Figure 21 shows the measured x-ray absorption from 3202 eV to 3210 eV and the emission spectra at two excitation energies; on resonance (3203.3 eV) and far above the IP (3250 eV) in both polarization directions. As Figure 21 shows, there are no polarization effects seen on resonance or above resonance, also observed by Cowan et al [26]. Because there are no polarization effects, there are no significant geometrical differences between parallel and perpendicular spectrometer orientations.

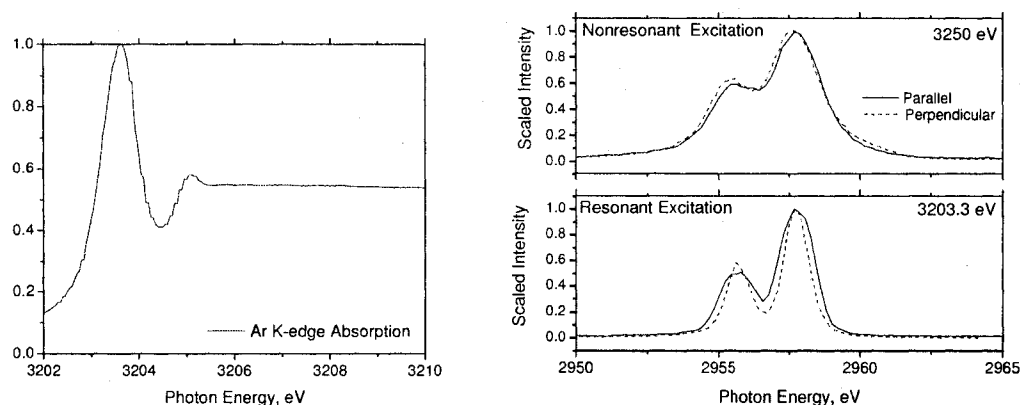


Figure 21. Argon *K*-edge absorption spectrum (left) and argon x-ray emission spectra at two incident photon energies on the main absorption resonance (3203.3 eV) and far above the IP (3250 eV) in both polarization directions.

Figure 22 shows the Ar x-ray dispersion and the x-ray peak-widths from 3202 eV to 3210 eV. The x-ray dispersion shows a linear increase with increasing photon energy

over the main resonance as seen in Xe [14] and predicted by Agren [23]. As seen in resonant x-ray scattering, there is a decrease in peak width on top of the resonance; above the IP the peak widths remain constant. The spin-orbit ratios, Figure 23, are increasing with increasing photon energy over the main resonance and decrease over the  $4p$  Rydberg but reach their characteristic 2:1 ratios on the resonance and above the IP; also seen by Cowan et al.

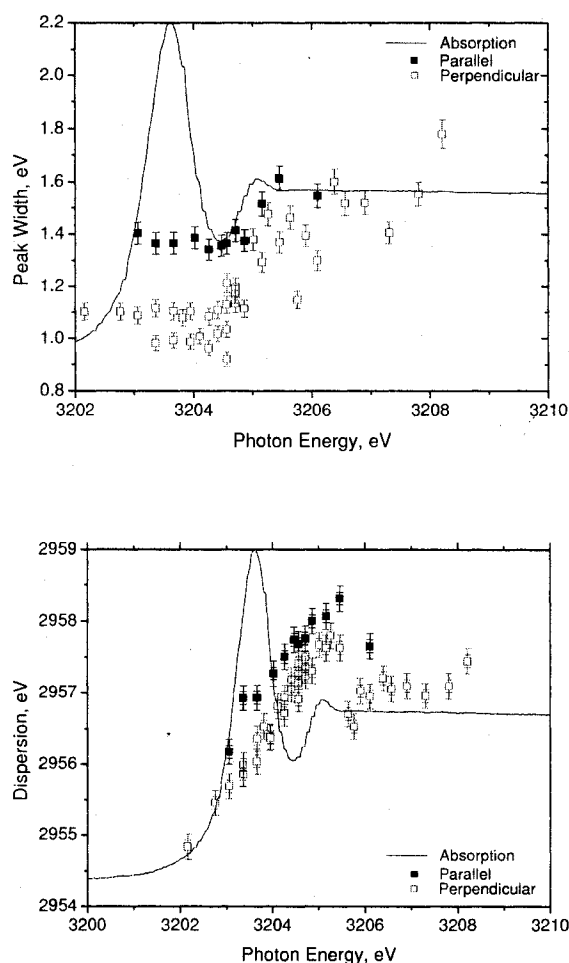


Figure 22. Measured  $K$ - $L$  x-ray peak widths (top) and x-ray dispersion (bottom) in the parallel (solid) and the perpendicular (empty) orientations.

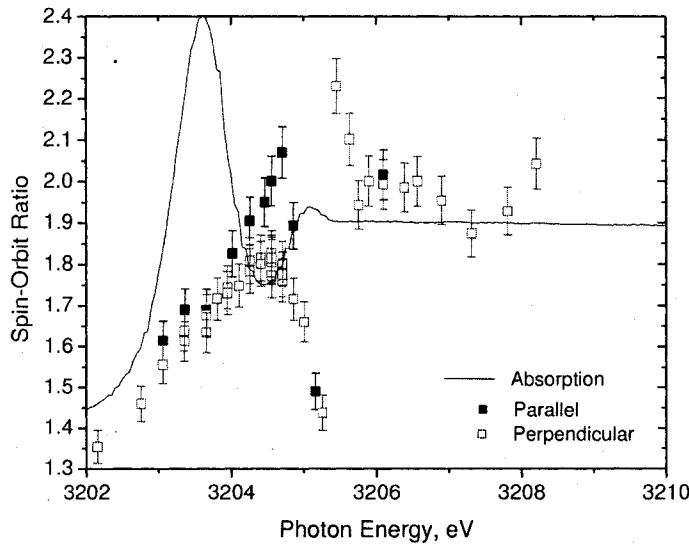


Figure 23. Measured Ar *K-L* spin-orbit ratios in the parallel and perpendicular orientations.

#### Spectrometer Equations

The x-ray emission spectrometer is sensitive to small changes in angle; to monitor the relative positions of the major components, position sensitive devices were installed. To track the position of the detector on the curved way (this movement selects the radius of the Rowland circle), a cable-extension position transducer is used. This device measures the displacement of the detector from  $90^\circ$  ( $\theta_{\text{Curved}}$ ), or the center of the curved path, and gives a voltage output. To calculate  $\theta_{\text{Curved}}$ , the Bragg angle is used:

$$\theta_{\text{Curved}} = 2 \cdot (45^\circ - \theta_{\text{Bragg}})$$

The displacement from  $90^\circ$  directly correlates to the energy region the detector can view.

To find the voltage output of the position transducer, the following equation is used:

$$V_{Out} = -0.136\theta_{Curved} + 3.4304.$$

The voltage range for the curved way is  $7.372 \geq V_{Out} \geq 0.206$ , which corresponds to a displacement of  $29.8^\circ$  to the right of center and  $24^\circ$  to the left of the center of the curved path. The position of the spectrometer tank (crystal face) and the angle of the spectrometer (parallel and perpendicular) are measured using rotational position transducers, which provide a linear output voltage with respect to the angle. The spectrometer angle can be calculated using the following equation:

$$V_{Out} = -0.0278\theta_{Spect} + 8.5883$$

and corresponds to a voltage output range of  $8.705 \geq V_{Out} \geq 3.554$ . The tank angle is not calculated directly; instead it is measured versus the photon energy, since the voltage output range is less than two volts. The equation is as follows:

$$V_{Out} = 3 \cdot 10^{-7} (h\nu)^2 - 0.0021(h\nu) + 8.7956$$

The angle of the main chamber is measured using two biaxial clinometers (tilt sensors). These two devices work together to cover the full range of rotation. Tilt one measures angles below zero up to an angle of  $42^\circ$  and tilt two covers angles above  $42^\circ$ . The tilt of the chamber can be calculated using the following set of equations:

$$\text{when } \theta_{Chamb} \leq 42^\circ; V = -1.0 \cdot 10^{-5} \theta^3 + 0.0003\theta^2 - 0.0376\theta - 0.0025$$

$$\text{when } \theta_{Chamb} \geq 42^\circ; V = 5.0 \cdot 10^{-6} \theta^3 + -0.0013\theta^2 + 0.1422\theta - 5.854$$

The voltage range for tilt one is  $-4.193 < V_{\text{tilt}} < (4.0)$ , and for tilt two,  $-4.22 < V_{\text{tilt}} < (4.0)$ .

The voltage outputs are displayed in Labview where they can be monitored.

### Gas Samples

Gas samples,  $\text{CFCl}_3$ ,  $\text{CF}_2\text{Cl}_2$ , and  $\text{CF}_3\text{Cl}$ , are obtained commercially with over 99% stated purities. They are stored in lecture bottles and plumbed directly into the gas cell through clean gas lines where the pressure is maintained at 450 Torr and room temperature during data collection. The liquid sample,  $\text{CCl}_4$ , is also obtained commercially with over 99% purity. A small amount of the liquid is transferred to a glass vial where the air is purged out. The vial is attached to the gas inlet system where the vapor is allowed to diffuse into the cell. Pressure in the cell is maintained at the vapor pressure of the liquid; vapor pressure of  $\text{CCl}_4$  is 91.3 Torr at room temperature.

## CHAPTER 5

### CHLORINE *K-L* RESULTS

In this chapter, data from the Cl *K-L* x-ray emission is presented at three energy ranges. The first energy range of interest is on and around the first absorption resonance of each molecule. The second energy range is over the second molecular resonance, the *4p* and the *np* Rydbergs, and the IP. The third and final energy range corresponds to excitation to the continuum. In each of the energy regions, four parameter will be discussed to characterize the data for each molecule, namely the peak-widths, dispersion, spin-orbit ratio (SO ratio), and polarization.

#### Cl *K*-Edge Absorption

Absorption measurements were made at the Cl *K*-edge for CCl<sub>4</sub>, CFCl<sub>3</sub>, CF<sub>2</sub>Cl<sub>2</sub>, and CF<sub>3</sub>Cl from 2800 to 2900 eV. From 2800 to 2810 eV and from 2830 to 2900 eV, absorption measurements were made with 0.5 eV steps and 3 s dwell time; between 2810 and 2830 eV, where the pre-edge features are located, the steps were shortened to 0.1 eV with a 3 s dwell time to maximize resolution.



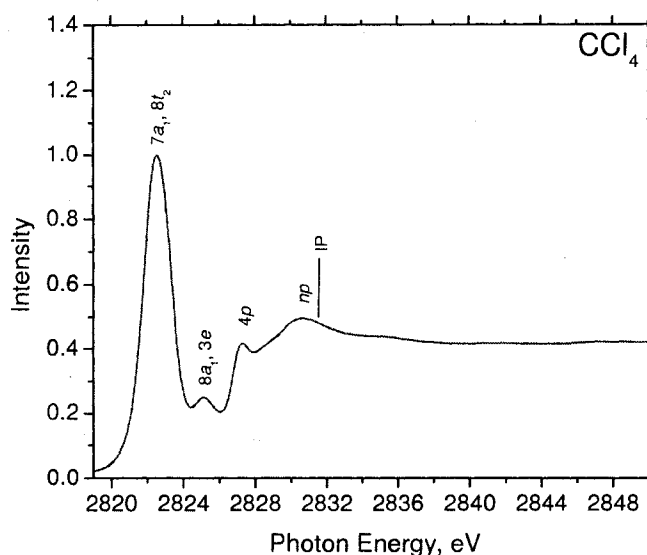


Figure 24. X-Ray absorption spectrum of  $\text{CCl}_4$  from 2810 to 2850 eV collected near the Cl  $K$ -edge. Energy assignments of the peaks were taken from Potts et al [63].

For  $\text{CCl}_4$ , there are four absorption resonances below the IP (2831.2 eV) and a broad shape resonance above the IP at 2880 eV (not shown); see Figure 24. These four peaks correspond to the Cl  $1s \rightarrow 7a_1, 8t_2$  transition (2822.5 eV) with a measured full width at half maximum (FWHM) of 1.7 eV,  $1s \rightarrow 8a_1, 3e$  transition (2825.1 eV) with a FWHM of 1.7 eV,  $1s \rightarrow 4p$  transition (2827.3 eV) with a FWHM of 1.4 eV and the  $1s \rightarrow np$  (2830.6 eV) with a FWHM of 4.6 eV. Peak assignments for  $\text{CCl}_4$  were taken from reference [66].

In  $\text{CFCl}_3$ , there are three resonances below the IP (2829.3 eV) and two above; see Figure 25. The main resonance corresponds to the Cl  $1s \rightarrow 11a_1$  transition (2822.8 eV) with a FWHM of 1.0 eV, the second corresponds to the  $1s \rightarrow 11e, 13a_1$  (2825.7 eV) with a FWHM of 1.3 eV and the third is the  $1s \rightarrow 4p$  Rydberg (2827.2 eV) with a FWHM of 1.1 eV. Above the IP, the broad low-energy peak is a multielectron peak at 2830.0 eV with a

FWHM of 3.6 eV and the one at 2875 eV (not shown) is due to a shape resonance [30, 31].

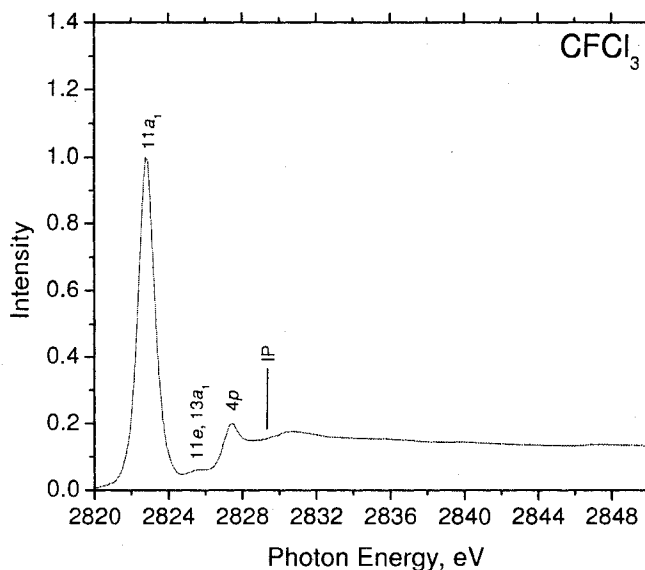


Figure 25. Same as Figure 24 except for  $\text{CFCl}_3$  and assignments were taken from [30].

In the absorption spectrum of  $\text{CF}_2\text{Cl}_2$ , there are four resonances below the IP (2829.6 eV) and a broad shape resonance at 2875 eV above the IP (not shown); see Figure 26. The first resonance is the  $1s \rightarrow 13a_1, 10b_2$  (2823.0 eV) with a FWHM of 1.2 eV, the second is the  $1s \rightarrow 14a_1, 6b_1$  resonance (2826.3) with a FWHM of 1.2 eV the third is the  $1s \rightarrow 4p$  Rydberg (2827.2 eV) with a FWHM of 1.1 eV and the fourth is the  $1s \rightarrow np$  Rydberg (2829.1 eV) with a FWHM of 2.5 eV [30, 31].

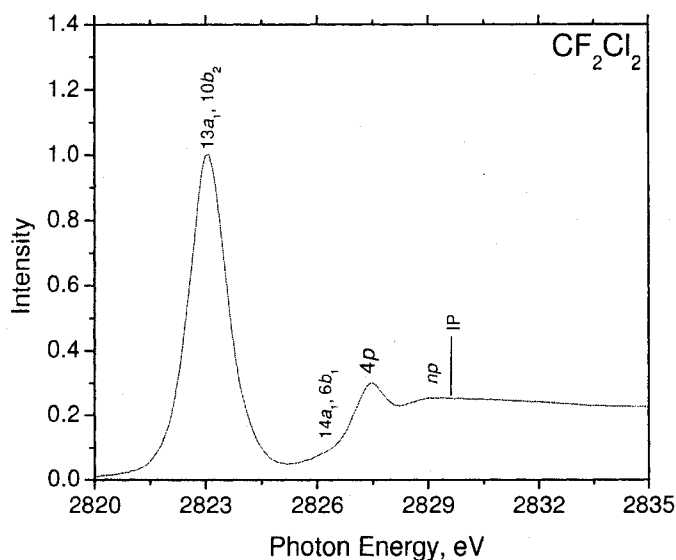


Figure 26. Same as Figure 25 except for  $\text{CF}_2\text{Cl}_2$ .

In  $\text{CF}_3\text{Cl}$ , there are also four absorption resonances below the IP (2830.2 eV) with one broad shape resonance far above the IP at 2875 eV (not shown); see Figure 27. The main absorption resonance corresponds to the  $1s \rightarrow 11a_1$  transition (2823.5 eV) with a FWHM of 1.740 eV, the second, small amplitude, resonance corresponds to the  $1s \rightarrow 12a_1, 8e$  resonance (2827.4 eV) with a FWHM of 1.7 eV, the third is the  $1s \rightarrow 4p$  Rydberg (2827.8 eV) with a FWHM of 1.3 eV and the final corresponds to the  $1s \rightarrow np$  Rydberg (2829.2 eV) with a FWHM of 2.4 eV [31]. Peak assignments for  $\text{CFCl}_3$ ,  $\text{CF}_2\text{Cl}_2$  and  $\text{CF}_3\text{Cl}$  were all taken from reference [30]. Table 2 shows a comparison of FWHM for all four molecules.

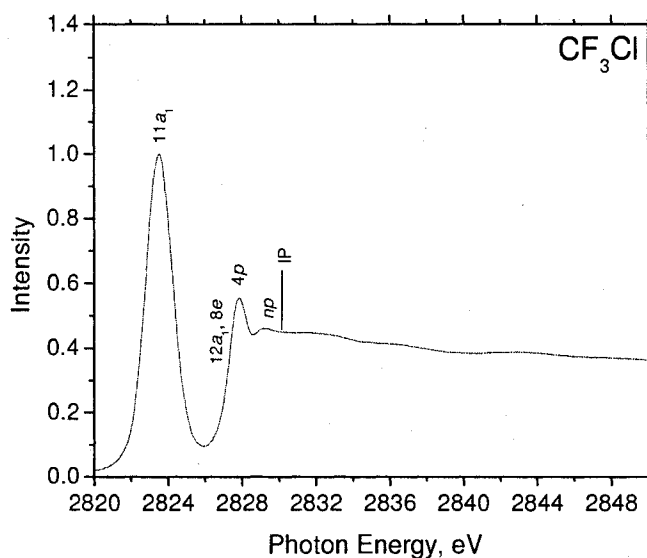


Figure 27. Same as Figure 25 except for  $\text{CF}_3\text{Cl}$ .

As seen in Figures 24 – 27 and in Table 2, the absorption spectra are changing dramatically from  $\text{CCl}_4$  to  $\text{CF}_3\text{Cl}$ . The addition of fluorine atoms to the molecule (and therefore the subtraction of chlorine atoms) is increasing the energy of the main absorption resonance. This is also increased from the measured energy position of the main resonance in  $\text{Cl}_2$  which occurs at 2821.3 eV with a FWHM of ~1.6 eV [40]. This corresponds to a 1.2 eV increase for  $\text{CCl}_4$ , 1.5 eV for  $\text{CFCl}_3$ , 1.7 eV for  $\text{CF}_2\text{Cl}_2$ , and 2.2 eV for  $\text{CF}_3\text{Cl}$ . The decrease in energy from molecular chlorine is from the enhanced electronegativity of the fluorine atoms, which withdraws electrons from the rest of the molecule. This then destabilizes the core-hole state and increases the energy of the LUMO. The molecules  $\text{CCl}_4$  and  $\text{CF}_3\text{Cl}$  have the same measured FWHMs (1.7 eV) and are close to the estimated peak width of  $\text{Cl}_2$  (~1.6 eV) while  $\text{CFCl}_3$  and  $\text{CF}_2\text{Cl}_2$  have a

much narrower FWHM (1.0 eV and 1.2 eV, respectively); this agrees with the Lindle et al [30] where the FWHM is also larger in CF<sub>3</sub>Cl over the main resonance.

Table 2. Measured FWHM of the pre-edge features of CCl<sub>4</sub>, CFCl<sub>3</sub>, CF<sub>2</sub>Cl<sub>2</sub>, and CF<sub>3</sub>Cl.

<i>Peak</i>	<i>Position</i>	<i>FWHM</i>
<b>CCl<sub>4</sub></b>		
7a <sub>1</sub> , 8t <sub>2</sub>	2822.5 eV	1.7 eV
8a <sub>1</sub> , 3e	2825.2 eV	1.7 eV
4p	2827.3 eV	1.4 eV
np	2830.6 eV	4.6 eV
<b>CFCl<sub>3</sub></b>		
11a <sub>1</sub>	2822.8 eV	1.0 eV
11e, 13a <sub>1</sub>	2825.7 eV	1.3 eV
4p	2827.2 eV	1.1 eV
<b>CF<sub>2</sub>Cl<sub>2</sub></b>		
13a <sub>1</sub> , 10b <sub>2</sub>	2823.0 eV	1.2 eV
14a <sub>1</sub> , 6b <sub>1</sub>	2826.3 eV	1.2 eV
4p	2827.2 eV	1.1 eV
np	2829.1 eV	2.5 eV
<b>CF<sub>3</sub>Cl</b>		
11a <sub>1</sub>	2823.5 eV	1.7 eV
12a <sub>1</sub> , 8e	2827.4 eV	1.7 eV
4p	2827.8 eV	1.3 eV
np	2829.2 eV	2.4 eV

The most dramatically changing feature in the absorption spectra is the 2<sup>nd</sup> molecular resonance. In CCl<sub>4</sub>, this resonance is well defined with peak energy of 2825.2 eV. In CFCl<sub>3</sub>, the second molecular resonance is still prominent in the valley between the main resonance and the 4p Rydberg with peak energy of 2825.7 eV but less intense. In CF<sub>2</sub>Cl<sub>2</sub> and CF<sub>3</sub>Cl the 2<sup>nd</sup> molecular resonance is diminished and barely visible between the main resonance and the Rydbergs. In all molecules, the second molecular resonance is

comprised of orbitals oriented along the symmetry axis ( $a_1$ ) and those oriented perpendicular ( $e$  or  $b_1$ ) and excitations to these MOs perpendicular to the molecular-symmetry axis are less probable (not as much overlap with the  $1s$  orbital).

In these molecules, the position of the  $4p$  Rydberg is in relatively the same position; 2827.4 eV in  $\text{CCl}_4$ , 2827.2 eV in  $\text{CFCl}_3$ , 2827.2 eV in  $\text{CF}_2\text{Cl}_2$ , and 2827.8 eV in  $\text{CF}_3\text{Cl}$ . The  $4p$  Rydberg is largely Cl in nature (just as the  $1s$  is effectively Cl in nature), and the position of this orbital changes very little from molecule to molecule. The same is true for the  $np$  Rydberg, which also changes little from molecule to molecule (2830.6 eV in  $\text{CCl}_4$ , 2829.1 in  $\text{CF}_2\text{Cl}_2$ , and 2829.2 eV in  $\text{CF}_3\text{Cl}$ ).

As for the IPs,  $\text{CCl}_4$  has the largest IP at 2831.2 eV,  $\text{CF}_3\text{Cl}$  is next with an IP of 2830.2 eV,  $\text{CFCl}_3$  has an IP of 2829.8 eV, and finally  $\text{CF}_2\text{Cl}_2$  has an IP of 2829.6 eV. Molecular chlorine has an IP of 2830.2 eV, so  $\text{CCl}_4$  has a higher IP,  $\text{CF}_3\text{Cl}$  has the same IP and  $\text{CFCl}_3$  and  $\text{CF}_2\text{Cl}_2$  have lower IPs. In these molecules, symmetry has the largest effect on the ionization energy. The molecule  $\text{CCl}_4$  is in the  $T_d$  point group and has the most symmetry, followed by  $\text{CF}_3\text{Cl}$  and  $\text{CFCl}_3$ , which have  $C_{3v}$  symmetry and then  $\text{CF}_2\text{Cl}_2$  with  $C_{2v}$  symmetry. In these molecules, the degree of symmetry and the IP are related; the more symmetry the molecule has, the higher the IP (or the more difficult it is to remove the  $1s$  electron). Removing a core electron changes the symmetry of the molecule; the core hole causes the outer electrons to rearrange in such a way as to stabilize the core-hole. The rearrangement of electrons can change the equilibrium bond lengths and the bond angles thus reducing the symmetry. Molecules with low symmetry are less affected by the rearrangement of the molecule (lower IP) than those with high symmetry (higher IP).

## Cl *K-L* Emission

### Cl $1s \rightarrow \text{LUMO}$

The data presented in the section is the *K-L* emission on and around the first absorption resonance, the Cl  $1s \rightarrow \text{LUMO}$  (lowest unoccupied molecular orbital); see Figure 28. The incident photon energy was detuned from the top of the resonance in 0.3 eV steps on the high and low energy sides of the resonance and emission spectra were taken in both polarization directions at each incident photon energy; see Figure 29. The detuning ( $\Omega$ ) is defined in Chapter 2, page 13 and is  $\Omega = \omega' - \omega$  where  $\omega$  is the frequency of the incident photons at the maximum of the resonance and  $\omega'$  is the monochromator photon energy; the detuning is the difference between the top of the resonance and the actual photon energy. As seen from Figure 29, as the incident photon energy is detuned away from the top of the main absorption resonance, the peaks become very broad; which is true for both polarization directions. The most dramatic change in peak width occurs at  $\Omega = -1.2$  in both polarizations where the two peaks begin to merge together. Also, the peak broadening is independent of the molecule being examined. Also seen in Figure 29, as the incident photon energy is detuned from the absorption maxima, the energy position (dispersion) of the peaks is changing with photon energy. The change of peak width and energy dispersion will be further discussed in the next sections.

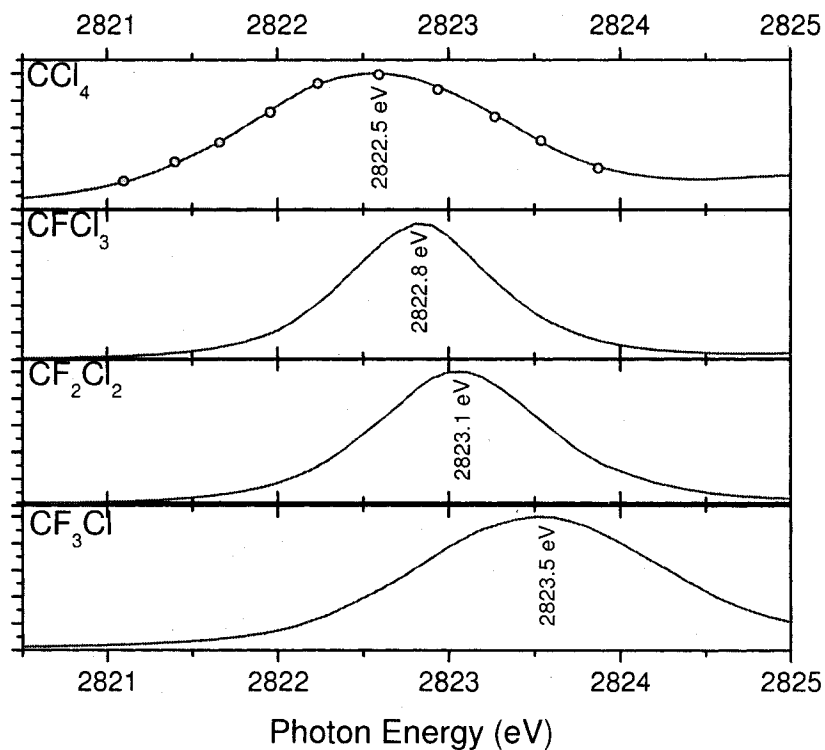


Figure 28. X-Ray absorption spectra taken on and around the  $1s \rightarrow \text{LUMO}$  for  $\text{CCl}_4$ ,  $\text{CFCF}_3$ ,  $\text{CF}_2\text{Cl}_2$ , and  $\text{CF}_3\text{Cl}$ . Grey dots on the absorption spectra of  $\text{CCl}_4$  represent incident photon energies where emission spectra were collected in both polarization directions.



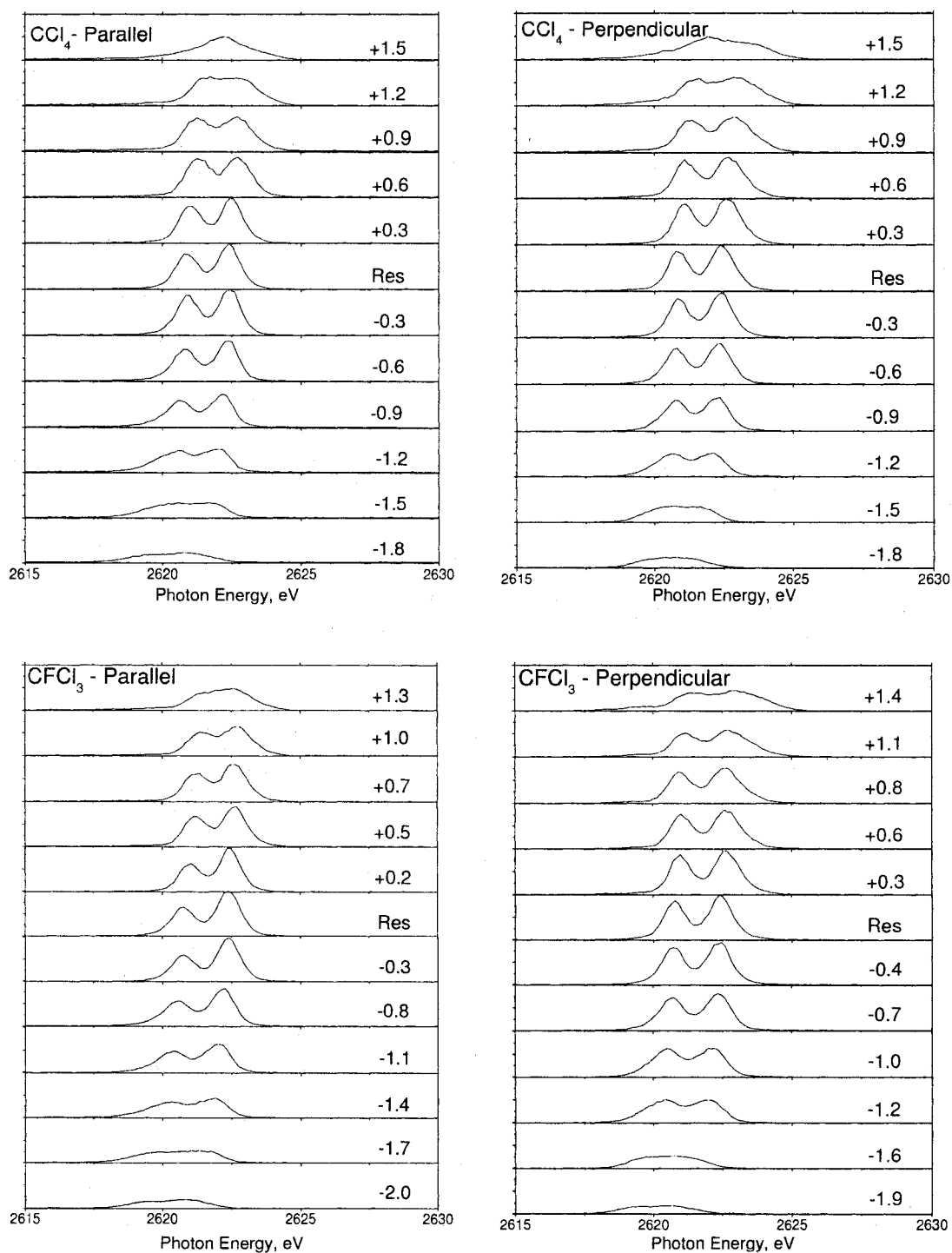


Figure 29 (a). X-ray emission spectra at various photon energies on and around the main resonance taken in both polarization directions for  $\text{CCl}_4$  and  $\text{CFCl}_3$ .

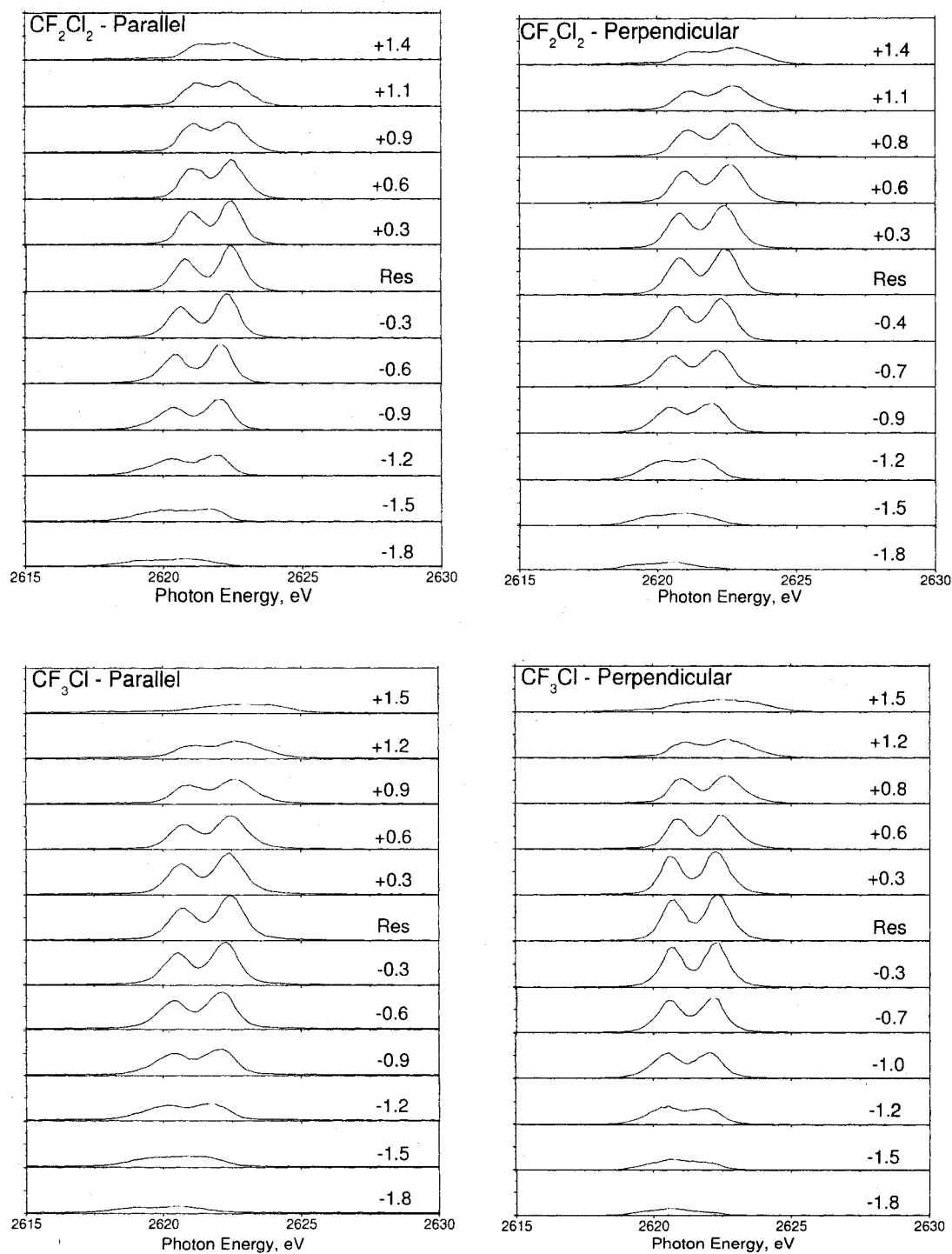


Figure 29 (b). X-ray emission spectra at various photon energies on and around the main resonance taken in both polarization directions for  $\text{CF}_2\text{Cl}_2$  and  $\text{CF}_3\text{Cl}$ .

### *Peak-Widths*

The x-ray emission peak-widths were measured as a function of photon energy in both polarization directions; see Figure 30. On top of the resonance ( $\Omega = 0$ ), the peak widths of all four molecules reach a minimum in both polarization directions and increase as the photon energy is moved away from the top of the resonance, as seen first by Eisenberg [8] and recently by Simon [15] and been well established in theoretical models for quite some time [8, 23, and 24]. The peak widths fall in a parabola from  $+1.5 < \Omega < -1.5$  in both polarizations ( $y \approx 0.3x^2 + 0.1x + 0.9$ , where  $y$  is the width and  $x$  is the detuning) and below  $\Omega = -1.5$ , the peak widths fall off with large negative detuning and approach a value of 1.2 (as seen in the perpendicular direction). When comparing all four molecules, there is no difference in peak widths over the first resonance in the parallel and perpendicular polarization directions.

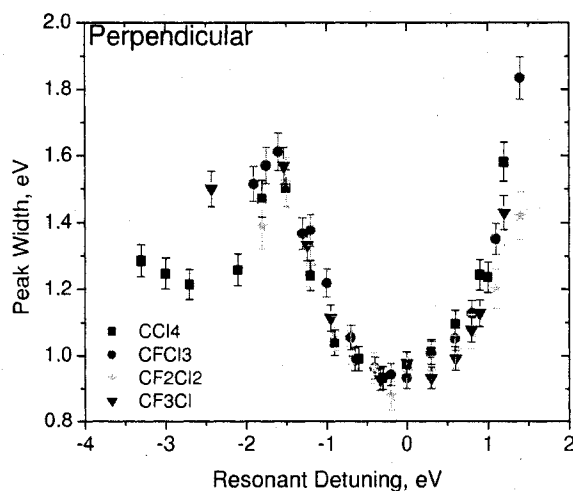
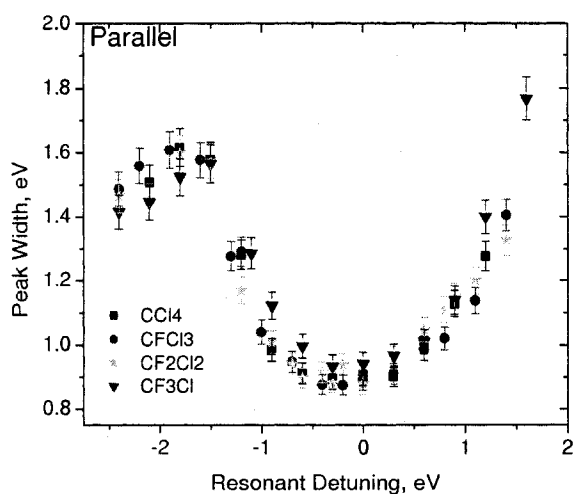


Figure 30. Measured x-ray emission peak widths on and around the first absorption resonance in the parallel orientation (top) and the perpendicular orientation (bottom) plotted versus resonant detuning.

The chlorine  $1s$  and  $2p$  have parallel potential surfaces even at large internuclear distances and have been calculated by Simon and Gel'mukhanov [15, 23]. The shapes of the potential surfaces play large roles in determining the Franck-Condon (FC) factors, or the transition strength of the  $2p$  and  $1s$  states [23]. The FC factors include contributions

from the photon function, the lifetime broadening function, and the vibrational distribution function. The resonant x-ray scattering cross section ( $\sigma$ ), or the probability that a scattering event will take place, is given by a bound-free (since the final state is dissociative) FC factor and a Lorentzian function from equation 18 in Chapter 2. The relationship is as follows:

$$\sigma(\omega, \omega_1) \propto \frac{F(\Omega_1 - \Omega)}{\Omega_1^2 + \Gamma^2 / 4} \quad (18)$$

here  $F(\Omega_1 - \Omega) \propto \exp\{ -[(\Omega_1 - \Omega)/\Delta]^2 \ln 2 \}$  is the FC factor that approximates the contributions from the incident radiation as a Gaussian function; a Gaussian function duplicates the shape of the incident spectral line and is convenient in numerical calculations. Also,  $\omega$  is the frequency of the initial photon, and  $\omega_1$  is the frequency of the emitted photon. Similar to the definition of detuning,  $\Omega_1 = \omega_1 - \omega(\infty)$  where  $\omega(\infty)$  is the resonant frequency of an isolated Cl atom. The final parameter,  $\Delta$  is  $\approx 1.68$  eV and is the full width at half maximum of the FC factor [15]. The way in which the spectral widths  $\Gamma(\omega)$ , relate to equation 18 is as follows [23]:

$$\Gamma(\omega) \propto \left( \frac{\Delta \Gamma}{w(\omega) \ln 2 \sqrt{\pi}} - F^2(-\Omega) - \Gamma^2 \right)^{1/2} \quad (33)$$

where  $w(\omega)$  is the error function (Gauss error function)<sup>1</sup> and the Lorentzian function in (18) is considered constant when the spectral width is smaller than the lifetime (0.3 eV compared to 0.6 eV for Cl) [24]. Figure 30a shows a plot of equation 33 for various widths of the Gaussian function ( $\gamma$ ). In this equation, the Gaussian function is dominant

---

<sup>1</sup>  $erf = \frac{2}{\sqrt{\pi}} \int_0^x e^{-t^2} dt$

at small detunings while the error function is dominant at larger detunings. At  $\Omega = 0$ , the Gaussian function reaches a minimum and  $\Gamma(\omega)$  approaches  $\Gamma$  (this is seen in Figure 30a). As the detuning increases, so do the peak widths until they reach the region where the error function is dominating the peak width distribution. At this point, the peak widths fall off and approach  $\Delta/\sqrt{2}$  (1.19 eV), this is an asymptotic value associated with the error function, and agrees well with the data in the perpendicular direction [24]. Because the excitation is from a narrowband source (or  $\gamma \ll \Gamma$ ) where  $\gamma$  is the FWHM of the spectral contribution of the FC factor (0.3 eV at the Cl *K*-edge versus a lifetime of 0.6 eV), the minimum of  $\Gamma(\omega)$  at  $\Omega = 0$  is a manifestation of subnatural width in RXS. Physically, resonant Raman scattering removes the lifetime smearing of the *K*-hole intermediate state (which is seen above the IP) and the resulting peak has a linewidth determined by the excitation beam and not the core-hole lifetime [8].

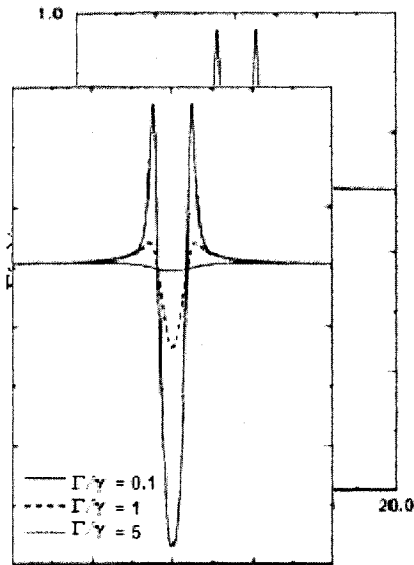


Figure 30a. Dependence of the spectral widths on the resonant detuning of the incident photon taken from Gel'mukhanov and Agren [24].

This phenomenon has been measured extensively in the past [8, 14, and 15] and the data presented in this section agree well with published works. As seen from Figure 30a and equation 33, the dependence of the spectral peak width on resonant detuning has been thoroughly described with theoretical models and has been known for many years [13, 23, and 24]. The data in this section also agrees well with theory.

### *Dispersion*

The x-ray dispersions of  $\text{CCl}_4$ ,  $\text{CFCl}_3$ ,  $\text{CF}_2\text{Cl}_2$ , and  $\text{CF}_3\text{Cl}$  were measured as a function of incident photon energy on and around the first absorption resonance; see Figure 31. On top on the main absorption resonance, the energies of the  $K$ - $L$  emission lines are that of the characteristic Cl atom  $K\alpha$  energies, 2622.39 eV ( $\alpha_1$ ) and 2620.78 eV ( $\alpha_2$ ) for all four molecules and show little (if any) screening effects. When the incident photon energy is close to the top of the resonance ( $-0.5 \text{ eV} < \Omega < +0.5$ ), the dispersion varies slightly from that at the top of the resonance ( $\Omega = 0$ ). Far above and below the top of the resonance, the emission lines linearly increase with increasing photon energy.

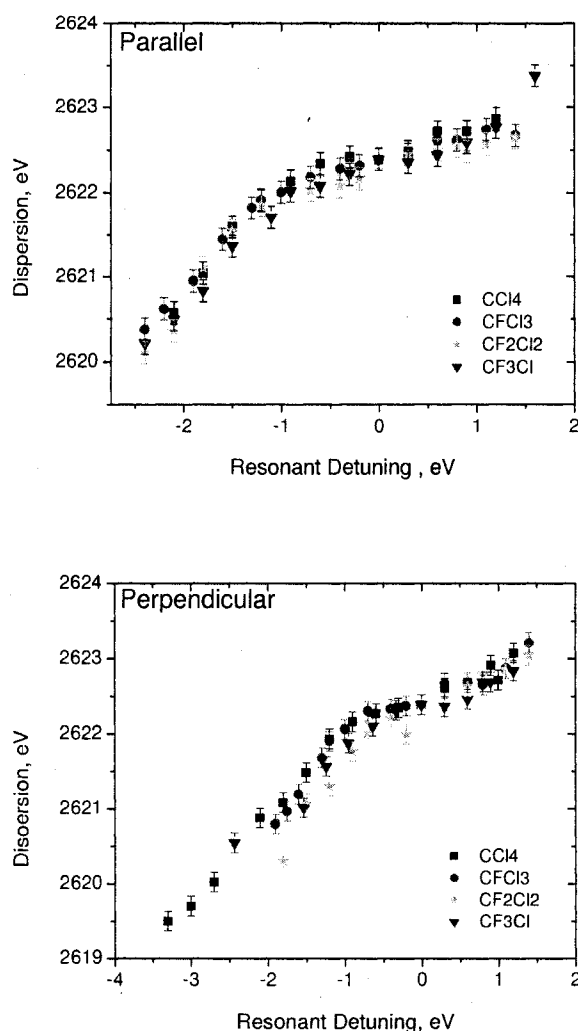


Figure 31. Measured x-ray dispersion on and around the first absorption resonance for CCl<sub>4</sub> (square), CFCl<sub>3</sub> (circle), CF<sub>2</sub>Cl<sub>2</sub> (star), and CF<sub>3</sub>Cl (triangle) in the parallel (top) and the perpendicular (bottom) polarization directions plotted versus resonant detuning.

As seen from Figure 31, the x-ray dispersion for all four molecules and in both orientations is nonlinear, however, it is still dependent on the incoming photon's energy. The dependence of the peak energy dispersion on the incident photon energy has been seen experimentally [8, 14, and 15] and the theory known since 1976 [8], with a more



comprehensive theory in 1996 [24]. The nonlinear dispersion can be a consequence of a number of things; namely when the region of excitation includes several intermediate states, screening effects, or by the presence of vibrational structure [23]; over the main resonance, the nonlinearity is most likely due to the presence of vibrational structure (as was seen in CO) [35] where dramatic lifetime-vibrational interference effects can redistribute intensity in a given spectrum, see Chapter 3, page 30. Similar nonlinear dispersion was also observed in Kr [59] (with different physical explanations). The dispersion varies as a function of incident photon energy as follows [23]:

$$\mathcal{E}(\omega) = \omega_f + \Omega \left( 1 - \frac{\gamma^2}{\Omega^2 + \Gamma^2} \right). \quad (34)$$

In this equation,  $\gamma$  is the resolution (FWHM) of the incident photon (0.3 eV at the Cl  $K$ -edge). When the detuning is small, the right side of equation 34 becomes  $\Omega(1 - (\gamma/\Gamma)^2)$  and the energy of the emitted peak is increasing slowly, as seen in the above data. At large detuning, the right side of 34 becomes  $\Omega - \gamma^2/\Omega$  and the equation approaches Raman-Stokes (linear) behavior (also seen). A plot of the dispersion as a function of incident photon energy is shown in Figure 31a.

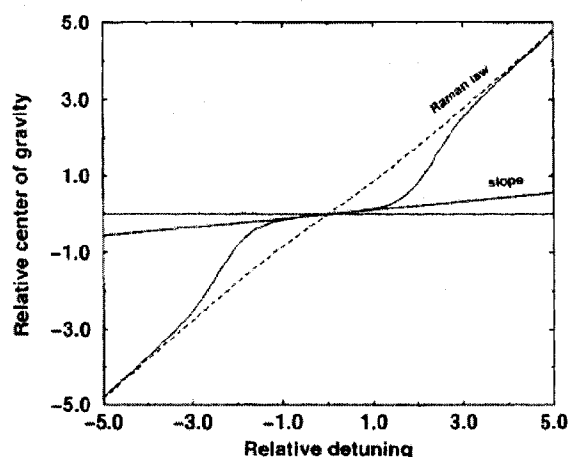


Figure 31a. Dependence of the peak energy dispersion on the incident photon's detuning taken from Gel'mukhanov and Agren [23].

### *Spin-Orbit Ratio*

The third parameter examined in the chlorofluoromethanes is the spin-orbit (SO) ratio and the high-energy, more intense peak is the  $2p_{3/2}$  and the low-energy peak is the  $2p_{1/2}$  as described in Chapter 2. The data presented here is the first detailed examination of the SO ratios of these molecules above and below the IP. In this section, each molecule is plotted separately in Figure 32 to compare the SO ratio in parallel and perpendicular orientations for each molecule and to compare to the statistical 2:1 ratio observed in Ar shown in Chapter 4.

For  $\text{CCl}_4$ , Figure 32(a), the SO ratios follow a "hump-like" spread over the top of the resonance and there is no difference between parallel and perpendicular orientations. In this molecule, the SO ratios are significantly lower than the statistical 2:1 ratio and are changing dramatically with photon energy. In  $\text{CFCl}_3$ , the SO ratios have a similar hump-like dispersion in the parallel direction and increase with increasing photon energy in the

perpendicular; see Figure 32(b). In this molecule, there are large differences in the parallel and the perpendicular orientations close to the top of the resonance (indicating large polarization effects). The SO ratios behave in a similar manner in  $\text{CF}_2\text{Cl}_2$  as they did in  $\text{CFCl}_3$ , Figure 32(c). In the parallel direction, the SO ratios have a double hump-like distribution while in the perpendicular direction, they increase with increasing photon energy. The most dramatic difference in this molecule occurs on the high-energy side of the resonance where the ratios in the parallel direction are decreasing and the perpendicular SO ratios are increasing. Finally,  $\text{CF}_3\text{Cl}$  shows the same pattern in both polarization directions that are seen in  $\text{CF}_2\text{Cl}_2$  and  $\text{CFCl}_3$ ; see Figure 32(d). This molecule also shows significant polarization effects over the main resonance but approach the same value in parallel and perpendicular directions at  $\Omega = 1$ .

Figure 33 shows all four molecules plotted together in both polarization directions. In the parallel direction, all four molecules show the double hump-like distribution with no significant difference among the four molecules over the first hump. Over the top of the resonance,  $\text{CFCl}_3$  has the largest SO ratio (1.7),  $\text{CF}_2\text{Cl}_2$  and  $\text{CF}_3\text{Cl}$  are the same with a SO ratio of 1.4, and finally  $\text{CCl}_4$  has the lowest SO ratio of 1.3. Above  $\Omega = +0.5$ ,  $\text{CFCl}_3$  and  $\text{CF}_3\text{Cl}$  are approaching the same value (1.3) while  $\text{CF}_2\text{Cl}_2$  and  $\text{CCl}_4$  approach the same value (1.0). On the high-energy side of the resonance, the molecules with  $\text{C}_{3v}$  symmetry have the higher SO ratios while  $\text{T}_d$  and  $\text{C}_{2v}$  symmetry have the lower SO ratios. The double-hump distribution is significantly different from the linear increase in SO ratio with increasing photon energy observed in the parallel direction in Ar, see Chapter 4, page 63.

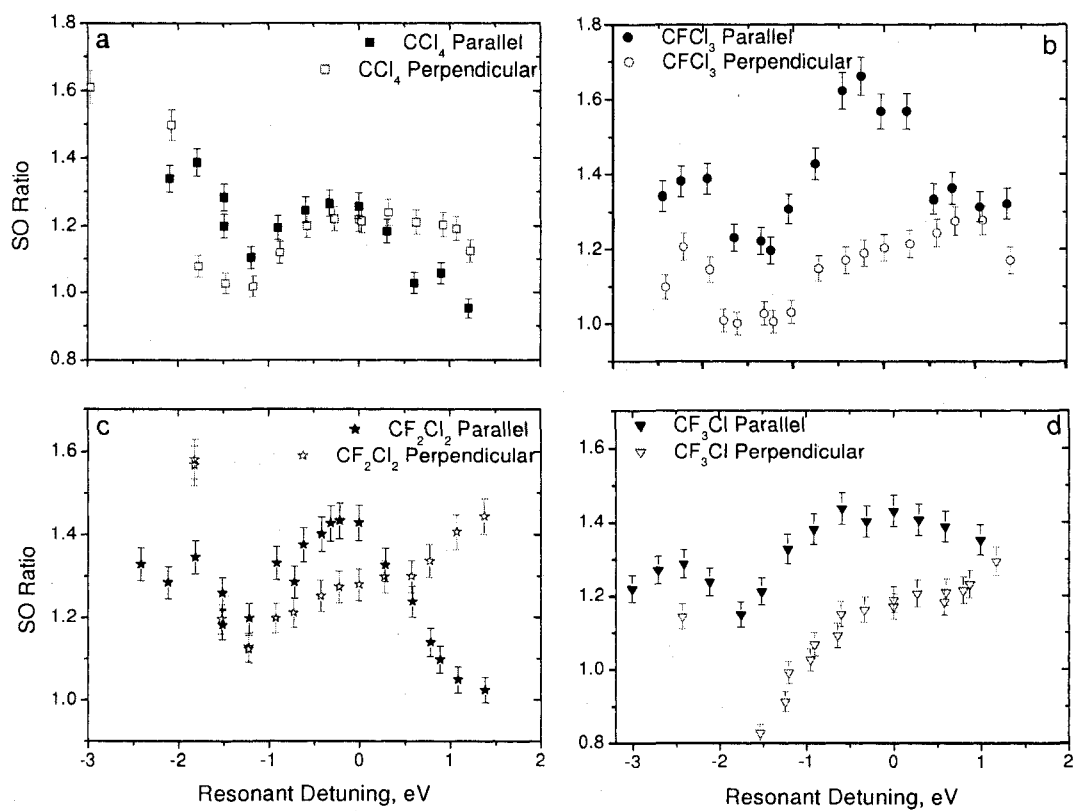


Figure 32. Spin-Orbit (SO) ratio plot for each molecule to compare polarization (parallel with solid symbols; perpendicular with empty). Plot (a) is  $\text{CCl}_4$ , plot (b) is  $\text{CFCl}_3$ , plot (c) is  $\text{CF}_2\text{Cl}_2$ , and plot (d) is  $\text{CF}_3\text{Cl}$ .

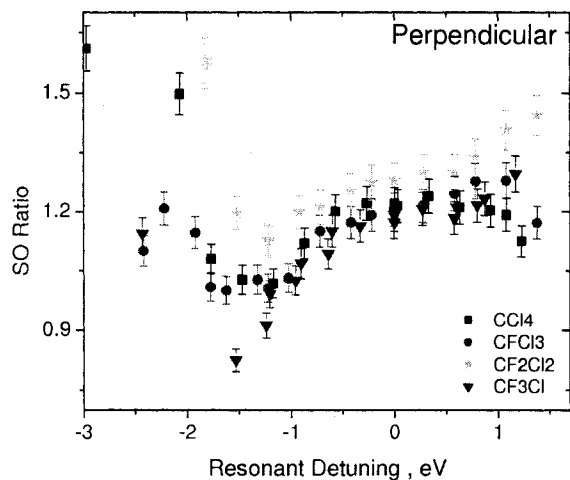
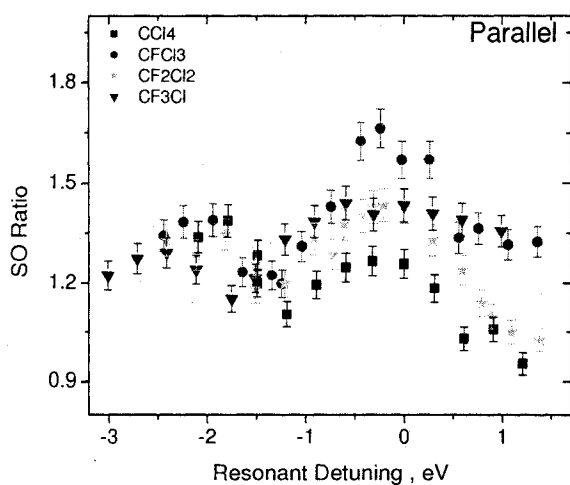


Figure 33. Experimental spin-orbit (SO) ratios for  $\text{CCl}_4$  (square),  $\text{CFCl}_3$  (circle),  $\text{CF}_2\text{Cl}_2$  (star), and  $\text{CF}_3\text{Cl}$  (triangle) in both polarization directions (parallel on top, perpendicular on the bottom) plotted versus resonant detuning.

In the perpendicular direction, around the top of the resonance, there is no difference between the four molecules and the increasing SO ratio with increasing energy mirrors the trend observed in Ar. Above  $\Omega = 1.0$   $\text{CF}_2\text{Cl}_2$  and  $\text{CF}_3\text{Cl}$  continue to increase with

increasing photon energy while  $\text{CCl}_4$  and  $\text{CFCl}_3$  are decreasing and the two groups begin to diverge. In this direction, the molecules with more fluorine atoms have increasing SO ratios while those with more Cl atoms have decreasing SO ratios.

As seen from Figures 32 and 33, the SO ratio never reaches the 2:1 statistical ratio seen in argon above the Ar  $1s$  ionization energy. In argon (Chapter 4, page 63) the SO ratios linearly increase with increasing photon energy in both polarization directions but only reach a value of 1.7 on the top of the resonance. The dependence of photon energy on peak ratio was also seen in the photoelectric spectra of Xe and Kr where the branching ratios (a measure of the peak intensity ratio in photoelectron spectroscopy) of  $4d_{5/2}$  to the  $4d_{3/2}$  and the  $3d_{5/2}$  to the  $3d_{3/2}$ , respectively, change dramatically with photon energy [60, 61].

Close to the top of the resonance in the perpendicular direction, the SO ratios are increasing linearly with photon energy just as seen in Ar but are much lower than the statistical 2:1 ratio. In the parallel directions, the trend in SO ratio is much different (double-hump) and a different mechanism is dominant. The dramatic differences in the Cl SO ratios compared to the SO ratios seen in Ar can be attributed to molecular field effects, where the nonspherical symmetry of the molecule provides another axis along which the  $2p$  orbitals can be aligned (they now also have  $m_l$  values with respect to the axis); this effect can raise or lower the SO ratio depending on the field. Significant MF effects have been measured in the photoelectron spectra of Cl in HCl [45] and other molecules [42]. In these cases, the MF couples with the SO interaction to stabilize the core-hole causing the branching ratio, and the energy difference between the two peaks (and also differences in the  $2p_{3/2}$  doublet), to vary with photon energy. In these

molecules, symmetry changes (changes in bond lengths and bond angles) have various degrees of MF coupling and can explain the differences seen among the molecules, as they have varying types of symmetry. The stabilization of  $2p\sigma$  types of orbitals with  $\sigma$ -bond interactions (here, sigma is used to describe MOs symmetric about the main symmetry axis and  $\pi$  to refer to those perpendicular to it) explains the larger MF effects in the parallel direction compared to the perpendicular. The  $\sigma$ -types of orbitals are symmetric about the symmetry axis so the effects are greater in the parallel direction [42]. As seen in this section, MF effects result in a SO ratio that is significantly lower than the 2:1 theoretical ratio.

### *Polarization*

The final parameter examined in this energy range is the polarization; where the difference in x-ray emission spectra in the parallel and the perpendicular direction determine the degree of polarization. In this analysis, the intensity of a given x-ray emission peak from the parallel orientation is compared to the same peak in the perpendicular orientation; both of which are at the same incident photon energy.

Polarization ( $P$ ) is calculated from experimental values as follows:

$$P = \frac{I_{\parallel} - I_{\perp}}{I_{\parallel} + I_{\perp}}, \quad (38)$$

where  $I_{\parallel}$  is the integrated relative intensity in the parallel direction and  $I_{\perp}$  is the intensity in the perpendicular direction (theoretical models were shown in Chapter 2, pages 16-19). For the  $K$ - $L$  energy range, the polarization ratio ( $P_{\alpha_1}/P_{\alpha_2}$ ), where  $K\alpha_1$  is peak 1 and  $K\alpha_2$  is peak 2, is more useful because it removes any experimental differences between parallel and perpendicular orientations (i.e. counting times, spectrometer efficiency, solid

angle...). Figure 34 shows the polarization ratios for  $\text{CCl}_4$ ,  $\text{CFCl}_3$ ,  $\text{CF}_2\text{Cl}_2$  and  $\text{CF}_3\text{Cl}$  over the main resonance.

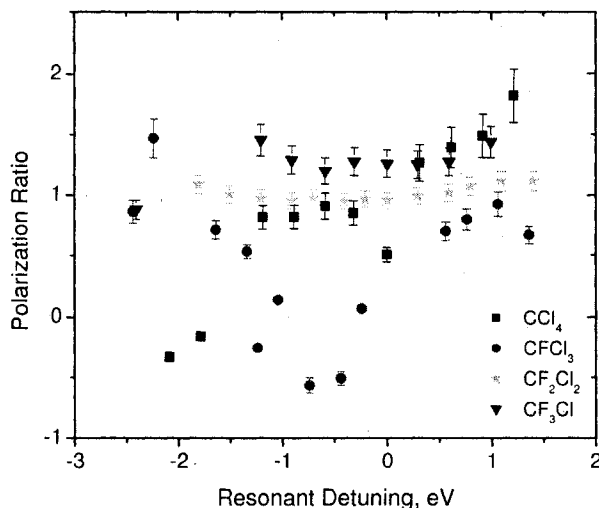


Figure 34. Polarization ratio [ $P$  (peak 1)/ $P$  (peak 2)] over the first resonance for  $\text{CCl}_4$ ,  $\text{CFCl}_3$ ,  $\text{CF}_2\text{Cl}_2$ , and  $\text{CF}_3\text{Cl}$ .

As seen from Figure 34, the largest polarization effect is seen in  $\text{CFCl}_3$ ; especially near the top of the resonance ( $\Omega = 0$ ) and the polarization ratios of  $\text{CF}_2\text{Cl}_2$  and  $\text{CF}_3\text{Cl}$  remain essentially constant over the resonance with a ratio around 1.0. In  $\text{CCl}_4$ , however, the polarization ratios are increasing over the resonance. Just as in the SO ratios, differences in the polarization ratios among the four molecules can be attributed to molecular field effects. The largest difference is seen in  $\text{CFCl}_3$  where the polarization ratio becomes negative over the top of the main resonance. This indicates that the intensities of peak 1 and peak 2 are not changing at the same rate in the parallel and perpendicular orientations (resulting in a ratio that is different from one). This is probably occurring in the parallel direction and can be seen experimentally, where  $\text{CFCl}_3$



has the largest difference in Figure 33. This can be physically from  $\sigma$ -(symmetric about the axis) bond stabilization, which has large MF effects visible in the parallel direction. The negative ratio also indicates that one of the two peaks is more sensitive to the MF effects and should have a large contribution parallel to the symmetry axis. In  $\text{CCl}_4$ , the MF effects are largest on the high-energy side of the resonance.

#### $\text{Cl } 1s \rightarrow 4p$

The next section of *K-L* data occurs just after the first absorption resonance to just above the ionization potential (IP); this includes the 2<sup>nd</sup> molecular resonance, the 4*p* and the *np* Rydberg states, and the IP. As with the preceding *K-L* data around the main resonance, the data around the  $\text{Cl } 1s \rightarrow 4p$  transition is broken up into four sections discussing the peak widths, x-ray dispersion, the spin orbit ratios, and the polarization.

#### *Peak Widths*

Figure 35 shows the measured x-ray peak widths of  $\text{CCl}_4$ ,  $\text{CFCl}_3$ ,  $\text{CF}_2\text{Cl}_2$ , and  $\text{CF}_3\text{Cl}$  over the  $1s \rightarrow 4p$  resonance in both polarization directions plotted with the absorption spectra. Similar to the peak widths over the main resonance, the peak widths over the 2<sup>nd</sup> molecular resonance and the 4*p* Rydberg show the same parabolic shape; having a minimum on the top of the resonance in all four of the molecules and in both polarization directions. Over the *np* Rydberg, the peak widths decrease slowly from 1.3 to 1.0 eV in both polarization directions; the decrease of peak width on top of a resonance occurs whether the orbital is molecular in origin or Rydberg as is clearly shown in Figure 35. Past the *np* Rydberg, the peak widths remain at 1.0 eV in the parallel direction. In the

perpendicular direction, the peak widths in  $\text{CCl}_4$  decrease to 0.9 eV close to the IP ( $\Omega = 8.6$  eV) but remain at 1.0 eV above.

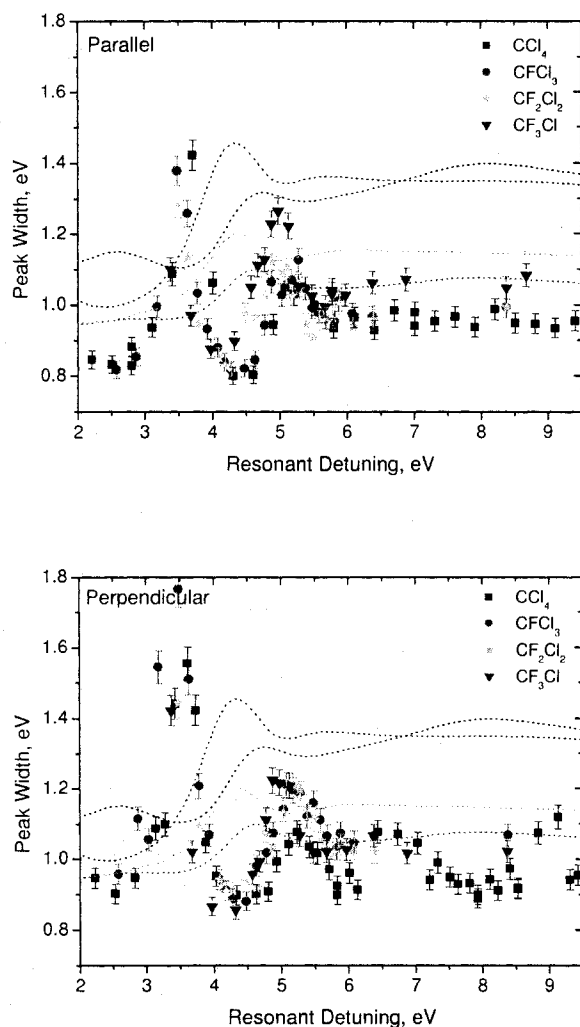


Figure 35. Peak widths versus resonant detuning over the Cl  $1s \rightarrow 4p$  resonance for parallel (top) and perpendicular (bottom) polarization orientations with the absorption spectra as dotted lines.

As with the peak widths over the main resonance, the RXS spectral lines become broad as the incident energy is moved from the top of the 2<sup>nd</sup> molecular, the 4p Rydberg

or the *np* Rydberg. Equations 20-23 explain the broadening over these resonances, which was seen over the main resonance and previously [8, 15].

### *Dispersion*

Similar to the effect seen over the main resonance, the x-ray dispersion is the same in both polarization directions and the same for all four molecules; see Figure 36. Between the second molecular resonance and the *4p* resonance, there is *negative* dispersion; or the energy of the peak positions is *decreasing* with incident photon energy. Over the *4p* resonance, the peak position increases from 2622.0 eV on the low energy side of the peak to 2622.4 eV on the top of the resonance; this is true for all molecules in the parallel orientation and all but CF<sub>2</sub>Cl<sub>2</sub>, which has a maximum of 2622.6 eV on resonance in the perpendicular orientation. Like the dispersion over the LUMO, there appears to be little, if any, screening over the 2<sup>nd</sup> molecular resonance and the Rydbergs. Past the resonance on the high-energy side in the parallel direction, CCl<sub>4</sub>, CFCI<sub>3</sub>, and CF<sub>3</sub>Cl essentially remain at 2622.4 eV while CF<sub>2</sub>Cl<sub>2</sub> decreases to 2622.3 eV and remains constant. In the perpendicular orientation, CF<sub>2</sub>Cl<sub>2</sub> and CFCI<sub>3</sub> remain at 2622.4 eV while CCl<sub>4</sub> and CF<sub>3</sub>Cl decrease to 2622.2 eV. Just below the IP, the x-ray energy dispersion of CCl<sub>4</sub> decreases to 2622.3 eV and then remains constant at 2622.4 eV above the IP.

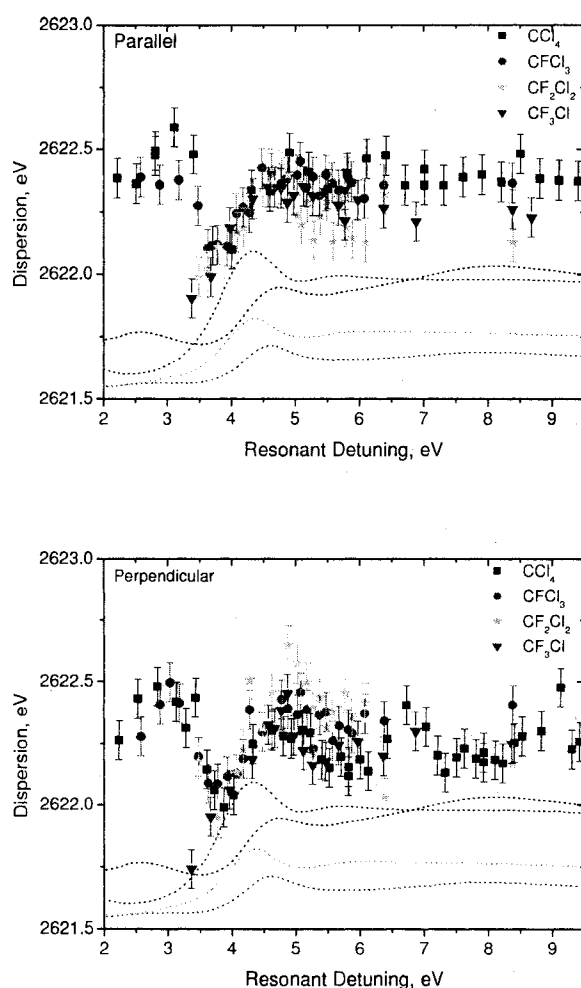


Figure 36. X-Ray dispersion plotted versus resonant detuning over the  $1s \rightarrow 4p$  resonance in the parallel (top) and the perpendicular (bottom) orientations with the absorption spectra.

Unlike the nonlinear dispersion over the main resonance, over the  $4p$  resonance the dispersion is linear; similar to the effect seen in Xe  $L\alpha_1$  and  $L\beta_{2,15}$  [14] and Cu [8]. In this scheme on the low-energy side of the resonance, the x-ray emission is resonance fluorescence that yields a linear dispersion, as seen in Xe. At incident energies approaching the  $np$  resonance, there is a small decrease in peak position in the

perpendicular direction and level off into fluorescence behavior above each molecule's corresponding IPs;  $IP_{CCl_4} = 8.6$  eV,  $IP_{CFCl_3} = 6.5$  eV,  $IP_{CF_2Cl_2} = 6.6$  eV, and  $IP_{CF_3Cl} = 6.7$  eV. The same behavior was seen in all four molecules. In these cases, the width of the spectral profile is given by a sum of the lifetime broadening of the core-excited ( $\Gamma_i$ ) and the final state ( $\Gamma_f$ ) and the peak positions depend on the excitation energy [23] as follows (from Chapter 2, page 14):

$$\omega_i = \omega - \omega_{f0}, \quad (19)$$

where  $\omega_{f0}$  is the resonant frequency of the transition between the ground (0) and the final ( $f$ ) states. This is the Raman Stokes linear shift seen over the 4*p* resonance and stems from the energy conservation law. Although equation 18 predicts a 1:1 linear relation, the molecules in this work have a 1:2 relationship, see Figure 36. This is due to lifetime-vibrational interference that occurs when the vibrational spacing and the lifetime are on the same order of magnitude [35] and can be explained by equation 20. In the case of the chlorofluoromethanes,  $\Omega$  is negative (low-energy side of the 4*p* Rydberg) and  $\omega_f > \omega_i$  which yields a positive slope. Physically, the short lifetime associated with the core-hole state causes broadening of each energy level where there is a possibility of overlap between neighboring vibrational levels. This occurs when the lifetime width is on the same order of vibrational spacing and a given excitation energy may lead to excitation to more than one vibrational level. These levels can decay to the same final state and the coherently excited levels can cause interference effects [35] or deviations from the 1:1 Raman Stokes slope.

The area between  $3.0 < \Omega < 4.0$  shows the first experimental observation of *negative* correlation between incident photon energy and dispersion (slope of  $-0.7$ ). This behavior

is known as anti-Raman behavior and results in a negative x-ray dispersion; this is due to excitation of several intermediate states and was discussed in Chapter 2, page 15 [24]:

$$\varepsilon(\omega) \approx \Omega \left( \frac{\omega_i^2 - \omega_f^2}{2\omega_i^2} \right) + \varepsilon_{if}, \quad (20)$$

where  $\varepsilon(\omega)$  is the center of gravity (dispersion) of the x-rays,  $i$  is vibrational level of the initial (ground) state,  $f$  is the final state, and  $\varepsilon_{if}$  is the frequency of the sudden (vertical) emission transition from the lowest vibrational level of the core-excited state. When the final state is vibronically excited ( $\omega_f > \omega_i$ ), the resulting peak position of the x-ray emission has anti-Raman dispersion (negative slope since  $\Omega$  is positive on the high-energy side of the resonance). This has been calculated for the O  $K$  emission of CO [24]. One can see from Figure 37 that the anti-Raman behavior in CO occurs on the high-energy side of the absorption profile (or at large vibrational excitations) and has contributions from many of the vibrational levels, as was seen in the lifetime-vibrational interference. In Figure 37, the absorption spectrum of oxygen is calculated with all its vibrational contributions (even though the measured absorption is a broad, featureless peak, see Figure 8). The vibrational dependence of the x-ray dispersion is shown over the calculated absorption to demonstrate the negative dispersion. On the low energy side of the resonance, the dispersion is increasing with increasing energy and  $\omega_f \leq \omega_i$ . On the high-energy side of the resonance (the probability of exciting multiple vibrational states is increased), the calculated x-ray dispersion is decreasing and  $\omega_f > \omega_i$ . When the detuning is increased (decreased) far from the top of the resonance, the dispersion approaches the Raman law. The negative dispersion is occurring on the high-energy side

of the 2<sup>nd</sup> molecular resonance where multiple vibrational excitations are probable similar to the calculated dispersion of oxygen.

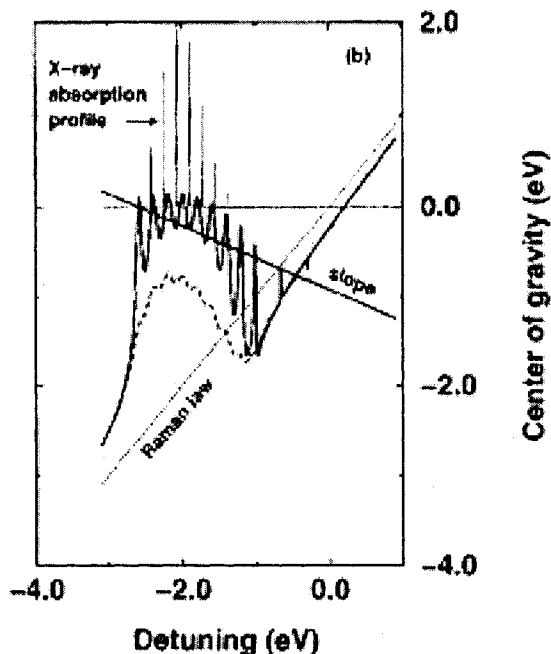


Figure 37. Calculated x-ray dispersion (vertical axis) plotted against resonant detuning (horizontal axis) for CO with the x-ray absorption profile taken from Gel'mukhanov [24].

### *Spin-Orbit Ratio*

Figure 38 shows the SO ratios of CCl<sub>4</sub>, CFCl<sub>3</sub>, CF<sub>2</sub>Cl<sub>2</sub>, and CF<sub>3</sub>Cl in both polarization directions plotted with the absorption spectrum. In CCl<sub>4</sub> and in CFCl<sub>3</sub>, the same trend is seen in the parallel and perpendicular directions over the 2<sup>nd</sup> molecular resonance where the SO ratios decrease rapidly with photon energy. Over 4*p* Rydberg, all four molecules show a decrease in SO ratio with incident photon energy in the parallel direction except for CF<sub>3</sub>Cl where the SO ratios are increasing, see Figure 39. Over the *np* Rydberg, the SO ratios remain essentially constant in all molecules and in both directions except

$\text{CF}_2\text{Cl}_2$  where they increase rapidly with photon energy on the low-energy side of the resonance. This is the same hump-like distribution observed over the LUMO. Past the resonance, the SO ratios remain constant and will be discussed further in the next section.

In Figures 38 and 39, the molecules with the largest differences between parallel and perpendicular directions are  $\text{CFCl}_3$  and  $\text{CF}_3\text{Cl}$ . In argon, the SO ratios are decreasing dramatically over the  $4p$  and  $np$  Rydbergs while in the Cl molecules, all the SO ratios are decreasing over the  $4p$  Rydberg except those in  $\text{CF}_3\text{Cl}$ . The “atomic-like”  $4p$  Rydberg can be broken up into separate components, the  $p$  orbitals perpendicular to the bond axis and the  $p$  orbital that is along the C–Cl bond. Excitation of these different states can lead to different rearrangements of the electron cloud depending on the geometry of the excited state. When the excitation is to orbitals oriented along the bond axis, the MF effects are larger in the parallel direction, as was observed over the main resonance, and conversely, excitations to perpendicular orbitals have small effects. Over the  $4p$  Rydberg, the  $p$ -parallel state is likely to have the largest MF effects and the  $p$ -perpendicular states little effect. From this, the data suggests that the  $\text{C}_{3v}$  molecules are preferentially exciting the  $4p$  state along the bond axis (which manifests itself as rather large MF effects in the parallel direction) and the  $\text{T}_d$  and the  $\text{C}_{2v}$  symmetry molecules are exciting the  $4p$  orbitals perpendicular to the axis (where small MF effects are seen in either direction). This is the first measurement of this type and a theoretical model is needed to understand the physics of these MF effects. Also, it is surprising to see such a dramatic drop in SO ratios over the 2<sup>nd</sup> molecular resonance (the same area where the negative dispersion is seen) and also such a dramatic difference in  $\text{CF}_3\text{Cl}$  compared to the other molecules.



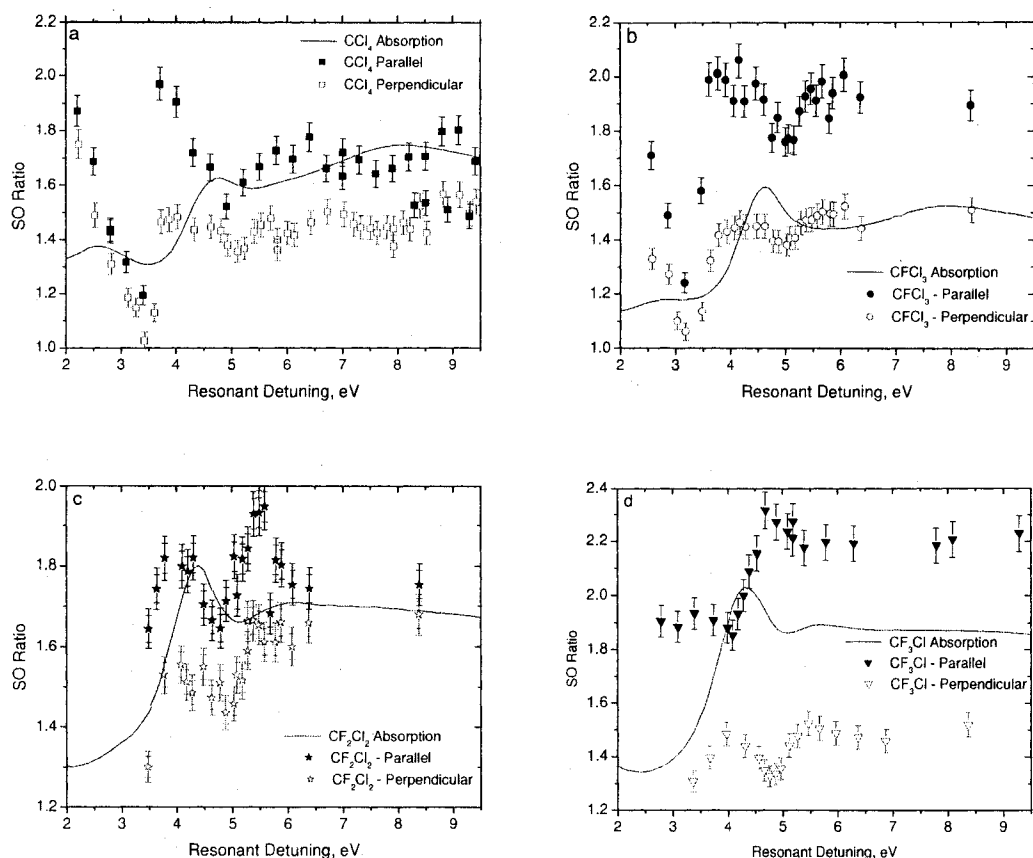


Figure 38. Spin orbit ratios of CCl<sub>4</sub> (a), CFCl<sub>3</sub> (b), CF<sub>2</sub>Cl<sub>2</sub> (c) and CF<sub>3</sub>Cl (d) plotted with the absorption spectrum over the 2<sup>nd</sup> molecular resonance, the 4p and np Rydberg states and the IP.

Figure 39 shows all four molecules plotted together in both polarization directions. In the parallel direction, CCl<sub>4</sub>, CFCl<sub>3</sub>, and CF<sub>2</sub>Cl<sub>2</sub> are essentially the same from  $+2.0 < \Omega < +6.0$ ; all three have the same trend in SO ratio with increasing photon energy with a minimum around  $\Omega = +5.0$ . The decreasing SO ratio over the 4p Rydberg is the same trend observed in argon. However, CF<sub>3</sub>Cl has *increasing* SO ratios with increasing photon energy and a maximum at  $\Omega = +5.0$ . In the perpendicular direction, all four molecules have the same shape from  $+2.0 < \Omega < +9.5$  with CF<sub>2</sub>Cl<sub>2</sub> having slightly larger

values; 1.6 for  $\text{CF}_2\text{Cl}_2$  compared to 1.5 for the other three molecules and also show the decrease in SO ratio over the  $4p$  Rydberg seen in Ar.

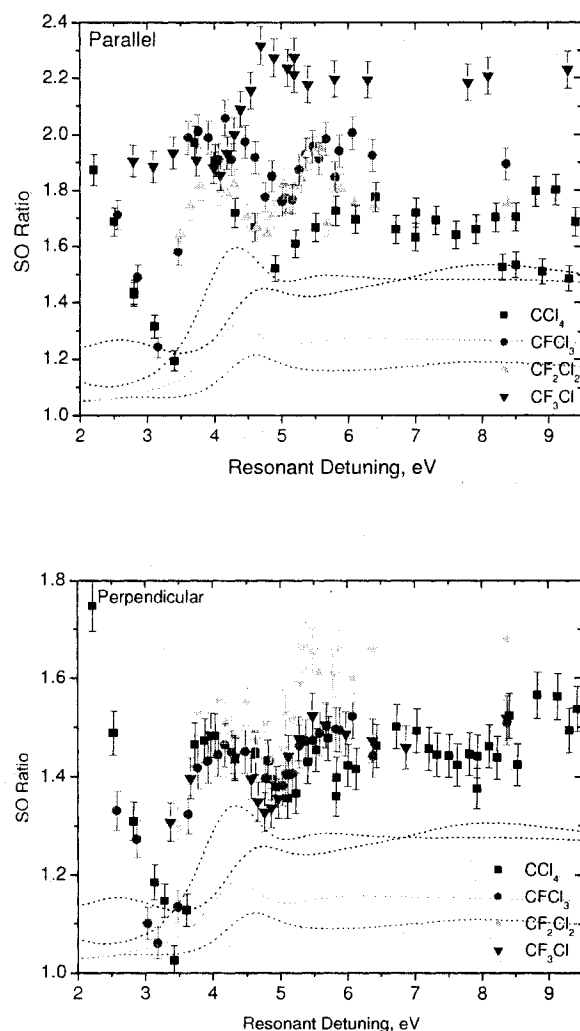


Figure 39. Spin-orbit ratios of  $\text{CCl}_4$ ,  $\text{CFCl}_3$ ,  $\text{CF}_2\text{Cl}_2$ , and  $\text{CF}_3\text{Cl}$  in the parallel (top) and perpendicular (bottom) orientations plotted with the absorption spectra.

### Polarization

The final parameter examined in this energy range is the x-ray polarization ratio; see Figure 40. From this,  $\text{CF}_3\text{Cl}$  and  $\text{CFCl}_3$  have the largest polarization effects;  $\text{CF}_3\text{Cl}$  has

large positive polarization ratios ( $\sim 2.5$ ) while  $\text{CFCl}_3$  has negative polarization ratios ( $\sim -0.5$ ). The polarization ratios of  $\text{CF}_2\text{Cl}_2$  and  $\text{CCl}_4$  are approximately 1.0, which indicates essentially no differences between parallel and perpendicular orientations (especially in  $\text{CF}_2\text{Cl}_2$ ). In this region, the MF effects are the greatest in the molecules with  $\text{C}_{3v}$  symmetry. The large positive SO ratio of  $\text{CF}_3\text{Cl}$  and the negative ratio in  $\text{CFCl}_3$  indicate that peak 1 and peak 2 are not changing in the same manner (one peak is increasing and the other decreasing in a given polarization direction) yielding a ratio different from one, this same effect was seen over the main resonance and suggests that one of the peaks is more sensitive to the MF effects in this energy range with a large contribution in the parallel direction. A theoretical model is also needed to explain these polarization differences.

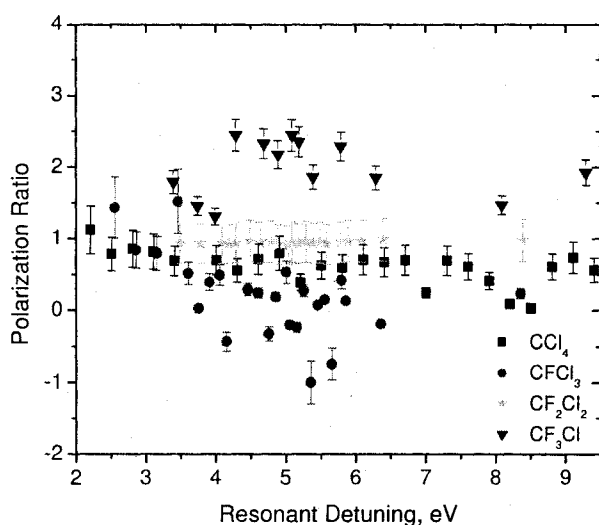


Figure 40. Polarization ratio plot for  $\text{CCl}_4$ ,  $\text{CFCl}_3$ ,  $\text{CF}_2\text{Cl}_2$ , and  $\text{CF}_3\text{Cl}$  over the Cl  $4p$  resonance.

$$\text{Cl } 1s \rightarrow \infty$$

In the final region of the *K-L* data, the *1s* electron is excited into the continuum, or the molecule is ionized; and is unlikely to produce an aligned gas-phase state. In this energy range, there is no difference in parallel and perpendicular orientations for the peak width and the dispersion, as they remain constant from  $+9.5 < \Omega < +70$ . Figure 41 shows the x-ray peak widths from  $\text{CCl}_4$ ,  $\text{CFCl}_3$ ,  $\text{CF}_2\text{Cl}_2$ , and  $\text{CF}_3\text{Cl}$  in the parallel and the perpendicular orientations. In both directions, the peak widths are statistically constant from  $+9.5 < \Omega < +70$ ; both having a width of 1.0 eV.

As seen over the main resonance, as the detuning becomes large (as is the case far above the IP), the peak widths have the following asymptotic behavior  $\Gamma(\omega) = \Delta/\sqrt{2}$  (which includes lifetime broadening effects). In this case, the peak widths are approaching a value of 1.19 eV. This agrees well with the peak width dispersion seen in Figure 41.

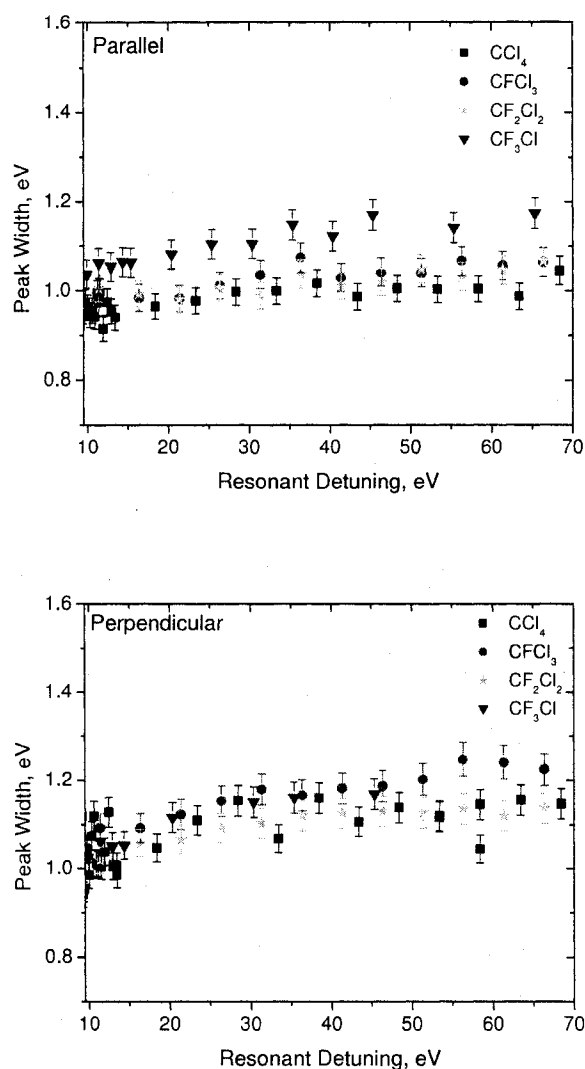


Figure 41. Measured x-ray emission peak widths from  $\text{CCl}_4$ ,  $\text{CFCl}_3$ ,  $\text{CF}_2\text{Cl}_2$ , and  $\text{CF}_3\text{Cl}$  in the parallel (top) and perpendicular (bottom) orientations.

The second parameter of the  $K$ - $L$  data is the x-ray dispersion. Figure 42 shows the change in x-ray dispersion with incident photon energy in both orientations for all four molecules. Above the IP, there is relatively no change in  $K$ - $L$  peak position in either polarization direction. Similar to the peak widths, there are small fluctuations at higher

photon energies due to satellite excitations and shape resonances (due to the molecular field). This agrees well with previous work [8, 14]. The general trends in peak width and dispersion are well known experimentally [8, 14] and theoretically [8, 23, 24].

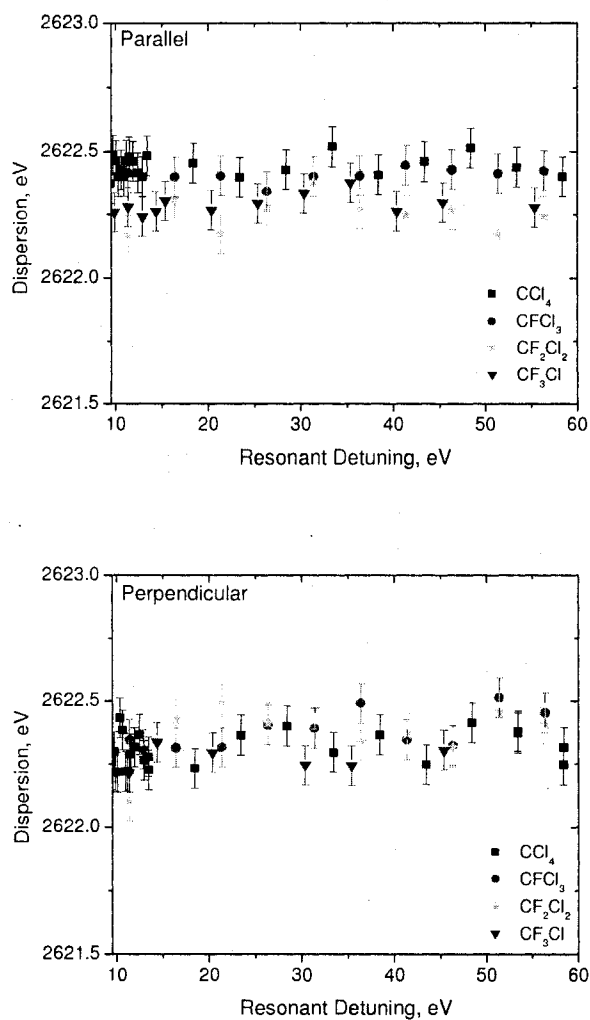


Figure 42. X-Ray dispersion in the parallel (left) and perpendicular (right) polarization directions above the ionization potential.

Like the peak widths and the x-ray dispersion, the SO ratios remain constant when the excitation is to the continuum, however, there are differences in the polarization directions and among the four molecules; see Figure 43. In the parallel orientation,  $\text{CF}_3\text{Cl}$  has the highest SO ratio (2.1),  $\text{CF}_2\text{Cl}_2$  and  $\text{CFCl}_3$  are statistically the same with a SO ratio of 1.8, finally,  $\text{CCl}_4$ , has the lowest SO ratio at 1.6. Also, the SO ratios of  $\text{CCl}_4$  are oscillating around the value of 1.6 above the IP which is a phenomenon not seen in any of the other molecules; see Figure 44. This trend is not a consequence of experimental fluctuations, however, as the SO ratios are highly reproducible. In the perpendicular direction,  $\text{CCl}_4$ ,  $\text{CFCl}_3$ , and  $\text{CF}_3\text{Cl}$  are the same with a SO ratio of 1.5; while the SO ratio for  $\text{CF}_2\text{Cl}_2$  is higher in the perpendicular direction (1.6).

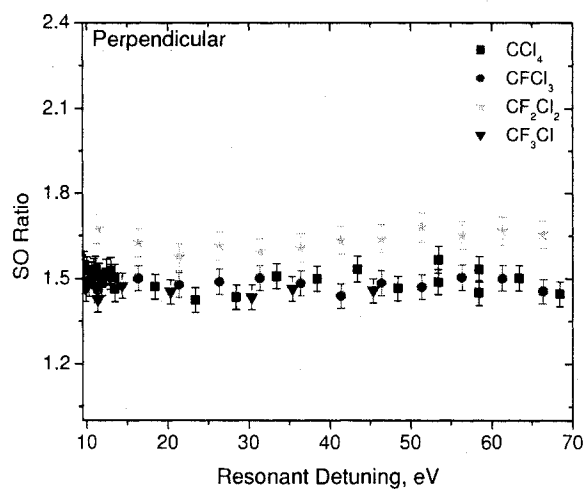
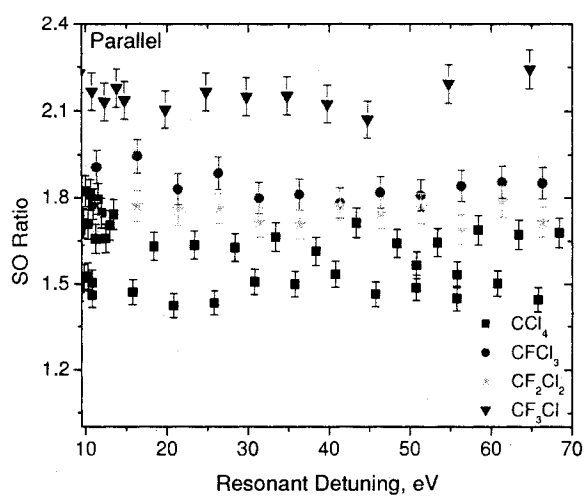


Figure 43. Measured spin-orbit ratios for all four molecules in both polarization directions when excitation is to the continuum.



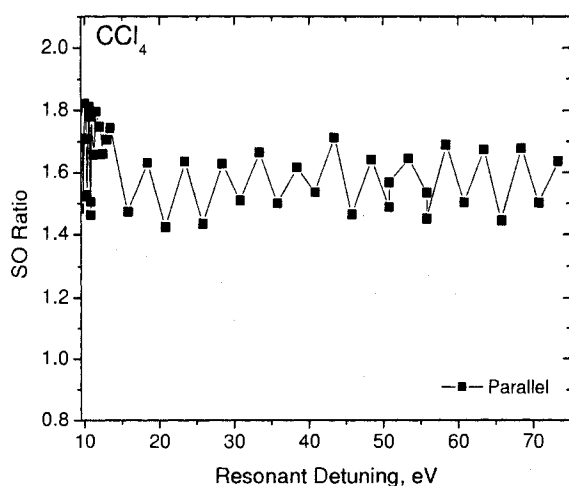


Figure 44. Oscillations of the SO ratios in  $\text{CCl}_4$  above the IP in the parallel orientation where the lines between data points were added to guide the eye.

Differences between molecules and deviations from the theoretical 2:1 must be attributed to molecular field effects in this energy range. Since the initial excitation is to the continuum, there are no resonant contributions and all differences in the SO ratio are due to the molecular field. Mixing of the  $2p$  states can be attributed to changes in ground-state symmetry above the IP [42]. The creation of a core-hole causes the outer electrons to rearrange to stabilize the core-hole. This rearrangement leads to changes in the equilibrium bond lengths and also differences in the bond angles. The changes in symmetry are dependent on the molecule from which they arise [42, 43, and 45] which is why we see such dramatic differences among the four molecules. Also seen in the other energy ranges,  $\text{CF}_3\text{Cl}$  has significant differences between the parallel and perpendicular directions (evident in Figure 43). Even in this energy range, where the molecular system is not aligned, the MF effects are larger in the parallel direction; supporting the claim that the MF coupling is stronger in the parallel direction. The oscillations in the parallel

direction in  $\text{CCl}_4$  could be explained by the MF “switching” from preferentially affecting the orbitals along the axis to the orbitals perpendicular. This would explain the upper SO ratios being constant around 1.7 and the lower SO ratios being constant around 1.5.

The final parameter in this section is the x-ray polarization ratio; see Figure 45. For all four molecules, the polarization ratio remains constant over the entire  $1s \rightarrow \infty$  range with  $\text{CCl}_4$  and  $\text{CF}_2\text{Cl}_2$  having the same polarization ratio of 1 (little polarization). The largest polarization ratio is seen in  $\text{CF}_3\text{Cl}$  at 2.0; which agrees well with Figure 43 where the largest SO ratio difference in parallel and perpendicular orientations was seen in  $\text{CF}_3\text{Cl}$ . Finally,  $\text{CFCl}_3$  has the lowest polarization ratio (0.5) and has a substantial polarization effect, as seen in Figure 43. The polarization ratios agree well with the MF effects in the SO ratio where  $\text{CF}_3\text{Cl}$  had the largest difference and  $\text{CF}_2\text{Cl}_2$  having little differences in the two polarization directions.

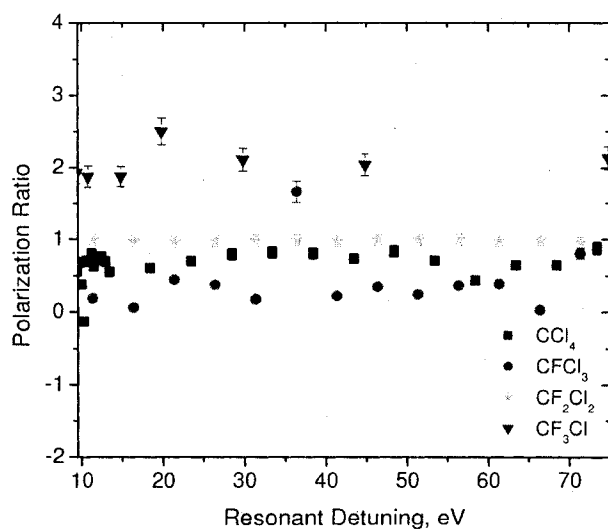


Figure 45. Polarization ratio versus incident photon energy for the  $1s \rightarrow \infty$  excitation.

## CHAPTER 6

### CHLORINE *K-V* RESULTS

Similar to the *K-L* data section, four data parameters will be discussed for  $\text{CF}_2\text{Cl}_2$ ,  $\text{CCl}_4$  and  $\text{CF}_3\text{Cl}$ ; peak widths, x-ray dispersion, peak ratios, and polarization. Since the molecular orbitals involved in the *K-V* x-ray emission are more complicated, a brief discussion of the empty and valence MO's will be presented. In this section, each molecule will be discussed separately with a brief comparison of all three molecules at the end of this chapter.

#### $\text{CF}_2\text{Cl}_2$

##### *K-V Valence Molecular Orbitals*

In this section, the initial absorption is the same as in the *K-L* data section; see Chapter 5, pages 67 - 70, but the emission in this energy range corresponds to the Cl  $3p \rightarrow 1s$  valence x-ray emission and only orbitals with Cl  $3p$  character contribute to the emission. The emission profile at this energy is more complicated than the *K-L* (where the six electrons contribute to two emission peaks) because the valence electrons are involved in bonding. The valence molecular orbitals (MOs) can be approximated using linear combinations of atomic orbitals (LCAO). In this picture, the atomic orbitals from chlorine, carbon, and fluorine combine to form MOs of different symmetries. In  $\text{C}_{2v}$  molecules such as  $\text{CF}_2\text{Cl}_2$ , the two C-Cl bonds point in different directions (although they

exist in the plane defined by the two Cl atoms and the C atom) and, using point group symmetry, MOs with  $a_1$  or  $b_2$  symmetry are symmetric about these two axes (z and y by definition) or more specifically, are symmetric about the Cl–C–Cl plane of symmetry (and the symmetry axis). See Appendix III for character tables to see how these orbitals change depending on the symmetry operation. For example, the  $9b_2$  MO (which contributes to the intensity of peak 1) is largely Cl  $3p$ , but also has contributions from the C  $2p$  and the F  $2p$ . MOs with  $a_2$  and  $b_1$  symmetry are oriented in a combination of directions, xy in  $a_2$  or x in  $b_1$  and are perpendicular, or not symmetric about the Cl–C–Cl plane of symmetry. Figure 46 shows the Cl  $K$ -V x-ray emission spectra of  $\text{CF}_2\text{Cl}_2$  at four incident energies; at 2823 eV (the  $1s \rightarrow 13a_1$ ,  $10b_2$  excitation), at 2827.2 eV (the  $1s \rightarrow 4p$  Rydberg), at 2829.1 eV (the  $1s \rightarrow np$  Rydberg) and at 2860 eV (far above the IP) where the parallel spectra have been smoothed using 5-point adjacent averaging to reduce the noise. Also, in Figure 26, the peak fits calculated in IGOR® are provided for the parallel direction.

As discussed in Chapter 3, pages 20 – 21, core levels undergo rapid Auger decay ( $10^{-14}$  s) so fluorescence is observed on a timescale much shorter than rotational time periods ( $10^{-11}$  to  $10^{-12}$  s) so any aligned system produced by the core hole is retained during the emission process. As an example, when the excitation is on top of the main absorption resonance ( $1s \rightarrow 13a_1$ ,  $10b_2$ ), the  $\text{CF}_2\text{Cl}_2$  molecules will be aligned with the Cl–C–Cl plane of symmetry (which includes the molecular symmetry axis) in the synchrotron radiation polarization direction. Emission from  $a_1$  and  $b_2$  orbitals will then have larger intensity in the parallel direction and those from  $b_1$  and  $a_2$  will be more intense in the perpendicular; allowing the orientation of MOs to be studied [4]. Polarization measurements can also

yield relative contributions in the emission spectra from MOs of different symmetry; specific examples of this will be seen in the following sections.

On the main resonance (2823 eV), there are four emission lines in the parallel orientation that are attributed to the  $12a_1$ ,  $3a_2$ ,  $6b_1$ ,  $7b_2$ , and  $8b_2$  molecular orbitals (peak 1), the  $11a_1$  and  $2a_2$  orbitals (peak 2) and the  $10a_1$ ,  $4b_1$ , and  $6b_2$  orbitals (peak 4) and peak 3 has not been assigned previously; the varying amounts of  $3p$  character associated with these orbitals is described in Chapter 3, pages 26 – 28. There are only two peaks present in the perpendicular spectrum, see Figure 46, as the two low energy peaks essentially disappear in the perpendicular direction. The initial excitation is to MO's that are symmetric about the Cl–C–Cl plane; peaks 2, 3, and 4 have significant intensity in the parallel direction and therefore contain significant amounts of  $a_1$  or  $b_2$  character. Since peak 1 has large intensity in both directions, it has contributions from orbitals in the Cl–C–Cl plane ( $a_1$  and  $b_2$ ) and perpendicular to it ( $b_1$  and  $a_2$ ). This can be seen from the MO assignment for peak 1 where it has contributions from all four types of orbitals.

Over the  $4p$  Rydberg, there are four peaks in the perpendicular (the low energy is weak and cannot be analyzed at this energy) and four in the parallel. On the  $np$  and above the IP, there are four peaks in both the parallel and the perpendicular orientations. Above the main resonance, the second peak appears as a shoulder to the main high-energy peak in both polarization directions. On the  $np$  Rydberg and far above the IP, there is a large tail in the perpendicular direction. A possible explanation for this is masking in the parallel direction from the crystal slit (where the crystal slit physically blocks the photons contributing to the tail); especially since this does not occur in the  $K$ - $L$  energy range or in argon.

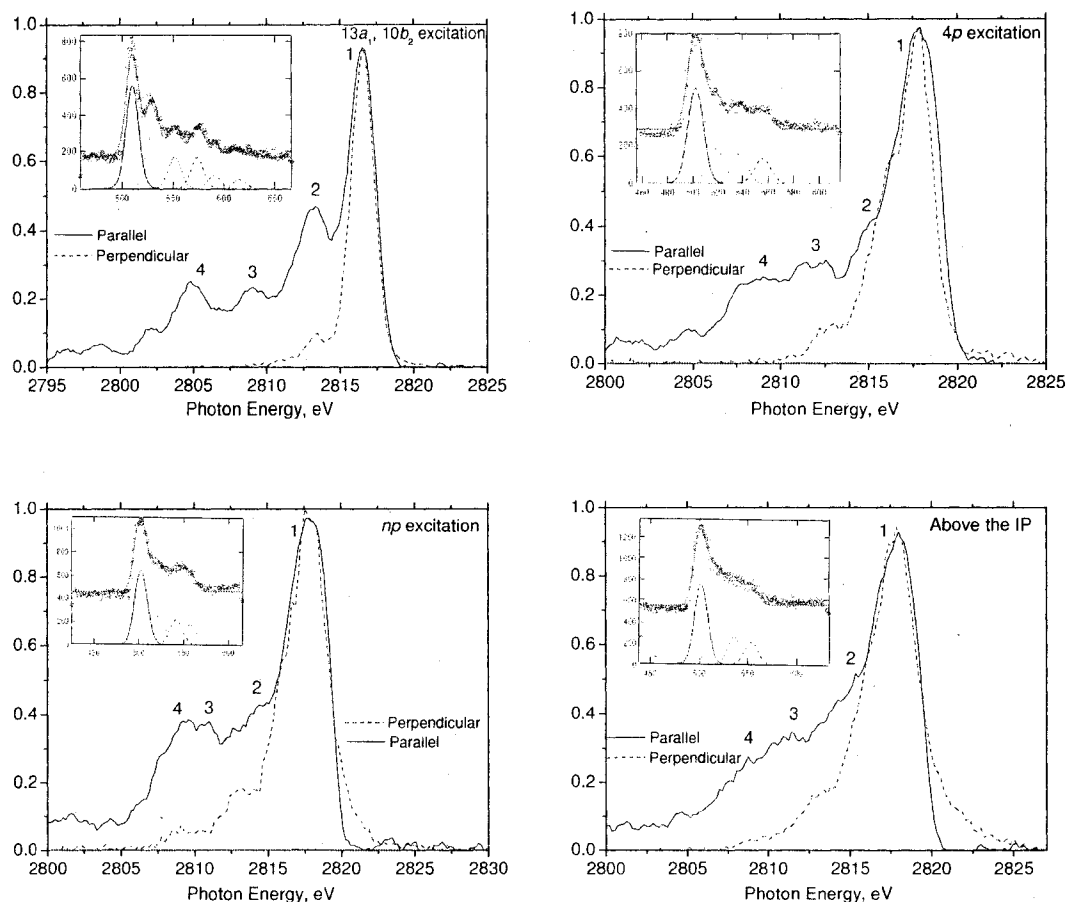


Figure 46. Measured Cl *K-V* x-ray emission from  $\text{CF}_2\text{Cl}_2$  at 2823 eV (the  $1s \rightarrow 13a_1, 10b_2$  excitation), at 2827.2 eV (the  $1s \rightarrow 4p$  Rydberg), at 2829.1 eV (the  $1s \rightarrow np$  Rydberg) and at 2860 eV (far above the IP), normalized to peak 1, with the peak-fitted spectra in the upper left. The peaks are reversed in the peak fit due to the geometry of the detector and are corrected during the energy calibration procedure.

### *Peak Widths*

The measured x-ray emission peak widths of peak 1 (defined in Figure 46) in both polarization directions over the main absorption resonance, over the  $4p$  resonance, and above the IP are shown in Figure 47. Over the main resonance, Figure 47, the peak widths fall in the predicted parabola-like distribution [15, 23, 24] with a minimum on top of the resonance; this is the same trend seen in the  $K$ - $L$  energy range. Over the  $4p$  resonance, Figure 47, there is also a decrease in peak width on top of the resonance (especially in the perpendicular direction) followed by a sharp decrease in the peak widths at the IP (2829.6 eV). Far above the IP, the peak widths remain essentially constant in both polarization directions; see Figure 47, with widths in the perpendicular direction being larger, 2.2 eV compared to 1.6 eV. The contribution to the increased peak widths in the perpendicular direction stem from the large high-energy tails. The peak widths would be comparable (as predicted by theory) if the crystal slit did not block the high-energy contributions in the parallel direction.

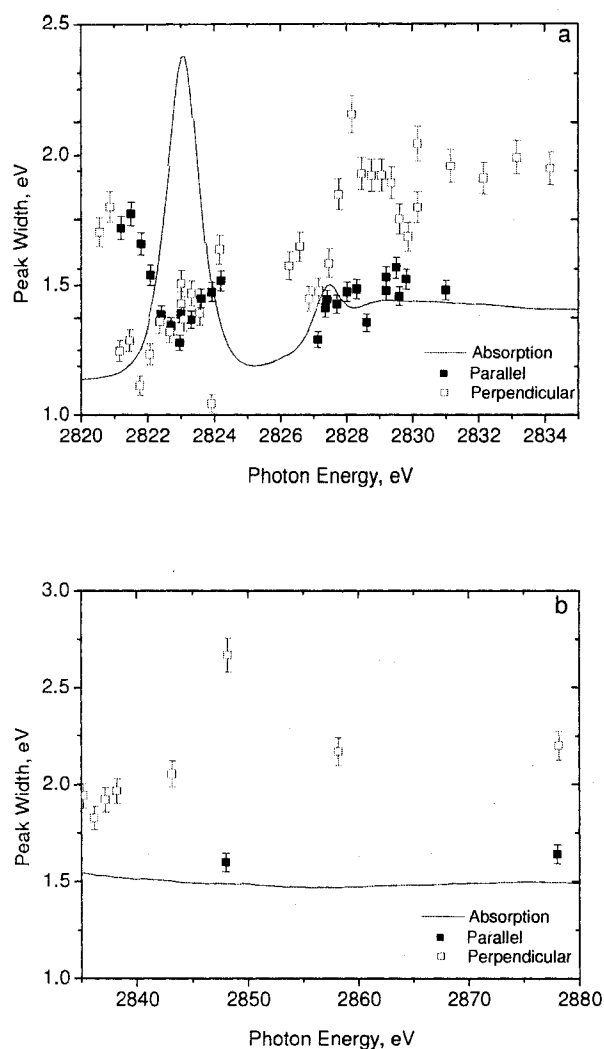


Figure 47. Measured Cl *K-V* x-ray peak widths from  $\text{CF}_2\text{Cl}_2$  in the parallel and perpendicular orientations plotted with the absorption spectrum at (top) 2820 – 2835 eV and (bottom) 2835 – 2880 eV.

### *Dispersion*

The measured x-ray dispersion of peak 1 is plotted against incident photon energy over the main absorption resonance (LUMO), over the *4p* Rydberg, and far above the IP in Figure 48. Over the main resonance, the dispersion has the same non-linear shape that



was seen in the *K-L* energy range (although it is less pronounced) and can also be explained with equation 18; this was also seen in the *K-V* data in HCl [15]. The peak energy on top of the resonance is 1.5 eV lower than the values measured above the IP (2815 eV versus 2816.5 eV); there is significant screening occurring on the  $1s \rightarrow 13a_1$ ,  $10b_2$  resonance as was seen by Lindle et al [30]. The degree of screening is dependent on the molecule (and the MOs involved in emission) because the promoted electron (and the core hole) causes a rearrangement of the electron cloud. Molecular orbitals that occupy the same space as the promoted electron (and the core hole) are more affected and show the largest energy shifts. This effect was not observed in the *K-L* data.

Over the  $4p$  Rydberg, Figure 48, there is a linear increase of peak position with photon energy (as was seen in the *K-L* data) to a value of 2816.3 eV on the top of the resonance; this value is 0.2 eV smaller than the value above the IP. As shown by Agren and Gel'mukhanov, the screening effects on the Rydberg states in  $\text{CF}_2\text{Cl}_2$  are small, due to the decreased overlap of the  $4p$  Rydberg and the core-hole and because the promoted electron is to states of mixed symmetry. These screening effects are on the same order of magnitude as those observed in the  $\text{H}_2\text{O}$  and  $\text{CO}$  Rydberg states [33]. The dispersion then remains essentially constant over the  $np$  resonance at 2816.5 eV with only slight fluctuations. After the IP, Figure 48, the peak positions are constant in both directions and close to 2816.5 eV and are the values measure by Lindle et al [30].

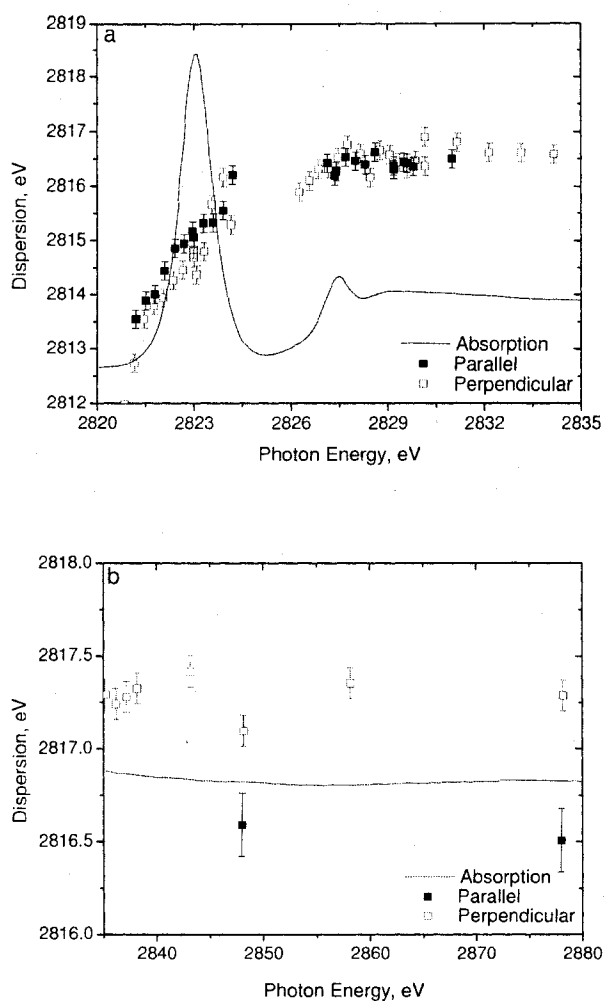


Figure 48. Measured Cl *K-V* x-ray dispersion of peak 1 in  $\text{CF}_2\text{Cl}_2$  in the parallel (solid) and perpendicular (empty) from (top) 2820 – 2835 eV and (bottom) 2835 – 2880 eV plotted with the absorption spectrum (line).

The dispersion trends in peaks 2 – 4 are similar to those seen in peak 1; see Figure 48a. Over the main resonance, the non-linear dispersion is more dramatic for peaks 3 and 4; this is a 3 eV increase over the resonance for peak 1 versus a 5 eV increase for peaks 3 and 4. Dispersion differences among the four emission peaks can be attributed to screening effects; which can be described by examining the molecular orbitals

contributing to the emission. Since the initial excitation is to orbitals of  $a_1$  or  $b_2$  symmetry, emission from orbitals of the same symmetry have more overlap with the core-hole and therefore, have larger screening contributions. Peaks 3 and 4 are largely composed of orbitals of  $a_1$  and  $b_2$  symmetry so the screening effects will be dramatic ( $a_1$  orbitals occupy the same regions of the molecule so valence MOs of  $a_1$  symmetry will interact more with the promoted electron and the core-hole). Peaks 1 and 2 have less (but still significant) screening effects because they have contributions from orbitals of different symmetry ( $a_2$  and  $b_1$  in peak 1 and  $a_2$  in peak 2). There is still significant overlap from the other orbital contributions of  $a_1$  symmetry but this is expected to be less dramatic due to the perpendicular MOs that also contribute. The four peaks have similar distributions over the  $4p$  Rydberg and far above the IP where the overlap with the core-hole is diminished.

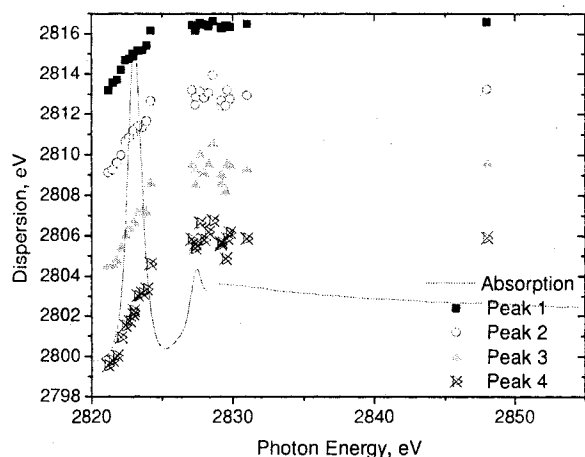


Figure 48a. Measured Cl x-ray dispersion of all four emission peaks over the  $K$ - $V$  energy range (error bars are omitted for comparison but are the same as in Figure 48) in  $\text{CF}_2\text{Cl}_2$ .

### Peak Ratios

The orbitals in the  $K$ - $V$  x-ray emission are involved in molecular bonding and are delocalized over the entire molecule according to the symmetry of the point group. Because of this, the spin orbit ratio is not a valid parameter since the orbitals involved have chlorine  $3p$  character and some character from the chlorine  $3s$ , fluorine  $2p$ , and carbon  $2p$  orbitals (also the SO splitting of Cl  $3p$  is small  $\sim 0.2$  eV and cannot be resolved). A more valid parameter will be the peak ratios; namely the ratio of peaks 2, 3, and 4 to that of peak 1 defined as  $R_{21}$ ,  $R_{31}$ , and  $R_{41}$ , respectively.

Figure 49 shows the peak ratios over the main absorption resonance and the Rydberg states in the parallel and perpendicular directions. In the parallel orientation,  $R_{21}$  shows a slow increase with increasing photon energy over the main resonance; meaning the intensity of peak 2 relative to peak 1 is changing very little over the resonance.  $R_{31}$  and  $R_{41}$  are the same over the resonance, where they have a U shaped distribution over the main resonance with a minimum close to the resonance maximum; Figure 49 (a). The ratios in the perpendicular direction are changing much more drastically over the main resonance, Figure 49 (b).  $R_{21}$  is steadily decreasing on the low-energy side of the resonance and then remains constant over the top and on the high-energy side.  $R_{31}$  and  $R_{41}$  are very small over the energy range (indicating very large differences between peak 1 and peaks 3 and 4). From examining these trends, one can expect large polarization effects over the main resonance (these will be examined in the next section).

Over the first resonance, the largest difference is seen in the parallel direction between peaks 3 and 4 and peak 1. Peak 3 and peak 4 have similar orbital makeup and are oriented largely in the parallel direction (with significant  $a_1$  and  $b_2$  character), as the

ratios are essentially zero in the perpendicular direction. Peak 2 also contains a large amount of  $a_1$  character as the ratio between peak 2 and peak 1 also decreases dramatically in the perpendicular direction.

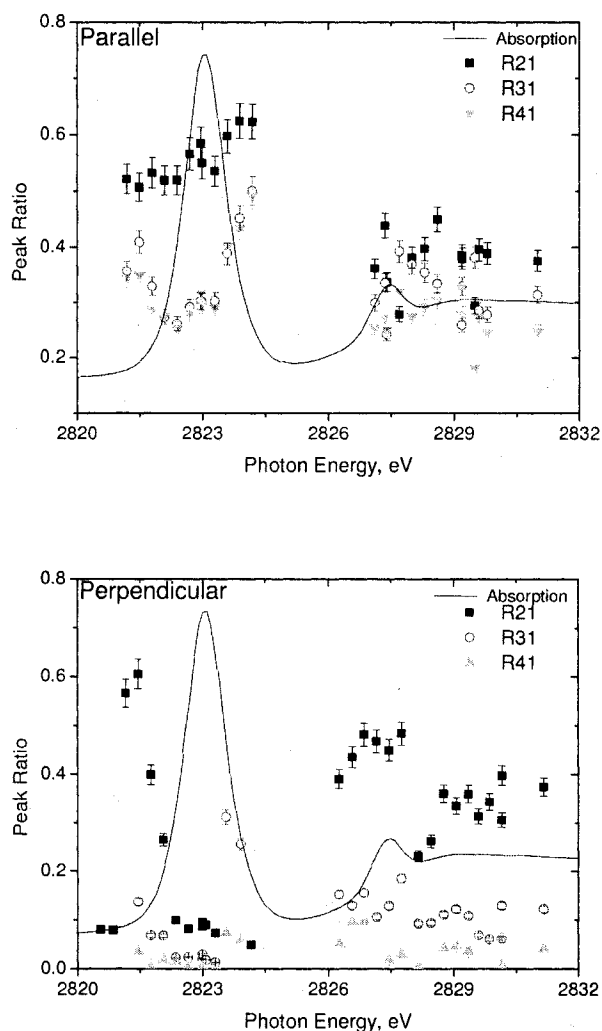


Figure 49. Measured Cl  $K$ - $V$  peak ratios of  $\text{CF}_2\text{Cl}_2$  in the parallel (top) and perpendicular (bottom) orientations plotted with the absorption spectrum (line) over the main resonance and the Rydberg states.

Over the  $4p$  Rydberg and close to the IP, the peak ratios in the parallel direction are fluctuating rapidly; see Figure 49. In this direction,  $R_{21}$  is the largest followed by  $R_{31}$  followed by  $R_{41}$ . The ratios are changing dramatically at this energy and indicate that polarization is not the only effect and nondipole effects could be significant (explained in detail with the peak ratios above the IP). In the perpendicular direction,  $R_{21}$  increases over the  $4p$  and the  $np$  Rydbergs then remains constant past the IP while  $R_{31}$  and  $R_{41}$  have similar dispersions in this range as they both increase over the  $4p$  Rydberg and then remain constant close to the IP.

Comparing parallel and perpendicular directions over the Rydberg states further confirms that both peak 3 and peak 4 have significant  $a_1$  and  $b_2$  character; as there are significant differences between the parallel and the perpendicular directions. Also, peak 1 has a mixture of molecular orbital contributions (as there is significant intensity in both directions). Differences in peak 3 and peak 4 at this energy range result from excitations to  $p$  orbitals along the C–Cl bonds or  $p$  orbitals perpendicular to the axes. Peaks with MO's that contain  $a_1$  and  $b_2$  symmetry ( $z$  and  $y$  directions along a C–Cl axis) will also show differences in the perpendicular direction compared to orbitals of  $b_1$  symmetry ( $x$ -direction, perpendicular to both C–Cl bond axes). As seen in Figure 49,  $R_{41}$  is essentially zero while  $R_{31} \neq 0$  so peak 3 has more contribution from orbitals of  $b_1$  symmetry compared to peak 4. While both peaks contain significant amounts of  $a_1$  and  $b_2$  character (as the ratios are still small), peak 3 also has some contributions from orbitals of  $b_1$  character as  $R_{31}$  is larger than  $R_{41}$ .

Far above the IP, the peak ratios are constant for all peaks and for both polarizations; see Figure 50. In both polarization directions,  $R_{21}$  is the largest followed by  $R_{31}$  and then

$R_{41}$ . Although the x-ray emission is predicted to be isotropic at this energy (because the system is not aligned) [4, 30], there are differences in the two polarization directions that have not been seen before;  $R_{31}$  and  $R_{41}$  are much larger in the parallel direction. Also, as seen from Figures 46 and 50, peak 4 disappears in the perpendicular direction even at energies far above the IP while it has significant intensity in the parallel direction. Possible explanations will be presented in the next section (polarization).

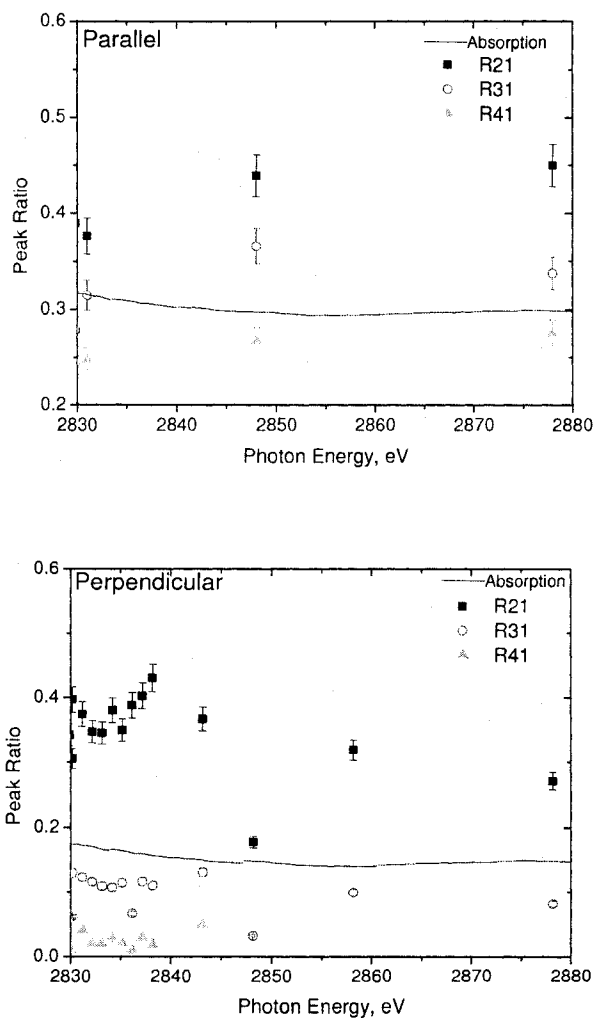


Figure 50. Cl K-V peak ratios of  $\text{CF}_2\text{Cl}_2$  in the parallel (top) and the perpendicular (bottom) polarization directions above the IP plotted with the absorption spectrum (line).

### *Polarization*

The relative polarization of each of the four x-ray emission peaks at the  $K$ - $V$  energy range is plotted against the incident photon energy (Figure 51), where polarization was defined in Chapter 4, page 89 and is the measure of the relative difference between the parallel and the perpendicular orientations (with a maximum value of 1, and a minimum of  $-1$  where 1 and  $-1$  represent significant polarization effects and 0 represents zero polarization effects). Although only the relative polarization values are given and no conclusions can be drawn about the values themselves, the differences between the four peaks can still be assessed by examining the trends in the polarization values.

Over the main resonance, Figure 51, peak 1 has a negative polarization (the intensity in the perpendicular direction is greater than the intensity in the parallel); with decreasing polarization values over the top of the resonance. Since the polarization value is negative, peak 1 has greater intensity in the perpendicular direction. Peak 2 has a negative polarization far below the top of the resonance and a positive polarization over the top of the resonance and on the high-energy side of the resonance; indicating it has mixed MO contributions. The polarization of peak 3 increases on the low-energy side of the resonance and remains close to 1 over the top of the resonance and on the high-energy side. Peak 4 shows the same dispersion as peak 3, remaining positive and close to one. The large positive polarization values for peaks 3 and 4 indicate they have large MO contributions in the parallel direction. This trend in polarization over the main resonance agrees well with Figure 46 where peaks 2, 3, and 4 (which have large contributions from MOs of  $a_1$  symmetry) are much more intense in the parallel orientation compared to the perpendicular.



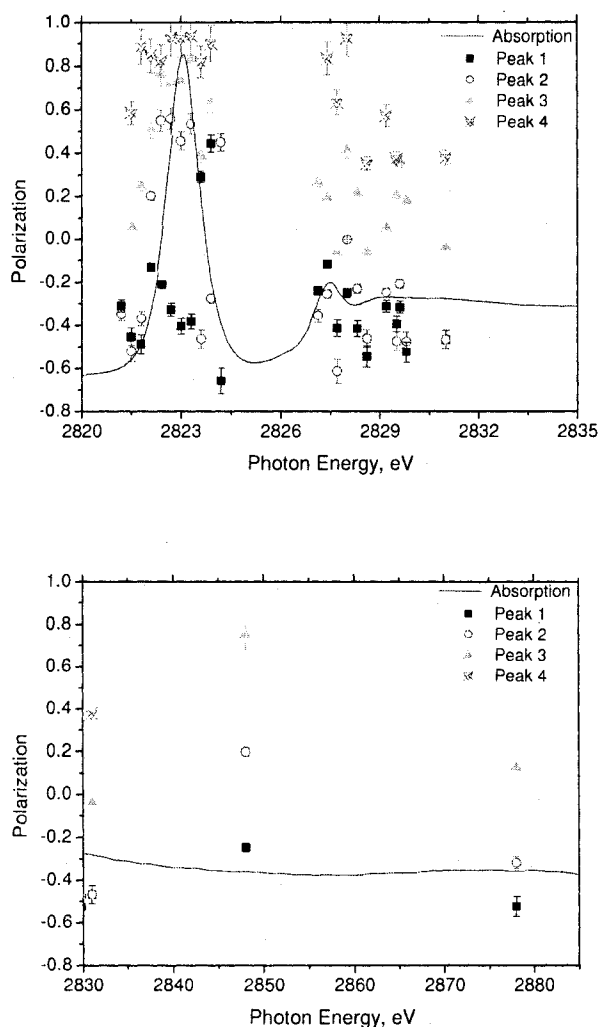


Figure 51. Cl K-V polarization plots for  $\text{CF}_2\text{Cl}_2$  of each of the four emission peaks from (top) 2820 – 2835 eV and (bottom) 2830 – 2885 eV plotted with the absorption spectrum (line).

The polarization of peak 1 shows small changes over the main resonance. This also supports that peak 1 has contributions from MOs symmetric about the Cl–C–Cl plane ( $a_1$  and  $b_2$  MOs) and from MOs perpendicular ( $b_1$ ). Peak 1 has polarization values close to zero, suggesting small differences between parallel and perpendicular directions (or a

mixture of MOs with parallel and perpendicular symmetry). The polarization of peaks 2, 3, and 4 are essentially the same (and quite significant) approaching a maximum value for the polarization (1) also supporting that they have large contributions from MOs of parallel (symmetric about the Cl–C–Cl plane) symmetry ( $a_1$  and  $b_2$ ). These results agree with previous measurements made on  $\text{CF}_2\text{Cl}_2$  [30]

Over the  $4p$  resonance, the polarizations of the four peaks cluster into two groups; negative values (peak 1 and peak 2) and positive values (peak 3 and peak 4); indicating peaks 1 and 2 have contributions from MO's perpendicular to the symmetry axis while peaks 3 and 4 have contributions from MO's along the axis. Peak 4, however, has a larger polarization effect than peak 3. This is because peak 3 has larger contributions from MO's of  $b_1$  (perpendicular) symmetry. Far above the IP, there are large differences among the three peaks (anisotropy).

Because of experimental differences, the polarization ratio is a valuable tool to compare the polarization changes of one peak to another, since taking the ratio eliminates any experimental effects, specifically the difference in counting times, solid angle, and detector efficiency. Figure 52 shows the polarization ratios of peak 1 to peak 2, peak 1 to peak 3 and peak 1 to peak 4 over the first resonance and the Rydberg states. Over the top of the main resonance, the polarization ratios are the same for all four peaks. This supports the molecular orbital assignments where peaks 2, 3, and 4 have MO's that are symmetric about the C–Cl axis and that peaks 1 and 2 have contributions from MO's perpendicular to the axis.

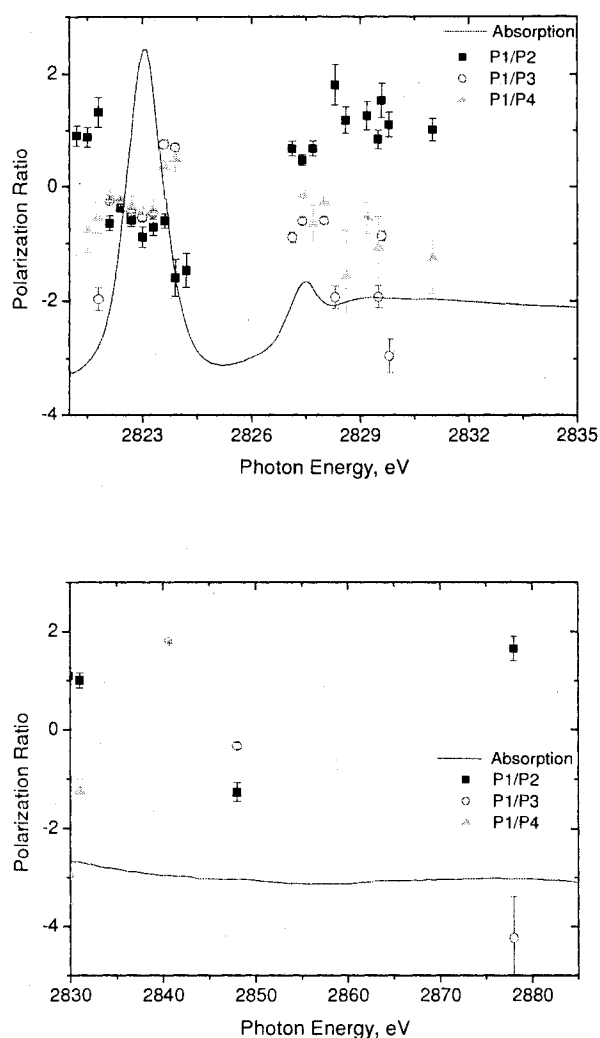


Figure 52. Cl K-V polarization ratios from  $\text{CF}_2\text{Cl}_2$  over the first absorption resonance and the Rydberg states (top) and above the IP (bottom) with the absorption spectrum (line).

Over the  $4p$  and  $np$  Rydbergs and far above the IP, the polarization ratio of peak 1 to peak 2 remains close to 1 with small fluctuations around the  $np$  Rydberg; suggesting the polarizations of peaks 1 and 2 are similar at this energy range (which was seen in the polarization plots). The ratios of peaks 1 and 3 and peaks 1 and 4 are negative and decrease with increasing photon energy. This means the polarizations of peak 1 and

peaks 3 and 4 are quite different over this energy range, yielding ratios vastly different from 1. Far above the IP there is a vast difference between the polarization ratio of peak 1 and peak 2 (2.0) and peak 1 and peak 3 (−4.0) suggesting the emission at this energy is anisotropic. This anisotropy is reported here for the first time.

Previously, x-ray emission at high photon energies was observed to be isotropic, as measured in  $\text{CH}_3\text{Cl}$  and predicted for  $\text{CF}_3\text{Cl}$  [4, 30]. Polarization differences above the IP observed at the  $K$ - $V$  energy range can be attributed to nondipole effects; Chapter 3, page 34. These effects are bond-length dependent, as in diatomic molecules, or depend on the separation of Cl atoms in polyatomic molecules; which makes  $\text{CF}_2\text{Cl}_2$  a good candidate since the two Cl atoms are sufficiently separated. The small excitation wavelength and large internuclear separation of the Cl atoms render the dipole approximation invalid and phase variations over the molecule become significant [40]. These variations can lead to vibronic coupling, as seen in  $\text{CO}_2$  [38]. In this scheme, near degenerate core-excited states (i.e. the two  $1s$  orbitals of the Cl atoms) can couple in the core-excited state via antisymmetric vibrational modes [38, 62]. The coupling occurs in the antisymmetric mode because the Cl  $1s$  belong to MO's of different symmetries. This coupling opens up decay channels that otherwise would not be seen (like the ungerade→ungerade transition seen in  $\text{Cl}_2$  [40], or nondipole transitions since they are not seen without the coupling). Opening these channels would account for the differences observed in the peak ratios (and polarization) in the parallel and the perpendicular directions. The nondipole effects are expected to be larger in the parallel direction where the coupling is between the  $a_1$  and  $b_2$  MO's (the orbitals where  $1s$  electrons reside) and maximum emission intensity is in the parallel direction. Nondipole

effects are possible below the IP, and could explain the differences seen over the Rydberg states, but not as evident because the polarization effects are large.

### *Bonus Peak*

At three incident photon energies on the low energy side of the  $4p$  resonance (close to the 2<sup>nd</sup> molecular resonance), a bonus high-energy peak appears in the perpendicular orientation at 2819.2 eV, see Figure 53. At the lower photon energy, 2826.18 eV, the peak is the most intense and as the photon energy is increase, the bonus peak decreases in intensity until it disappears close to the  $4p$  Rydberg. This high-energy peak appears due to vibrational excitation of the intermediate and final states. In this case,  $v_0 \neq v_i$  but  $v_i = v_f$  where 0, i, f, are the ground, intermediate, and final states and the difference in energy between the main emission peak and the bonus peak is the difference in vibrational energies.

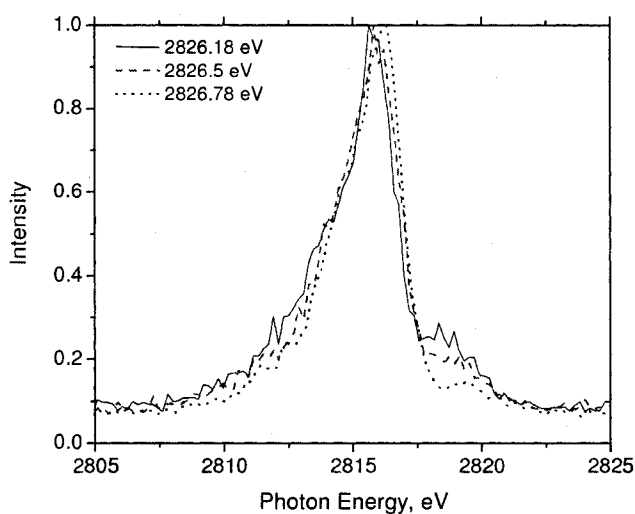


Figure 53. Cl K-V x-ray emission spectra of  $\text{CF}_2\text{Cl}_2$  at 2826.18 eV (line), 2826.5 eV (dash) and at 2826.78 (dots).

## CCl<sub>4</sub>

### *K-V Valence Molecular Orbitals*

In this molecule, only data at six different incident energies were collected (due to time constraints); thus rendering it difficult to draw any major conclusions. The initial absorption for CCl<sub>4</sub> is the same as in the *K-L* data section; see Chapter 5, pages 67 – 70. Figure 54 shows the Cl *K-V* x-ray emission spectra for CCl<sub>4</sub> at four incident energies, at 2822.5 eV (the  $1s \rightarrow 7a_1, 8t_2$  excitation), at 2827.35 eV (the  $1s \rightarrow 4p$  Rydberg), at 2830.65 eV (the  $1s \rightarrow np$  Rydberg) and at 2860 eV (far above the IP). On the main resonance (2822.5 eV), there are four emission lines in the parallel orientation; one very broad feature, with contributions from peaks 2 and 3, and two narrow, peaks 1 and 4. There are only two emission peaks in the perpendicular and, similar to CF<sub>2</sub>Cl<sub>2</sub>, the low energy peaks essentially disappear in the perpendicular direction. Peak 1 is comprised of the  $2t_1, 7t_2$ , and  $2e \rightarrow 1a_1, 1t_2$  transitions, peak 2 is the  $6t_2 \rightarrow 1a_1, 1t_2$  transition, peak 3 is the  $6a_1 \rightarrow 1a_1, 1t_2$  transition and peak 4 is the  $5t_2 \rightarrow 1a_1, 1t_2$  transition [66, 67]. From the peak assignments, peak 1 has contributions from MO's symmetric about the four C–Cl axes ( $t_2$ ) and from MO's perpendicular to it ( $t_1, e$ ) and therefore has significant intensity in both directions. Peaks 2, 3, and 4 are composed of MO's that are symmetric about the axes ( $a_1, t_2$ ) and have little intensity in the perpendicular direction (as seen from Figure 54). On the  $4p$  Rydberg, there are three peaks in the perpendicular and four in the parallel; two narrow and one large, broad peak (with contributions from peaks 2 and 3). The same is true on the  $np$  Rydberg and far above the IP.

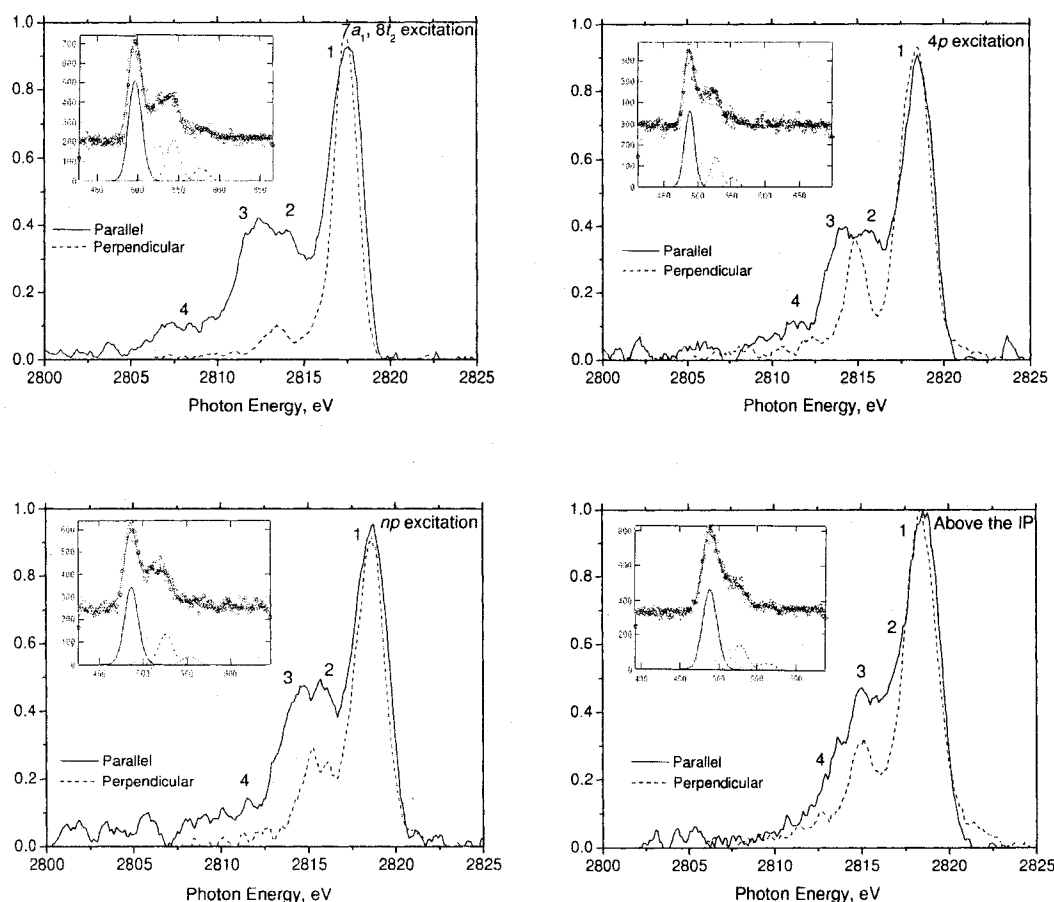


Figure 54. Measured  $K$ -V x-ray emission from  $\text{CCl}_4$  at 2822.5 eV (the  $1s \rightarrow 7a_1, 8t_2$  excitation), at 2827.35 eV (the  $1s \rightarrow 4p$  Rydberg), at 2830.65 eV (the  $1s \rightarrow np$  Rydberg) and at 2860 eV (far above the IP) with the curve fitting in the upper right corner.

### Peak Widths

The measured x-ray peak widths of peak 1 in  $\text{CCl}_4$  in the parallel and perpendicular orientations are plotted in Figure 55. Over the entire energy range (2820 – 2860 eV) the peak widths in the parallel and perpendicular orientations are the same except on the main resonance where the parallel spectrum has a width of 2.2 eV while it is 1.5 eV in the perpendicular direction; we attribute this discrepancy to experimental uncertainty because

of insufficient counting time. The widths on the  $np$  Rydberg, on the IP, and far above the IP are all the same in both directions, having a width of 2.1. The peak widths are smaller on the resonances (compared to above the IP); which agrees well with  $\text{CF}_2\text{Cl}_2$  and theory [23].

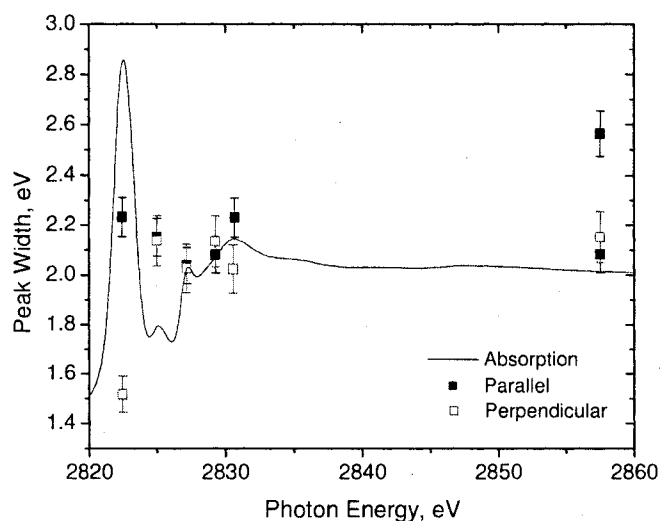


Figure 55. Measured Cl  $K$ - $V$  peak widths of  $\text{CCl}_4$  in the parallel (solid) and perpendicular (empty) orientations plotted with the absorption spectrum (line).

### Dispersion

Similar to the effects seen in the  $K$ - $V$  x-ray dispersion of  $\text{CF}_2\text{Cl}_2$ , the energy of peak 1 on the main resonance is 1.0 eV lower than the energy far above the IP; see Figure 56. The peak energies increase with increasing photon energy over the main resonance, the 2<sup>nd</sup> molecular resonance, the  $4p$  Rydberg, where they level off and remain constant over the  $np$  Rydberg, across the IP and far above the IP. Similar to the effect seen in  $\text{CF}_2\text{Cl}_2$ , there is significant screening on the main resonance (a  $-1.0$  eV energy difference) and minor screening effects seen on the Rydbergs (a  $+0.1$  eV energy difference on the  $4p$



Rydberg). Just as in  $\text{CF}_2\text{Cl}_2$ , peaks 2, 3, and 4 are expected to have larger screening effects, as there is greater overlap of  $a_1$  and  $t_2$  orbitals with the core-hole. Although there is not sufficient data over the main resonance, the dispersion is predicted to obey equation 18 [15].

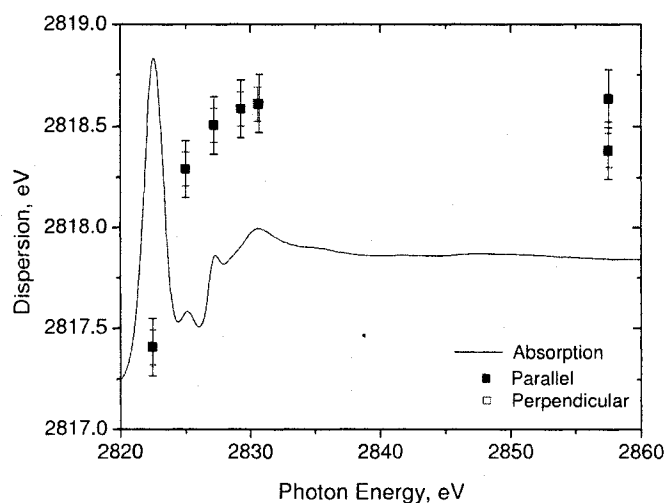


Figure 56. Measured K-V x-ray dispersion of  $\text{CCl}_4$  in the parallel (solid) and perpendicular (empty) plotted with the absorption spectrum (line).

### Peak Ratios

The x-ray peak ratios are plotted in Figure 57 for the parallel and perpendicular orientations. In the parallel and the perpendicular directions,  $R_{21}$  remains constant over the entire energy range (2820 – 2860 eV) with the ratio in the parallel direction being larger than that in the perpendicular. In the parallel direction,  $R_{31}$  is similar to that of  $R_{21}$  except on the  $np$  resonance where it is significantly smaller.  $R_{31}$  is small over the entire energy range in the perpendicular direction. Similar to the effect seen in  $\text{CF}_2\text{Cl}_2$ , there

are large differences in the peak ratios between the parallel and the perpendicular directions.

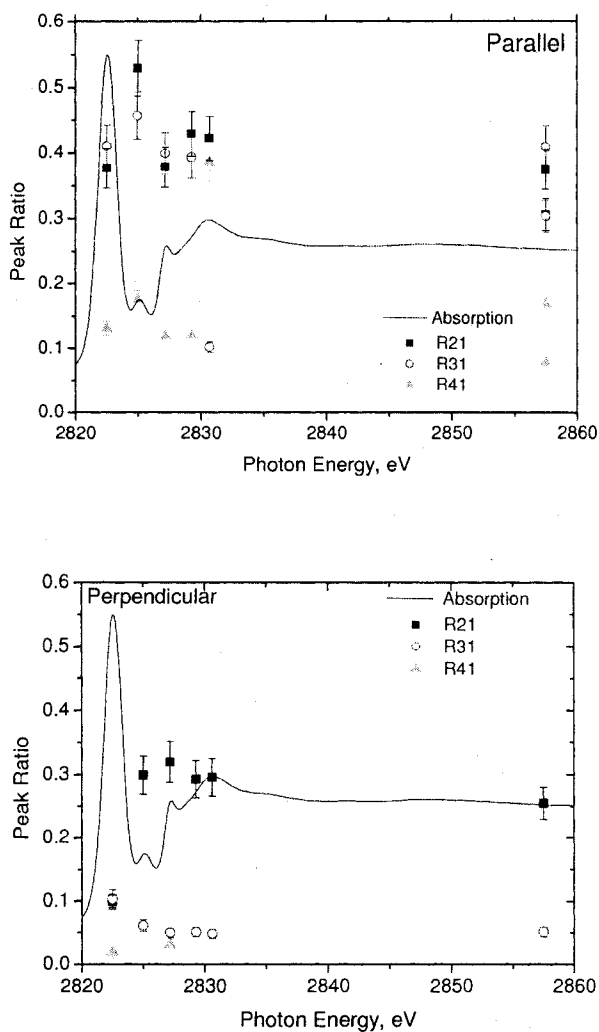


Figure 57. Measured  $K$ - $V$  peak ratios of  $\text{CCl}_4$  in the parallel (top) and perpendicular (bottom) orientations plotted with the absorption spectrum (line).

Differences in these ratios are due to polarization effects; peak 1 has contributions from MO's that are symmetric about the C-Cl axes ( $a_1$ ) as well as from MOs that are perpendicular ( $t_1, e$ ); while peaks 2 – 4 are composed of MOs in the parallel direction ( $a_1$

and  $t_2$ ), as seen by the drastic decrease in all peak ratios (especially peaks 3 and 4) in the perpendicular direction. Also, differences between the two orientations can be attributed to nondipole effects (as there is a large difference in polarization directions above the IP where the emission was presumed to be isotropic). A further discussion will be presented in the polarization section.

### *Polarization*

In  $\text{CCl}_4$  in the  $K$ - $V$  energy range, the relative polarization of peak 1 is increasing with increasing photon energy from the main resonance, over the 2<sup>nd</sup> molecular resonance, over the 4 $p$  Rydberg, the  $np$  Rydberg and the IP but always remains negative; see Figure 58. As the photon energy is tuned away from the molecular resonances and to the less symmetric atomic-like Rydbergs, the polarization effects decrease. The polarization of peak 2 is decreasing with photon energy over the main resonance, the 2<sup>nd</sup> molecular resonance and the 4 $p$  Rydberg (indicating there are large contributions from MO's symmetric about the C-Cl bonds) and increases over the  $np$  but also remains negative over the entire energy range. The negative polarization indicates there is more intensity in the perpendicular direction; most of the contributions to peak 1 are from the  $t_1$  and  $e$  orbitals. Like peak 1, peak 3 is increasing over the entire energy range but has large positive polarization values. Peak 3 shows the largest polarization effects (the same as was seen in  $\text{CF}_2\text{Cl}_2$ ) as it disappears in the perpendicular direction at some energies. Peaks 3 and 4 are expected to be composed of MO's that are  $a_1$  and  $t_2$  in character as the polarizations are large and approach 1. Far above the IP, peak 1 and peak 2 remain negative while peak 3 remains positive. This large difference in polarization far above the IP is tentatively attributed to nondipole effects. Just as in  $\text{CF}_2\text{Cl}_2$ , vibronic coupling

is lifting the degeneracy of near identical states (and  $\text{CCl}_4$  has two more than  $\text{CF}_2\text{Cl}_2$ ).

This coupling can open decay channels usually not accessible in normal dipole emission.

This effect is large in  $\text{CCl}_4$  as the polarization of peak 3 is much larger than that of peaks 1 and 2.

The polarization ratios of peak 1 to peak 2 lie in a similar distribution compared to the polarization values of peak 2. However, since the polarizations of peak 1 and peak 2 are both negative, the ratio is positive; see Figure 58. The polarization ratio of peak 1 to peak 3 is large and positive on resonance, and then remains small and negative over the rest of the energy range. Far above the IP, the polarization ratio of peak 1 to peak 2 is 1.5 while that of peak 1 to peak 3 is  $-1.0$ ; indicating there is anisotropy at this energy range; similar to that seen in  $\text{CF}_2\text{Cl}_2$ . The polarization ratios of peak 1 to peak 2 and of peak 1 to peak 3 are of different sign far above the IP. This indicates the nondipole effects in  $\text{CCl}_4$  are quite significant; which can be expected as  $\text{CCl}_4$  has twice as many Cl atoms as  $\text{CF}_2\text{Cl}_2$ . This means there are four near degenerate states that can be lifted due to the vibronic coupling (4 Cl  $1s$  core orbitals in  $\text{CCl}_4$  versus 2 in  $\text{CF}_2\text{Cl}_2$ ). Because coupling can occur with two or more near degenerate states, the nondipole effects should be greater (or more otherwise forbidden channels can be opened). This explains why there are larger effects seen in  $\text{CCl}_4$  above the IP. It is expected the coupling mechanism for nondipole effects is the same in both molecules.

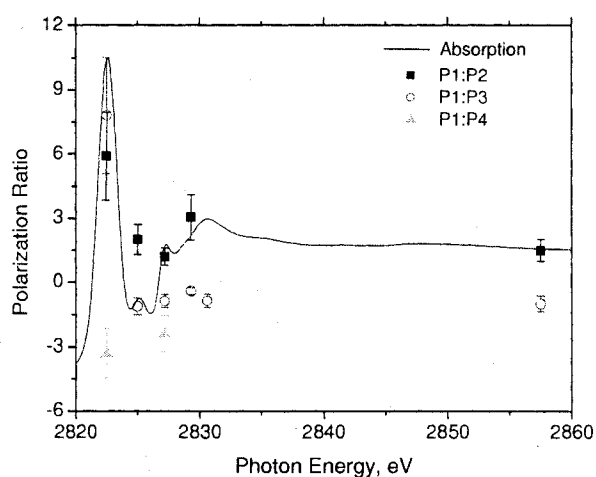
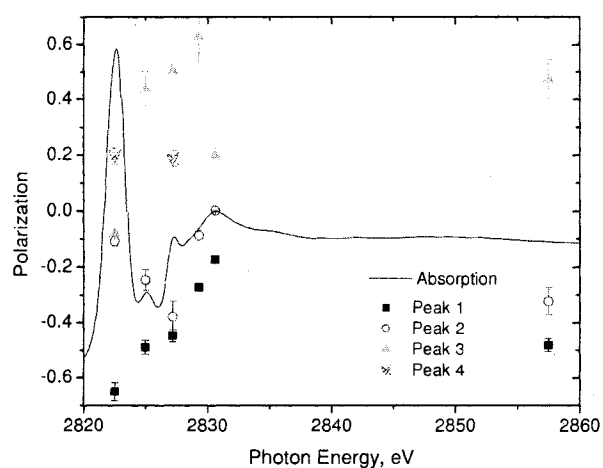


Figure 58. Cl *K-V* polarization (top) and polarization ratio (bottom) of  $\text{CCl}_4$  from 2820 – 2860 eV with the absorption spectrum (line).



*K-V Valence Molecular Orbitals*

The previous molecules in this energy range ( $\text{CF}_2\text{Cl}_2$  and  $\text{CCl}_4$ ) contain multiple chlorine atoms;  $\text{CF}_3\text{Cl}$  is unique because it is the only molecule with only one chlorine atom. Because of this,  $\text{CF}_3\text{Cl}$  can be considered a pseudo diatomic molecule (C–Cl) and

treated with a simple classical picture. The initial absorption for  $\text{CF}_3\text{Cl}$  is the same as in the *K-L* data section; see Chapter 5, pages 67 – 70. Figure 59 shows the Cl *K-V* x-ray emission spectra at four incident energies, at 2823.5 eV (the  $1s \rightarrow 11a_1$  excitation), at 2827.8 eV (the  $1s \rightarrow 4p$  Rydberg), at 2829.2 eV (the  $1s \rightarrow np$  Rydberg) and at 2855 eV (far above the IP). On the main resonance (2823.5 eV), there are four emission lines in the parallel orientation; one broad and three narrow, and only three in the perpendicular; like the other two molecules, the low energy peak essentially disappears in the perpendicular direction. Peak 1 has been assigned to the  $7e \rightarrow 1a_1$  transitions, peak 2 to the  $10a_1, 5e \rightarrow 1a_1$  transition and peak 3 to the  $4e, 9a_1 \rightarrow 1a_1$  transition. Just as in  $\text{CF}_2\text{Cl}_2$  and  $\text{CCl}_4$ , peak 1 is largely comprised of a MO that is perpendicular to the C–Cl bond axis (*e*), which is also the symmetry axis, while peaks 2, 3, and 4 are largely MO's symmetric about the symmetry axis (*a<sub>1</sub>*). On the *4p* Rydberg, there are three peaks in the parallel; two narrow and one broad, and three peaks in the perpendicular (peak 4 is very weak and not analyzed). The same is true on the *np* Rydberg and far above the IP. However, at these higher energies, there is statistically no difference between the parallel and the perpendicular orientations and the x-ray emission is largely isotropic (this will be discussed in further detail in the following sections).

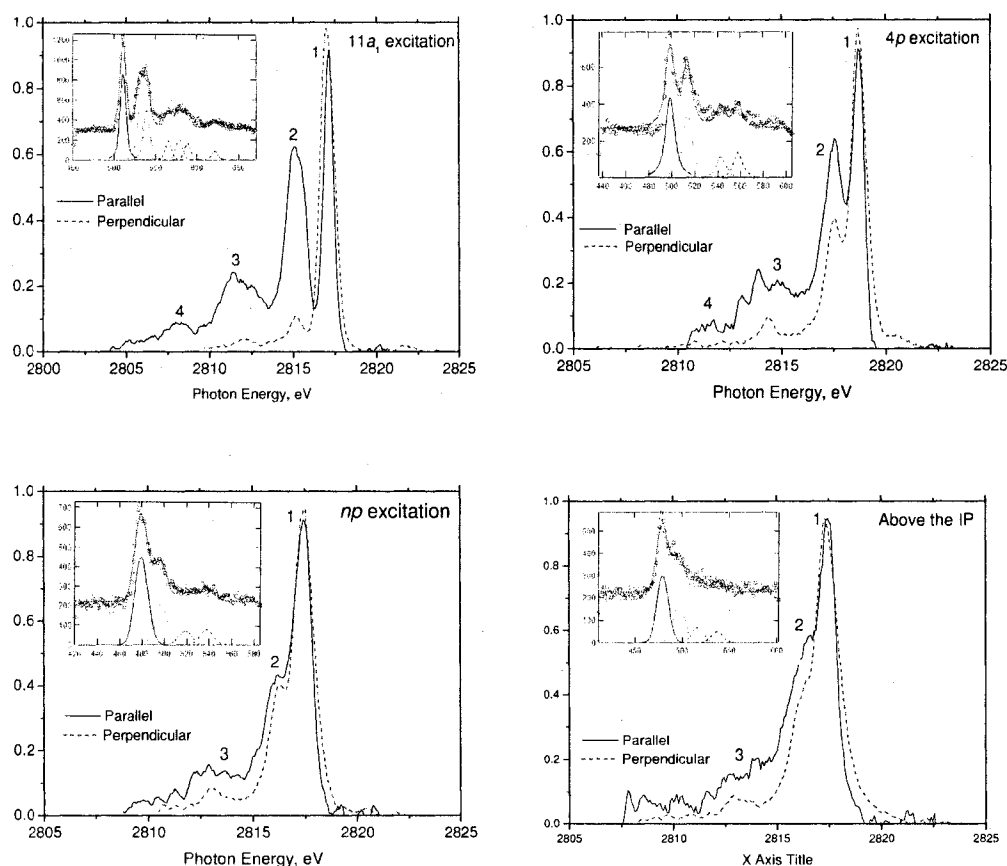


Figure 59. Measured Cl  $K$ -V x-ray emission spectra of  $\text{CF}_3\text{Cl}$  on the main resonance ( $1s \rightarrow 11a_1$ ), on the  $4p$  Rydberg ( $1s \rightarrow 4p$ ), on the  $np$  Rydberg ( $1s \rightarrow np$ ), and far above the IP with the peak fit for the parallel direction in the upper left corner.

### Peak Widths

The measured  $K$ -V x-ray peak widths over the main absorption resonance, over the  $4p$  and  $np$  Rydbergs, and far above the IP are shown in Figure 60. Similar to the peak width distribution seen over the main absorption resonance in the  $K$ -V emission of  $\text{CF}_2\text{Cl}_2$  and of the  $K$ -L emission seen in all four molecules, the peak widths of lie in the same parabolic distribution seen in  $\text{CF}_2\text{Cl}_2$  and in the  $K$ -L energy range. Over the resonance, there is no difference between parallel and perpendicular orientations.

Over the  $4p$  and  $np$  Rydbergs, the peak widths are increasing with increasing photon energy and also show a decrease in width on the top of the resonance. Just after the IP, the peak widths in both directions drop but then increase far above the IP. As in  $\text{CF}_2\text{Cl}_2$ , the difference in peak width above the IP is due to the crystal slit blocking the tail contributions in the parallel direction.

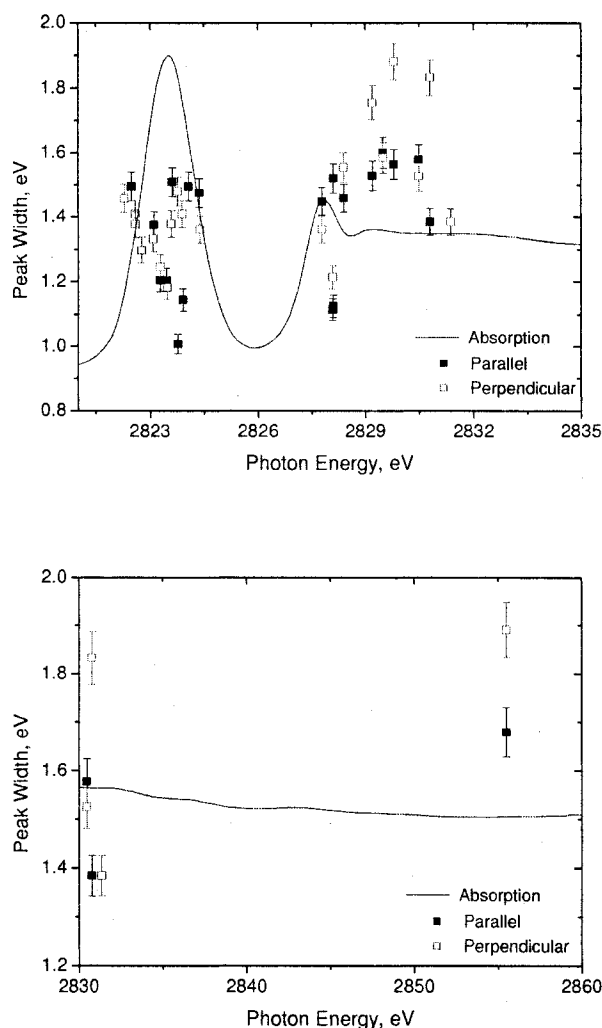


Figure 60. Measured peak widths from Cl  $K$ -V x-ray emission of  $\text{CF}_3\text{Cl}$  in the parallel (solid) and the perpendicular (empty) orientations from (top) 2820 – 2835 eV and (bottom) 2830 – 2860 eV plotted with the Cl  $K$ -edge absorption spectrum (line).



### Dispersion

Figure 61 shows the variation of the x-ray peak energy dispersion with incident photon energy over the main absorption resonance, over the  $4p$  and  $np$  Rydbergs, and far above the IP. The peak energies over the main resonance have the same non-linear dispersion as  $\text{CF}_2\text{Cl}_2$  in the  $K$ - $V$  energy range and also the same as all four of the molecules in the  $K$ - $L$  energy range (which is clearly seen in the perpendicular direction). Variations in the parallel direction are due to an increase in noise at this energy range. On top of the resonance, peak 1 has energy of 2815.5 eV, a value that is 1.6 eV less than that far above the IP and is due to screening. This is different than the screening energy of  $\text{CF}_2\text{Cl}_2$  and  $\text{CCl}_4$  because the valence MO distribution is different in  $\text{CF}_3\text{Cl}$  and the promoted electron redistributes the electron cloud differently [33].

Over the  $4p$  Rydberg, the peak energies are effectively constant in the parallel orientation while, in the perpendicular direction, the peak energies are increase. On the  $4p$  Rydberg, the peak energy is 0.4 eV lower than that far above the IP; yielding a screening energy of 0.4 eV. Close to the IP and far above the IP, the peak energies remain constant at 2817.1 eV in both polarization directions and are the same as measured by Lindle et al [30].

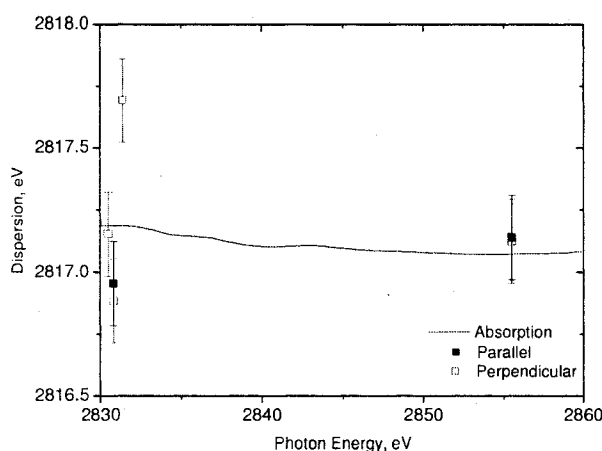
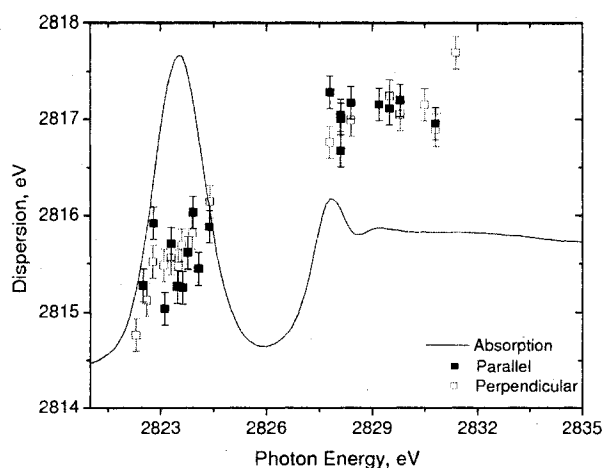


Figure 61. Measured Cl *K*-V x-ray peak dispersion for CF<sub>3</sub>Cl from (top) 2820 – 2835 eV and (bottom) 2830 – 2860 eV plotted with the *K*-edge absorption spectrum (line).

### Peak Ratios

The measured peak ratios in the parallel and the perpendicular orientations are shown in Figure 62 over the main absorption resonance and the Rydberg states. Over the main absorption resonance and the Rydberg states in the parallel direction,  $R_{21}$  remains close to 1,  $R_{31}$  is close to 0.6 and  $R_{41}$  remains close to zero. In the perpendicular orientation, there are only three peaks over the entire resonance so two peak ratios are reported here. Over

the main absorption resonance,  $R_{21}$  and  $R_{31}$  both decrease with increasing photon energy at the same rate with  $R_{21}$  having values between 0.8 and 0.12 and  $R_{31}$  having ratios between 0.02 and 0.05. Over the Rydberg states,  $R_{21}$  decreases slowly with photon energy but remains close to 0.3 over both Rydbergs and the IP.  $R_{31}$  is also decreasing with increasing photon energy but less drastically than  $R_{21}$ , remaining close to 0.05 close to the IP.  $\text{CF}_3\text{Cl}$  shows the largest polarization effects over the main resonance (as compared to  $\text{CF}_2\text{Cl}_2$  and  $\text{CCl}_4$ ); peaks 2 and 3 have very little intensity in the perpendicular direction. The MO that contributes to peak 1 ( $7e$ ) is oriented perpendicular to the molecular symmetry axis while peaks 2 and 3 have contributions from MO's with varying amounts of  $e$  and  $a_1$  symmetry. By looking at the ratios in the perpendicular direction, peak 2 has more  $e$  character than peak 3 ( $R_{31}$  is almost zero in the perpendicular direction indicating its MO contribution is largely oriented in the parallel direction). The peak ratios have large variance in the parallel direction because all ratios include peak 1 whose MO contribution is oriented perpendicular to the symmetry axis.

The effects over the  $4p$  Rydberg are similar to those seen over the main resonance when comparing trends in the parallel and perpendicular directions; there is more variation in the parallel direction than in the perpendicular. This suggests that excitations to the  $4p$  and the  $np$  Rydbergs are exciting  $p$ -states that are along the bonding axis; especially over the  $4p$  Rydberg where there are still large polarization effects; see Figure 59. Also, at this energy range, peak 3 shows the largest polarization effects; further confirming that peak 3 has the largest contributions from the  $9a_1$  MO and that peak 2 (smaller polarization effects) has significant contributions from the  $5e$  MO.

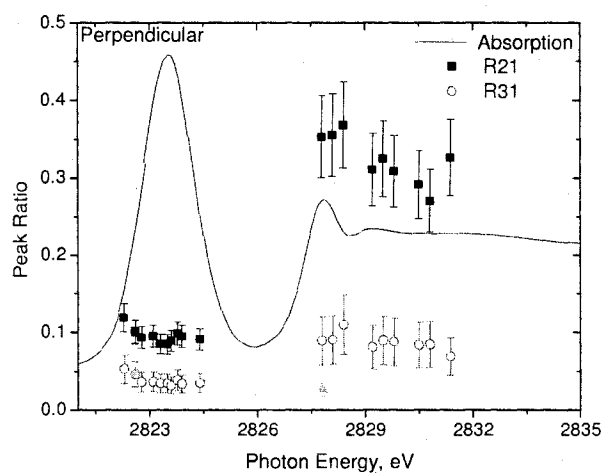
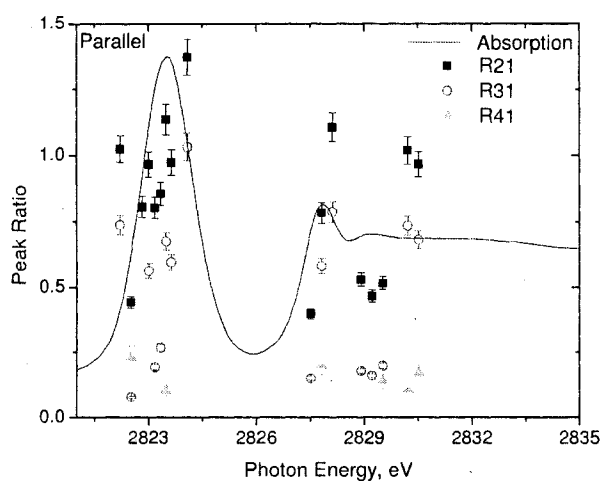


Figure 62. Measured peak ratios from the Cl  $K$ -V x-ray emission of  $\text{CF}_3\text{Cl}$  from (top) 2820 – 2835 eV in the parallel and (bottom) 2821 – 2835 eV in the perpendicular with the absorption (line).

Figure 63 shows the measured  $K$ -V peak ratios close to and far above the IP. Close to the IP in the parallel direction,  $R_{21}$  and  $R_{31}$  are larger than they are above the IP where both decrease by 0.5.  $R_{41}$  is small (0.1) below the IP; peak 4 is not analyzed above the IP so  $R_{41}$  is not reported. In the perpendicular direction,  $R_{21}$  and  $R_{31}$  remain constant above

and below the IP with  $R_{21}$  being larger than  $R_{31}$ . The parallel and perpendicular directions will be compared in the polarization section.

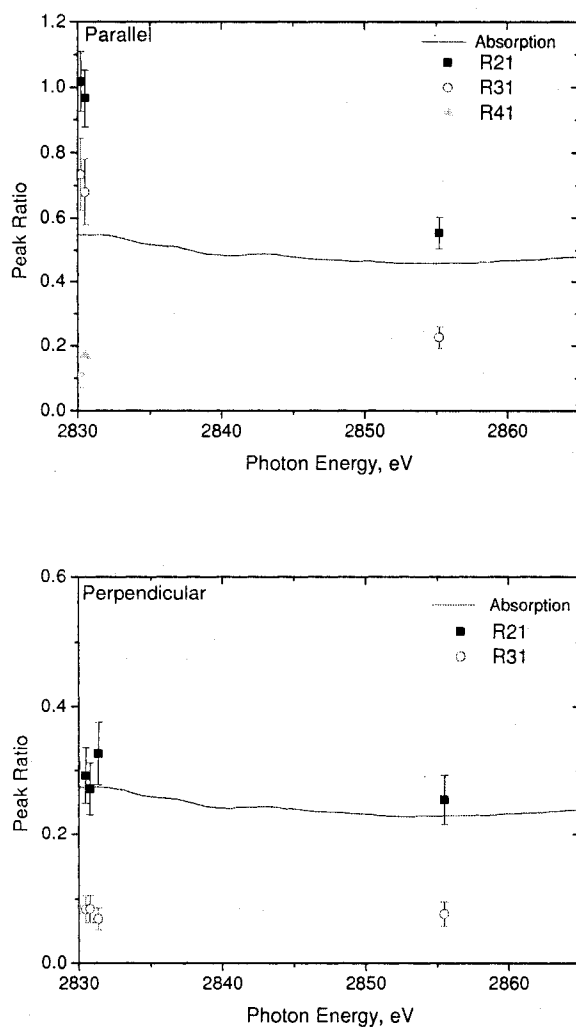


Figure 63. Measured peak ratios from the Cl *K*-V x-ray emission of CF<sub>3</sub>Cl from (top) 2830 – 2865 eV in the parallel and (bottom) 2830 – 2865 eV in the perpendicular with the absorption spectrum (line).

### Polarization

The Cl  $K$ -V relative polarization plots of peaks 1, 2, and 3 are given in Figure 64 to compare polarization trends among the three peaks. Over the main absorption resonance, the polarization of peak 1 remains negative while peaks 2 and 3 remain largely positive over the resonance; which can be deduced from Figure 59, and is the same trend that is seen in  $\text{CF}_2\text{Cl}_2$ . All three peaks show significant polarization; peak 1, being negative, is polarized in the perpendicular direction (MO's with  $e$  symmetry) while peaks 2 and 3 have positive polarization values and are predominately oriented in the parallel (MO's with  $a_1$  symmetry).

Over the Rydberg resonances, the relative polarization of peak 1 remains negative and is clustered between  $-0.2$  and  $-0.8$ . Far above the IP, the relative polarization of peak 1 also remains negative ( $-0.8$ ). The polarization values of peak 2 on the  $4p$  and the  $np$  Rydbergs are negative and increase to positive values close to the IP. Far above the IP the polarization of peak 2 is similar to that of peak 1 ( $-0.6$ ). Finally, peak 3 essentially remains positive over the Rydberg states and close to the IP. Far above the IP, the polarization of peak 3 is close to that of peaks 1 and 2 ( $-0.5$ ). Over this range, the polarization of peak 2 becomes negative, further supporting that it has significant  $e$  character. Peak 3 is largely positive and predominantly of  $a_1$  character. Above the IP, the relative polarization values of all three peaks are the same (within error). This means there is no difference between the spectra collected in the parallel and the perpendicular directions (isotropic x-ray emission). This is different from what was seen in  $\text{CF}_2\text{Cl}_2$  and  $\text{CCl}_4$ .

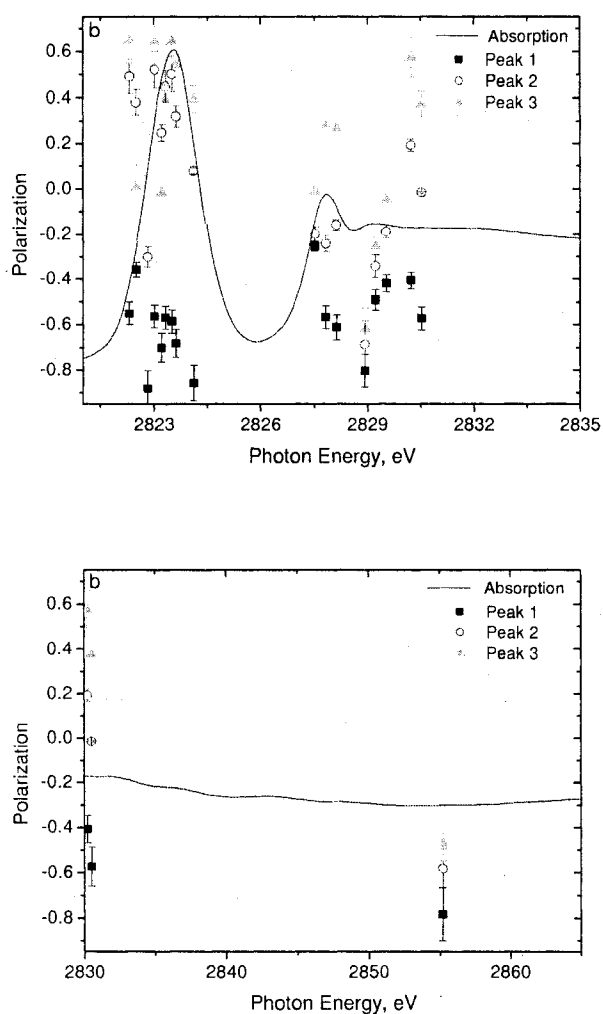


Figure 64. Relative Cl *K-V* polarization plots of CF<sub>3</sub>Cl from (top) 2820 – 2835 eV and (bottom) 2830 – 2865 eV with the absorption spectrum (line).

The polarization ratios over the main absorption resonance, the *4p* and the *np* Rydbergs and far above the IP are plotted in Figure 65. Over the main resonance, the polarization ratio of peak 1 to peak 2 and that of peak 1 to peak 3 are roughly the same; having values between  $-2$  and  $-1$ . This suggests the polarizations of all three peaks are changing in the same manner over this energy range. Over the *4p* Rydberg, the polarization ratio of peak 1 to peak 2 is increasing slightly (remaining positive) while the

ratio of peak 1 to peak 3 decreases from large and positive to small and negative. These results agree well with the trends observed in  $\text{CF}_2\text{Cl}_2$  and  $\text{CCl}_4$  where MO's with significant  $a_1$  character (symmetric about the symmetry axis) are more intense in the parallel direction and those with  $e$  character (perpendicular to the axis) are more intense in the perpendicular; results which have been well studied [4, 30].

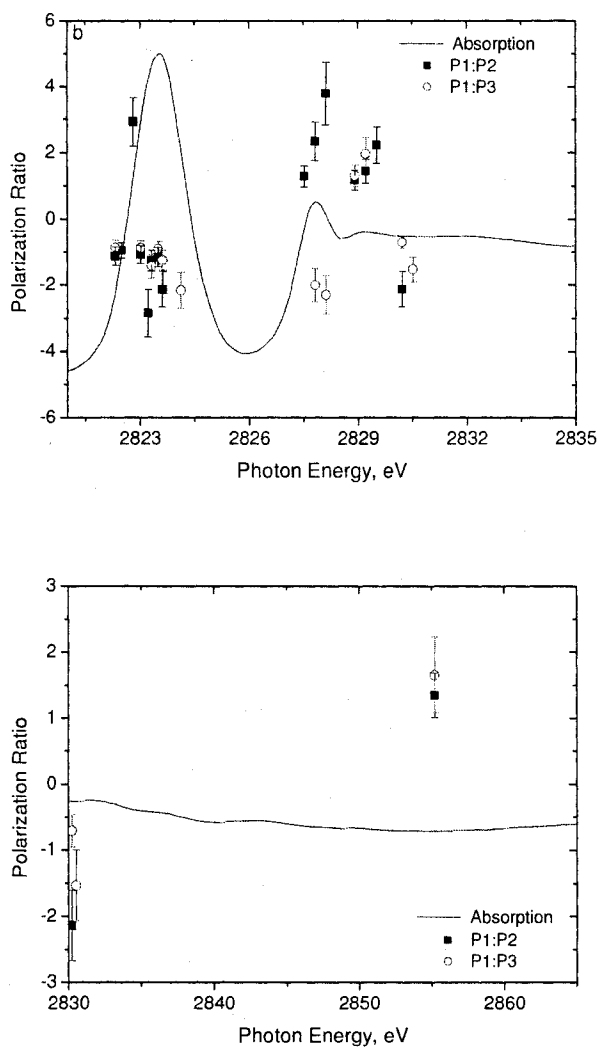


Figure 65. Cl K-V polarization ratios of  $\text{CF}_3\text{Cl}$  from (top) 2820 – 2835 eV and (bottom) 2830 – 2865 eV with the absorption spectrum (line).



Over the  $np$  Rydberg, the polarization ratios of peak 1 to peak 2 and that of peak 1 to peak 3 increase slightly (from 1.1 to 2.2) with increasing photon energy. Far above the IP, the polarization ratios of peak 1 to peak 2 and peak 1 to peak 3 are the same (1.3 and 1.6, respectively). This is different from what was seen in  $\text{CF}_2\text{Cl}_2$  and  $\text{CCl}_4$  where the polarization ratios were vastly different, both numerically ( $\text{CF}_2\text{Cl}_2$ ) and with a different sign ( $\text{CCl}_4$ ). The trend in polarization seen in  $\text{CF}_3\text{Cl}$  agrees well with what was observed in  $\text{CH}_3\text{Cl}$  (strong polarization effects on the main resonance with small or no polarization effects seen far above the IP) [4] and also what was measured in  $\text{CF}_3\text{Cl}$  [30]. This molecule can be considered as a pseudo diatomic molecule (C–Cl) and can be thought of in a simple classical picture. In such a molecule, there is only one Cl atom so there is no coupling among near degenerate states to “turn on” transitions forbidden by the dipole approximation. The emission in this molecule should therefore be isotropic above the IP; and this is in fact the case as Figures 59 and 65 illustrate.

#### Polarization Ratios of $\text{CF}_2\text{Cl}_2$ , $\text{CCl}_4$ , and $\text{CF}_3\text{Cl}$

The polarization ratios of  $\text{CF}_2\text{Cl}_2$ ,  $\text{CCl}_4$ , and  $\text{CF}_3\text{Cl}$  will be discussed together to assess similarities and differences among the three molecules. To organize the section, each absorption feature will be discussed separately (namely the main resonance and the Rydbergs followed by the continuum).

In all three molecules, there are large, but similar, polarization effects seen over the top of the main absorption resonance where some of the emission peaks observed in the parallel direction essentially disappear in the perpendicular direction; an occurrence observed in many molecules [4, 30]. For all three of these molecules, the polarization

ratio is essentially changing in the same manner in all emission peaks; see Figure 66. In this figure, all the polarization ratios are roughly constant regardless of the molecule. Although observed in the *K-L* data, the effect is much more dramatic at this energy range where the Cl 3*p* electrons are located in MO's delocalized over the entire molecule. In these cases, the x-ray emission intensity in the parallel and perpendicular directions depends on the orientation of the orbital with respect to the symmetry axis.

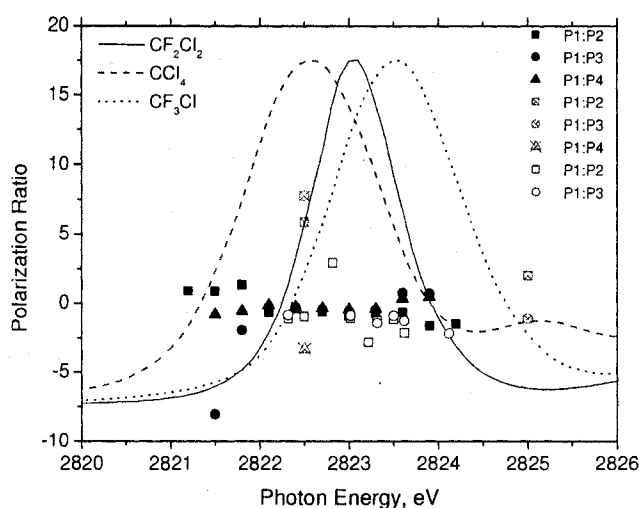


Figure 66. Comparison of the polarization ratios of CF<sub>2</sub>Cl<sub>2</sub> (line/solid), CCl<sub>4</sub> (dash/x-ed), and CF<sub>3</sub>Cl (dot/empty) over the first absorption resonance at the *K-V* energy range.

The polarization ratios of CF<sub>2</sub>Cl<sub>2</sub>, CCl<sub>4</sub>, and CF<sub>3</sub>Cl are quite different far above the IP. At these energies, there is no alignment of the molecules with respect to the polarization of the incident x-rays and the emitted fluorescence is expected to be isotropic. This is true for CF<sub>3</sub>Cl where there is no difference between the parallel and the perpendicular spectra above the IP; see Figure 59. This is also seen in the polarization

ratios where the ratio of peak 1 to peak 2 is the same as the ratio of peak 1 to peak 3 and close to 1; Figure 67.

Isotropy above the IP is not seen in all the molecules. In  $\text{CF}_2\text{Cl}_2$  and in  $\text{CCl}_4$ , there are large polarization differences seen above the IP; see Figures 46 and 54. This is also evident in Figure 67 where the polarization ratios of peak 1 to peak 2 and peak 1 to peak 3 are different (especially in the ratio of peak 1 to peak 2 in  $\text{CF}_2\text{Cl}_2$  and the ratio of peak 1 to peak 3 in  $\text{CCl}_4$  where the ratio is negative). This difference in polarization ratio seen in these two molecules suggests there is a large molecular effect above the IP. Because there is significant separation between chlorine atoms in these molecules, this effect must be due to nondipole effects, as was suggested by Mills et al [40] and discussed extensively in this chapter. In the  $K$ - $L$  data, there were polarization differences in  $\text{CF}_3\text{Cl}$  above the IP that were attributed to molecular field effects which is not the case in the  $K$ - $V$  energy range where there is no difference in the spectra in the parallel and the perpendicular directions.

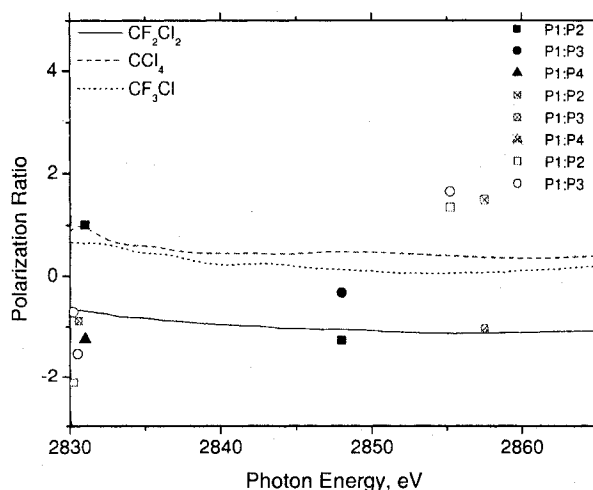


Figure 67. Comparison of the polarization ratios of  $\text{CF}_2\text{Cl}_2$  (line/solid),  $\text{CCl}_4$  (dashed/x-ed), and  $\text{CF}_3\text{Cl}$  (dotted/empty) far above the IP at the  $K$ - $V$  energy range.

## CHAPTER 7

### CONCLUSION

This chapter is divided into four sections: the first section will discuss the absorption features of all four molecules, the second will discuss the data parameters that are well understood (peak widths, dispersion, and polarization), the third will discuss the new findings (SO ratios, nondipole, and anti-Stokes dispersion), and the final section will tie all the data together.

#### Absorption Spectra

The Cl *K*-edge absorption spectra of CCl<sub>4</sub>, CFCl<sub>3</sub>, CF<sub>2</sub>Cl<sub>2</sub>, and CF<sub>3</sub>Cl have similar features; a main absorption resonance to an antibonding orbital oriented along the C-Cl bond, a second low-intensity molecular resonance of mixed symmetry and *4p* and *np* Rydberg resonances (except for CFCl<sub>3</sub> where there are no *np* Rydberg features). The absorption features are affected by the number of fluorine atoms present (as seen in the increase of the LUMO peak with the addition of F atoms) and the symmetry (the higher the symmetry the larger the IP). As expected, the atomic-like Rydberg resonances are at relatively the same energy in all four molecules. All four of these spectra have been measured in the past [30, 63] and those presented here agree well with previous measurements.

## Peak Widths, Dispersion, and Polarization

Over the first absorption resonance, the peak widths and the peak dispersion have the same distribution for all molecules, in both polarization directions, and in both the *K-L* and the *K-V* energy ranges. Also, it was found that as the detuning is increased from the top of the resonance, the peaks broaden at the same rate in both polarization directions. The hump-shaped peak width distribution and the non-linear peak dispersion can be described using well known theoretical models, which are dependent on the detuning and the final state lifetime broadening [8, 15, 23, and 24]. There is, however, significant screening of the  $3p \rightarrow 1s$  electrons in the *K-V* energy range due to the spectator electron. This was observed in all three molecules and is rather significant (1-2 eV) and was seen previously [30]. Over the  $4p$  Rydberg, the peak widths have the same distribution observed over the main absorption resonance (especially evident in the *K-L* data), this can be explained with equations 20-23, and is caused by the FC distribution; the same as over the main resonance. This is not as evident in the *K-V* data, however, as the weak signal results in more experimental error. There are also screening effects observed in the *K-V* data on the  $4p$  Rydberg (although rather small ( $\sim 0.1$  eV)). The dispersion is linear over the  $4p$  Rydberg (adding energy to the system increases the energy of the peaks) and constant close to the IP [8, 14]. Far above the IP, the peak widths and the energy dispersion are constant, which agrees well with what was seen in Ar, Xe [14], and Cu [8] where the x-ray emission is considered fluorescence (absorption followed by emission). At these energies, multielectron processes and vibrational excitation, although not resolved, are common and contribute to the larger peak widths observed.

Over the main absorption resonance in the  $K$ - $V$  energy range, there are large polarization effects observed. The initial excitation is to a MO oriented along a C-Cl bonding axis and, because of its symmetry, produces an aligned system where all the molecules excited have their symmetry axes oriented in the direction of the electric field of the incident radiation. As molecular tumbling is slow compared to x-ray emission, the molecule remains frozen during the emission process making polarization measurements on the valence orbitals possible. In all three molecules, peak 1 has significant intensity in both polarization directions and contains large amounts of  $e$  or  $b_1$  character (perpendicular), depending on the point group. Peak two was found to have significant  $a_1$  and  $b_2$  character as well as significant contributions from MOs of  $e$  and  $b_1$  character (this was observed on the  $4p$  Rydberg where the  $p$  orbitals have mixed symmetries). Peaks 3 and 4 are almost entirely composed of MOs of  $a_1$  and  $b_2$  symmetry. This agrees well with the measurements by Lindle et al and the calculations by Perera et al [30, 31].

#### Spin-Orbit Ratios, Nondipole, and Anti-Raman Dispersion

Over the main absorption resonance in the  $K$ - $L$  energy range, the SO ratios vary with photon energy more drastically in the parallel direction. This suggests that the molecular field effects are greater in the parallel direction (or along the symmetry axis) than they are in the perpendicular direction (or orthogonal to the axis) and are dependent on the symmetry of the molecule. The SO distribution in the perpendicular direction is similar to that measured in argon. Over the Rydberg resonances, the SO ratios are the same for each individual molecule; that is the parallel and perpendicular orientations have the same shape over the  $2^{\text{nd}}$  molecular resonance, the  $4p$  and the  $np$  Rydbergs and through the

IP with the parallel values being higher than the perpendicular. This is true for all molecules except  $\text{CF}_3\text{Cl}$  where the SO ratios are vastly different in the parallel direction over the  $4p$  Rydberg. In this energy region, the molecular field is still affecting the SO ratios even on an atomic-like resonance; especially in  $\text{CF}_3\text{Cl}$  where the dispersion is different from the other four molecules and from argon. Again, the large difference is in the parallel direction (along the axis) where the MF has a larger coupling. The SO ratios, while remaining constant above the IP, are different in each polarization direction and for each molecule. The largest effects are seen in the parallel direction in  $\text{CCl}_4$ . In this molecule, there are large oscillations in the SO ratio above the IP (which is not seen in the perpendicular direction or in any other molecule) where small changes in symmetry have large effects in this molecule.

In all the energy ranges of the  $K$ - $L$  data, symmetry is a large contribution to the MF effects. Over the main resonance and over the  $4p$  Rydberg, molecules with  $C_{3v}$  symmetry have the largest differences between parallel and perpendicular directions. Distortions in the ground-state geometry must affect  $C_{3v}$  molecules more than  $T_d$  or  $C_{2v}$  molecules. Surprisingly, the emission spectra still retain the shape of the spin-orbit doublet even with all the MF effects.

Polarization differences among  $\text{CF}_2\text{Cl}_2$ ,  $\text{CCl}_4$ , and  $\text{CF}_3\text{Cl}$  in the  $K$ - $V$  energy range have been attributed to nondipole effects. In  $\text{CF}_2\text{Cl}_2$  and  $\text{CCl}_4$ , the x-ray emission above the IP is anisotropic, an effect not seen before. As there is relatively no alignment of the molecular system at these energies, polarization effects are not the cause of this anisotropy and must be attributed to nondipole effects. These effects are dependent on

the separation of like atoms (Cl) as the large separation renders the dipole approximation invalid and phase variations of the incident radiation over the molecule become significant [40]. These variations lead to vibronic coupling among near degenerate states (the two 1s core orbitals). This coupling can open channels otherwise not seen when the dipole approximation holds; in the pseudo diatomic molecule  $\text{CF}_3\text{Cl}$ , the dipole approximation is valid as this molecule can be treated in a simple classical picture. These nondipole effects are possible at energies below the IP but are not as evident as there are such large polarization effects. The nondipole effects were also found to be dependent on the number of like atoms (or the number of Cl atoms in this case). The differences in polarization ratios were far greater in  $\text{CCl}_4$  than they were in  $\text{CF}_2\text{Cl}_2$  above the IP where the number of Cl atoms has doubled; see Figure 68.

The peak energy dispersion over the 2<sup>nd</sup> molecular resonance in the  $K$ - $L$  energy range was found to *decrease* with increasing photon energy. In this case, the emitted photon's energy is dependent on vibrational excitations; where excitation of several intermediate states (contributions from the main resonance and the second molecular resonance) leads to negative energy dispersion on the high-energy side of the 2<sup>nd</sup> molecular resonance. In this case, the vibrational energy of the final state is greater than that of the initial state ( $\omega_f > \omega_i$ ) and the negative dispersion can be explained by equation 26. This negative dispersion has been calculated in CO but this is the first experimental measurement of a negative dispersion.



## Conclusion

In the *K-L* and the *K-V* energy ranges, the peak widths and the energy dispersion can be described using intrinsic properties of the Cl atom (lifetime broadening) and the energy of the incoming photon (detuning); which is the same phenomenon observed in HCl [15] (at both energy ranges) and is described by theory [23, 24]. The result of this yields no differences between parallel and perpendicular directions and among different molecules even though the molecules are of different symmetry with differing numbers of F and Cl atoms. In contrast, the SO ratio (polarization) can be described by extrinsic properties (molecular field effects or nondipole effects) and is dependent on symmetry, the differing numbers of F and Cl atoms, and on which absorption resonance is excited. The true nature and the magnitude of these new effects are unknown at this time and theoretical models are required to fully investigate these phenomena.

## APPENDIX I

### RAISING AND LOWERING OPERATORS OF J

The square of the total angular momentum is [21]:

$$J^2 = J_x^2 + J_y^2 + J_z^2 \text{ where } [J^2, J_z] = 0 \text{ (the same is true of } J_y \text{ and } J_x).$$

What then are the eigenstates of  $J^2$  and  $J_z$  such that

$$J^2 f = \lambda f \text{ and } J_z f = \mu f ?$$

To determine the eigenstates, a ladder operator technique will be used. Let

$$J_{\pm} \equiv J_x \pm iJ_y, [J_z, J_{\pm}] = \pm \hbar J_{\pm}, \text{ and } [J^2, J_{\pm}] = 0.$$

Since  $f$  is an eigenfunction of  $J^2$  and  $J_z$ , then so is  $J_{\pm} f$  [64]. Because of this,

$$J^2 (J_{\pm} f) = J_{\pm} (J^2 f) = J_{\pm} (\lambda f) = \lambda (J_{\pm} f),$$

where  $J_{\pm} f$  is an eigenfunction of  $J^2$  with the same eigenvalue  $\lambda$ . Now

$$J_z (J_{\pm} f) = (J_z J_{\pm} - J_{\pm} J_z) f + J_{\pm} J_z f = \pm \hbar J_{\pm} f + J_{\pm} (\mu f) = (\mu \pm \hbar) (J_{\pm} f).$$

From this,  $J_{\pm} f$  is an eigenfunction of  $J_z$  with a new eigenvalue  $\mu \pm \hbar$ . In this scheme,  $J_+$  is the raising operator as it increases the eigenvalue of  $J_z$  by  $\hbar$  and  $J_-$  is the lowering operator. To obtain the maximum eigenvalue, the following condition is applied:

$$J_+ f_i = 0$$

where  $f_i$  is the function to obtain the maximum eigenvalue. Let  $\hbar j$  be the eigenvalue of  $J_z$  at the maximum:

$$J_z f_i = \hbar j f_i \text{ and } J^2 f_i = \lambda f_i.$$

It is now useful to determine the following:

$$J_{\pm}J_{\mp} = (J_x \pm iJ_y)(J_x \mp iJ_y) = J_x^2 + J_y^2 \mp i(J_xJ_y - J_yJ_x) = J^2 - J_z^2 \mp i(\hbar J_z).$$

From this, we can say

$$J^2 = J_{\pm}J_{\mp} + J_z^2 \mp \hbar J_z.$$

Now,

$$J^2 f_l = (J_{\pm}J_{\mp} + J_z^2 + \hbar J_z) f_l = (0 + \hbar^2 j^2 + \hbar^2 j) f_l = \hbar^2 j(j+1) f_l$$

and hence

$$\lambda = \hbar^2 j(j+1).$$

Applying the lowering operator to the function with the minimum eigenvalue yields the following:

$$\lambda = \hbar^2 j'(j'-1)$$

where  $j'$  is the eigenvalue of  $J_z$  at the minimum. We can conclude that

$$j' = -j.$$

The eigenvalues of  $J_z$  are  $m_j \hbar$  where  $m_j$  goes from  $-j$  to  $j$  in integer steps (as the raising and lowering operators change the eigenvalues by one unit of  $\hbar$ ). Finally,

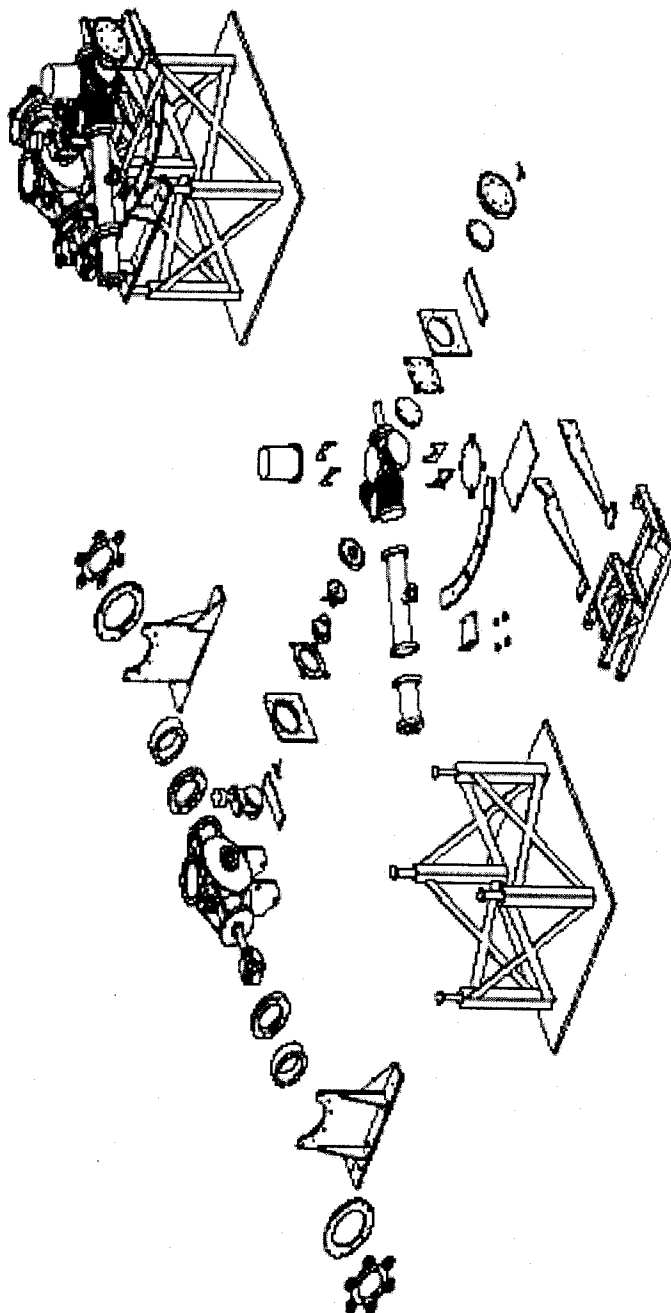
$$j = \ell + s \text{ (the definition of total angular momentum) and}$$

$$m_j = -j, -j+1, \dots, j-1, j.$$

For a given value of  $j$ , there are  $2j+1$  possible states. This raising and lowering scheme can be used to determine the eigenvalues of any angular momentum system (orbital, spin, total). Imposing boundary conditions will determine if the eigenvalues have integral values (such as orbital angular momentum) or half-integral values (as in spin).

## APPENDIX II

### AUTOCAD DRAWING OF THE X-RAY EMISSION SPECTROMETER



### APPENDIX III

#### CHARACTER TABLES FOR $C_{2v}$ , $C_{3v}$ , AND $T_d$ MOLECULES

Character Tables [21]:

$C_{2v}$	E	$C_2$	$\sigma_v$	$\sigma_v'$
$A_1$	1	1	1	1
$A_2$	1	1	-1	-1
$B_1$	1	-1	1	1
$B_2$	1	-1	-1	1

$C_{3v}$	E	$2C_3$	$3\sigma_v$
$A_1$	1	1	1
$A_2$	1	1	-1
E	2	-1	0

$T_d$	E	$8C_3$	$3C_2$	$6\sigma_d$	$6S_4$
$A_1$	1	1	1	1	1
$A_2$	1	1	1	-1	-1
E	2	-1	2	0	0
$T_1$	3	0	-1	-1	1
$T_2$	3	0	-1	1	-1

## REFERENCES

- [1] Y. Baer and G. Busch, Phys. Rev. Lett. 30, 280 (1973).
- [2] B. Smandek, Y. Gao, T. J. Wagener, J. H. Weaver, F. Levy, and G. Margaritondo, Phys. Rev. B. 37, 4196 (1988).
- [3] H. M. Boechat Roberty, C. E. Bielschowsky, and G. G. B. de Souza, Phys. Rev. A. 44, 1964 (1991).
- [4] D. W. Lindle, P. L. Cowan, R. E. LaVilla, T. Jach, R. D. Deslattes, B. Karlin, J. A. Sheehy, T. J. Gil, and P. W. Langhoff, Phys. Rev. Lett. 60, 11 (1988).
- [5] [http://www-als.lbl.gov/als/als\\_users\\_bl/9.3.1-Datasheet.pdf](http://www-als.lbl.gov/als/als_users_bl/9.3.1-Datasheet.pdf)
- [6] J. Stohr, *NEXAFS Spectroscopy* (Springer Verlag, Berlin, 1992).
- [7] T. K. Sham, B. X. Yang, J. Kirz, and J. S. Tse, Phys. Rev. A. 40, 652 (1989).
- [8] P. Eisenberger, P. M. Platzman, and H. Winick, Phys. Rev. B. 13, 2377 (1976).
- [9] F. Bloch, Phys. Rev. 48, 187 (1935).
- [10] W. C. Stolte, D. L. Hansen, M. N. Piancastelli, I. Dominguez Lopez, A. Rizvi, O. Hemmers, h. Wang, A. S. Schlachter, M. S. Lubell, and D. W. Lindle, Phys. Rev. Lett. 86, 4504 (2001).
- [11] J. Maruani, A. I. Kuleff, Ya. I. Delchev, and C. Bonnelle, *Fundamental World of Quantum Chemistry: A Tribute to the Memory of Per-Olov Lowdin*, Edited by E. J. Brandas and E. S. Kryachko (Kluwer Academic, Dordrecht 2003) pgs 639-654.
- [12] P. H. Citrin, Phys Rev Lett. 31, 1164 (1973).
- [13] P. Eisenberger, P. M. Platzman, and H. Winick, Phys. Rev. Lett. 36, 623 (1976).
- [14] M. A. MacDonald, S. H. Southworth, J. C. Levin, A. Henins, R. D. Deslattes, T. LeBrun, Y. Azuma, P. L. Cowan, and B. A. Karlin, Phys. Rev. A. 51, 3598 (1995).
- [15] M. Simon, L. Journal, R. Guillemin, W. C. Stolte, I. Minkov, F. Gel'mukhanov, P. Salek, H. Agren, S. Carniato, R. Taieb, A. C. Hudson, and D. W. Lindle, Phys. Rev. A. 020706 (2006).

- [16] S. I. Salem, D. C. Clark, and R. T. Tsutsui, *Phys. Rev. A* 5, 2390 (1972).
- [17] M. O. Krause, T. A. Carlson, and R. D. Dismukes, *Phys. Rev.* 170, 37 (1968).
- [18] [http://en.wikipedia.org/wiki/Auger\\_electron\\_spectroscopy](http://en.wikipedia.org/wiki/Auger_electron_spectroscopy)
- [19] V. L. Shneerson, W. T. Tysoe, and D. K. Saldin, *Phys. Rev. B* 53, 10177 (1996).
- [20] A. C. Hudson. *The Design and Performance of an X-Ray Emission Spectrometer Using the Polarized  $K\alpha$  Spectra of Chlorine and Potassium*, Master's Thesis, December 2003.
- [21] P. W. Atkins and R. S. Friedman, *Molecular Quantum Mechanics* (Oxford University Press, New York, 1997).
- [22] I. A. Levine, *Quantum Chemistry* (Prentice Hall, New Jersey, 2000).
- [23] F. Gel'mukhanov and H. Agren, *Physics Reports* 312, 87 (1999).
- [24] F. Gel'mukhanov and H. Agren, *Phys. Rev. A* 54 3960 (1996).
- [25] M. A. Ratner and G. C. Schatz, *Introduction to Quantum Mechanics in Chemistry* (Prentice Hall, New Jersey, 2001).
- [26] S. Brennan, P. L. Cowan, R. D. Deslattes, A. Henins, D. W. Lindle, and B. A. Karlin, *Rev. Sci. Instrum.* 60, 2243 (1989).
- [27] J. D. Mills and P. W. Langhoff, *Raman Emission by X-Ray Scattering*, Edited by D. L. Ederer and J. H. McGuire, (World Scientific, River Edge, 1996).
- [28] K. Das Gupta, *Phys. Rev. Lett.* 3, 38 (1959).
- [29] C. J. Sparks, Jr., *Phys. Rev. Lett.* 33, 262 (1974).
- [30] D. W. Lindle, P. L. Cowan, T. Jach, R. E. LaVilla, R. D. Deslattes and R. C. C. Perera, *Phys. Rev. A* 45, 5 (1991).
- [31] R. C. C. Perera, P. L. Cowan, D. W. Lindle, R. E. LaVilla, T. Jach, and R. D. Deslattes, *Phys. Rev. A* 43, 7 (1991).
- [32] P. Skytt, P. Glans, K. Gunnelin, J.-H Guo, J. Nordgren, Y. Luo and H. Ågren, *Phys. Rev. A* 55, 1 (1997).
- [33] J. Nordgren, P. Glans, K. Gunnelin, J.-H Guo, P. Skytt, C. S  the, and N. Wassdahl, *App. Phys. A* 65, 97 (1997).



- [34] P. Glans, P. Skytt, K. Gunnelin, J.-H Guo, J. Nordgren, F. Gel'mukhanov, A. Cesar, and H. Ågren, *J. Elctr. Spectr. Rel. Phenom.* 82, 3 (1996).
- [35] P. Skytt, P. Glans, K. Gunnelin, J.-H Guo and J. Nordgren, *Phys. Rev. A* 55, 1 (1997).
- [36] H. Agren, Y. Luo, F. Gel'mukhanov, H. Jorgen, and A. Jensen, *J. Elctr. Spectr. Rel. Phenom.* 82, 125 (1996).
- [37] P. Glans, K. Gunnelin, P. Skytt, J.-H Guo, N. Wassdahl, J. Nordgren, H. Ågren, F. Gel'mukhanov, T. Warwick, and E. Rotenberg, *Phys. Rev. Lett.* 76, 14 (1996).
- [38] A. Cesar, F. Gel'mukhanov, Y. Luo, H. Ågren, P. Skytt, P. Glans, J.-H Guo, K. Gunnelin and J. Nordgren, *J. Chem. Physics* 106, 9 (1997).
- [39] P. Skytt, P. Glans, J.-H Guo, K. Gunnelin, C. Sâthe, J. Nordgren, F. Gel'mukhanov, A. Cesar and H. Ågren, *Phys. Rev. Lett.* 77, 25 (1996).
- [40] J. D. Mills, J. A. Sheehy, T. A. Ferrett, S. H. Southworth, R. Mayer, D. W. Lindle and P. W. Langhoff, *Phys. Rev. Lett.* 79, 3 (1997).
- [41] K. Gunnelin, P. Glans, J. E. Rubensson, C. Sathe, J. Nordgren, Y. Li, F. Gel'mukhanov, and H. Agren, *Phys. Rev. Lett.* 83, 1315 (1999).
- [42] N. Kosugi and T. Ishida, *Chem. Phys. Lett.* 329, 138 (2004).
- [43] N. Kosugi, S. Bodeur, and A. P. Hitchcock, *J. Elctr. Spectr. Rel. Phenom.* 51, 103 (1990).
- [44] S. Svensson, A. Ausmees, S. J. Osborne, G. Bray, F. Gel'mukhanov, H. Agren, A. Naves de Brito, O.-P. Salranen, A. Kivimaki, E. Nommiste, H. Askela and S. Askela, *Phys. Rev. Lett.* 72, 3021 (1994).
- [45] M. Kivilompolo, A. Kivimaki, M. Jurvansuu, H. Askela, S. Askela, and R. F. Fink, *J. Phys. At. Mol. Opt. Phys.* 33 157 (2000).
- [46] K. Ellingsen, T. Saue, H. Askela, and O. Gropen, *Phys. Rev. A.* 55, 2743 (1997).
- [47] R. Mayer, D. W. Lindle, S. H. Southworth, and P. L. Cowan, *Phys. Rev. A* 43, 1 (1991).
- [48] K. Gunnelin, P. Glans, P. Skytt, J.-H Guo, J. Nordgren and H. Ågren, *Phys. Rev. A* 57, 2 (1998).
- [49] M. Simon, C. Morin, N. Leclercq, P. Morin, K. Ueda, Y. Sato, S. Tanaka, and Y. Kayanuma, *Phys. Rev. Lett.* 79, 3857 (1997).

- [50] P. Morin and I. Nenner, Phys. Rev. Lett. 56, 1913 (1986).
- [51] C. Sathe, F. F. Guimaraes, J.-E. Rubensson, J. Nordgren, A. Agui, J. Guo, U. Ekstrom, P. Norman, F. Gel'mukhanov, and H. Agren, Phys. Rev. A. 74 062512 (2006).
- [52] P. Kuiper and B. I. Dunlap, J. Chem. Phys. 100, 4087 (1994).
- [53] R. Feifel, A. Baev, F. Gel'mukhanov, H. Agren, M. N. Piancastelli, M. Andersson, G. Ohrwall, C. Miron, M. Meyer, S. L. Sorensen, A. Naves de Brito, O. Björneholm, L. Karlsson, and S. Svensson, Phys. Rev. A. 69, 022707 (2004).
- [54] K. Ueda, J. Elcetr. Spectr. Rel. Phenom. 88, 1 (1998).
- [55] S. Sundin, F. Gel'mukhanov, H. Agren, S. J. Osborne, A. Kikas, O. Björneholm, A. Ausmees, and S. Svensson, Phys. Rev. Lett. 79, 1451 (1997).
- [56] S. H. Southworth, D. W. Lindle, R. Mayer, and P. L. Cowan, Phys. Rev. Lett. 67, 9 (1991).
- [57] A. C. Hudson, W. C. Stolte, R. Guillemin, and D. W. Lindle, Rev. Sci. Instrum. 78, 053101 (2007).
- [58] H.H. Johann, Z. Physics 69, 185, (1931).
- [59] E. Kukk, S. Aksela, and H. Aksela, Phys. Rev. A. 53, 3271 (1996).
- [60] S. Askela, K. H. Tan, G. M. Bancroft, H. Askela, B. W. Yates, and L. L. Coatsworth, Phys. Rev. A. 32, 1219 (1985).
- [61] A. Ausmees, S. J. Osborn, R. Moberg, S. Svensson, S. Aksela, O. P. Sairanen, A. Kivimaki, A. Naves de Brito, E. Nommiste, J. Jauhiainen, and H. Askela, Phys. Rev. A. 51, 855 (1995).
- [62] L. S. Cederbaum, J. Chem. Phys. 403, 562 (1995).
- [63] A. W. Potts, H. F. Fhadil, J. M. Benson, I. H. Hiller, A. A. MacDowell, and S. Jones, J. Phys. At. Mol. Opt. Phys. 27, 473 (1994).
- [64] D. J. Griffiths, *Introduction to Quantum Mechanics* (Upper Saddle River 2005).
- [65] H. A. Kramers and W. Heisenberg, Z. Phys. 31, 681 (1925).
- [66] G. R. Burton, W. F. Chan, G. Cooper, and C. E. Brion, Chem. Phys. 181, 147 (1994).

- [67] R. C. C. Perera, R. E. LaVilla, and G. V. Gibbs, J. Chem. Phys. 86, 4824 (1987).
- [68] M. Neeb, J.-E. Rubensson, M. Biermann, and W. Eberhardt, J. Elcetr. Spectr. Rel. Phenom. 67, 261 (1994).
- [69] A. Jablonski, Z Phys. 96, 236 (1935).

## VITA

Graduate College  
University of Nevada, Las Vegas

Amanda Hudson

### Home Address:

1072 Silver Bullet Ct.  
Henderson Nevada, 89011

### Degrees:

Bachelor of Science in Chemistry, 2001  
University of Nevada, Reno

Masters of Science in Chemistry, 2003  
University of Nevada, Las Vegas

### Special Honors and Awards:

Advanced Light Source Doctoral Fellow, 2005  
Nowak-Notre Dame Prize in Chemistry, 2006

### Publications:

O. Hemmers, R. Guillemin, E. P. Kanter, B. Krässig, D. W. Lindle, S. H. Southworth, R. Wehlitz, J. Baker, A. Hudson, M. Lotrakul, D. Rolles, W. C. Stolte, I. C. Tran, A. Wolska, S. W. Yu, M. Ya. Amusia, K. T. Cheng, L. V. Chernysheva, W. R. Johnson, and S. T. Manson. *Dramatic Nondipole Effects in Low-Energy Photoionization: Experimental and Theoretical Study of Xe 5s*. Phys. Rev. Lett. 91, 5 (2003).

A. C. Hudson. *The Design and Performance of an X-Ray Emission Spectrometer Using the Polarized  $K\alpha$  Spectra of Chlorine and Potassium*, Master's Thesis, December (2003).

R. Guillemin, O. Hemmers, D. Rolles, S. W. Yu, A. Wolska, I. Tran, A. Hudson, J. Baker, and D. W. Lindle. *Nearest-Neighbor-Atom Core-Hole Transfer in Isolated Molecules*. Phys. Rev. Lett. 92, 223002 (2004).

M. Simon, L. Journal, R. Guillemin, W. C. Stolte, I. Minkov, F. Gel'mukhanov, P. Salek, H. Ågren, S. Carniato, R. Taïeb, A. C. Hudson, and D. W. Lindle, *Femtosecond Nuclear Motion of HCl Probed by Resonant X-Ray Raman Scattering in the Cl 1s region*. Phys. Rev. A. 73, 020706 (2006).

A. C. Hudson, W. C. Stolte, R. Guillemin, and D. W. Lindle. *Design and Performance of a Curved-Crystal X-Ray Emission Spectrometer*. Rev. Sci. Instrum. 78, 053101 (2007).

Dissertation Title: Polarized X-Ray Emission Spectroscopy at the Cl K Edge of the Chlorofluoromethanes

Dissertation Examination Committee:

Chairperson, Dr. Dennis W. Lindle, Ph. D.

Committee Member, Dr. Boyd W. Earl, Ph. D.

Committee Member, Dr. Clemens Heske, Ph. D.

Graduate College Representative, Dr. David P. Shelton, Ph. D.